UNIVERSITY OF OKLAHOMA

GRADUATE COLLEGE

EXPERIMENTAL DETERMINATION OF OILFIELD CEMENT PROPERTIES AND THEIR INFLUENCE ON WELL INTEGRITY

A THESIS

SUBMITTED TO THE GRADUATE FACULTY

in partial fulfillment of the requirements for the

Degree of

MASTER OF SCIENCE

By

ADONIS-COSTIN ICHIM
Norman, Oklahoma
2017

EXPERIMENTAL DETERMINATION OF OILFIELD CEMENT PROPERTIES AND THEIR INFLUENCE ON WELL INTEGRITY

A THESIS APPROVED FOR THE
MEWBOURNE SCHOOL OF PETROLEUM AND GEOLOGICAL ENGINEERING

BY

_____
Dr. Cătălin Teodoriu, Chair

_____
Dr. Carl Sondergeld

_____
Dr. Ramadan Ahmed

Acknowledgements

I would first like to thank my research advisor Dr. Cătălin Teodoriu for his continuous mentorship during my time as a student. Although the door to his office was always open, I got most of the answers to my questions in our laboratory sessions, where his input made me value experimental and hands-on work. To Dr. Carl Sondergeld, for his help and patience in my NMR journey and igniting my interest in petrophysical measurements and something other than "just drilling a hole". To Dr. Ramadan Ahmed, as the third reader of this thesis.

I would also like to thank Mr. Gary Stowe for his support with the equipment and allowing me to work and learn from him this past year, and Dr. Ali Ousseini Tinni, for his valuable input and helping me understand what might be important in my measurements through asking me the right questions.

I thank Mountain Cement Company of Laramie, Wyoming, for providing the materials necessary for this research and supporting our Well Integrity Laboratory, and The Mewbourne School of Petroleum and Geological Engineering at The University of Oklahoma for encouragement and financial support throughout the program.

Finally, I would like to thank M.Sc. Niklas Romanowski and Daniel Mbainayel for their help in performing some of the experiments.

To everyone who kindly supported me, I hope I can return the service in one way or another when the time comes.

Boomer Sooner!

Adonis-Costin Ichim, Class of 2017.

Table of Contents

List of Tables

List of Figures

Abstract

Oilfield cements are a key element in well construction, during the operational phase of a well, and after its abandonment. Hydrocarbon, geothermal, gas storage and carbon sequestration wells make use of oilfield cements to seal the annular space between the casing and the formation, some of the most common cements being API Class G and H. With an increase in the world's energy needs and an expected uptick in drilling and plugging and abandonment activities, evaluating and understanding cement properties is crucial, since these properties are used in various engineering designs and calculations. In many scenarios, these properties are assumed constant with time, but an increasing number of authors have shown how properties change with time, temperature, and pressure.

This work presents experiments run on Class G cement mixed with and without additives and cured at 25°C, 50°C, and 75°C, and constant pressure over a total of approximately two years. The influence of time, temperature, and additives on the performance of these cements is evaluated, and non-destructive testing methods are used to develop correlations to assess cement mechanical properties and to understand the development of porosity and its influence on cement performance. We applied NMR for the non-destructive evaluation of porosity, pore size distribution, cement water saturation, and curing of cement. We develop more accurate correlations as a function of temperature and for a variety of additives for the estimation of unconfined compressive strength through ultrasonic measurements.

1. Introduction

1.1. Research Motivation

The worldwide energy scene is currently ongoing a series of transformations driven by technological advancements, geopolitics, and environmental concerns. Although energy market projections are subject to uncertainties related to technological breakthroughs, macroeconomics, resources, and energy policies, global energy demand is expected to grow by 30% until 2035 (EIA 2017). The effect of such uncertainties on the energy industry is presented in **Figure 1**, which shows that independent of assumptions, United States' of America (USA) energy consumption is expected to flatten out or increase by 2040 with a variation of approximately 14% between the most conservative and most generous estimate. This behavior is also observed when estimating future crude oil and dry natural gas production, as seen in **Figure 2**.

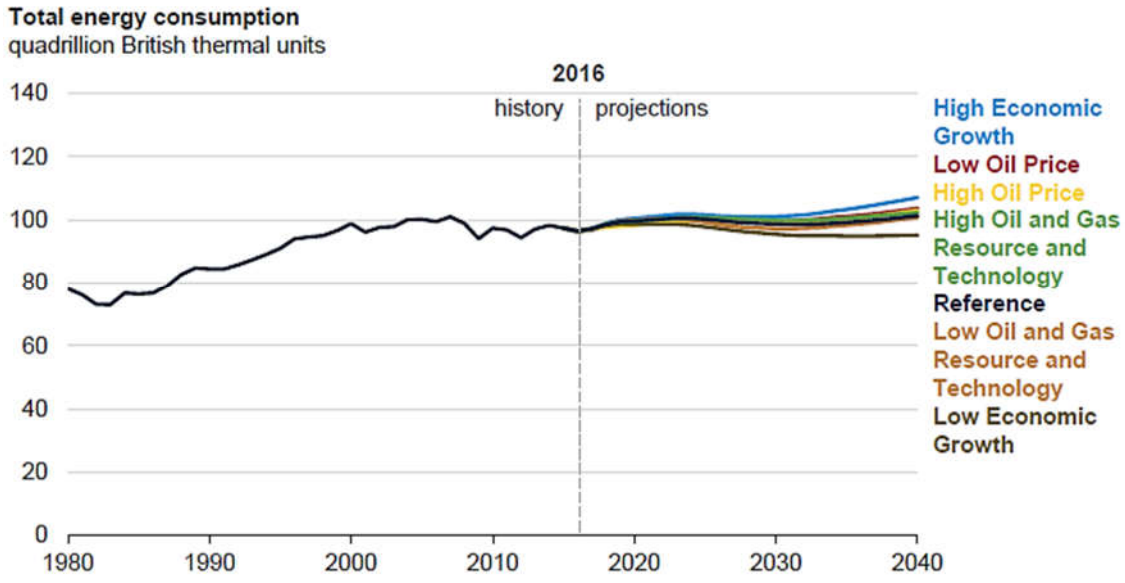

Figure 1 – Total Energy Consumption Estimations (EIA 2017)

According to BP's statistical review (2017), key uncertainties to this growth are a faster mobility revolution, alternative pathways to a lower carbon world, and slower than expected gas demand. Moreover, half of this growth will be covered by renewable forms of energy (e.g. wind, solar, geothermal, bio, hydro) and an increase in the use of natural gas. As of 2015, approximately 55% of the world primary energy sources were oil and natural gas.

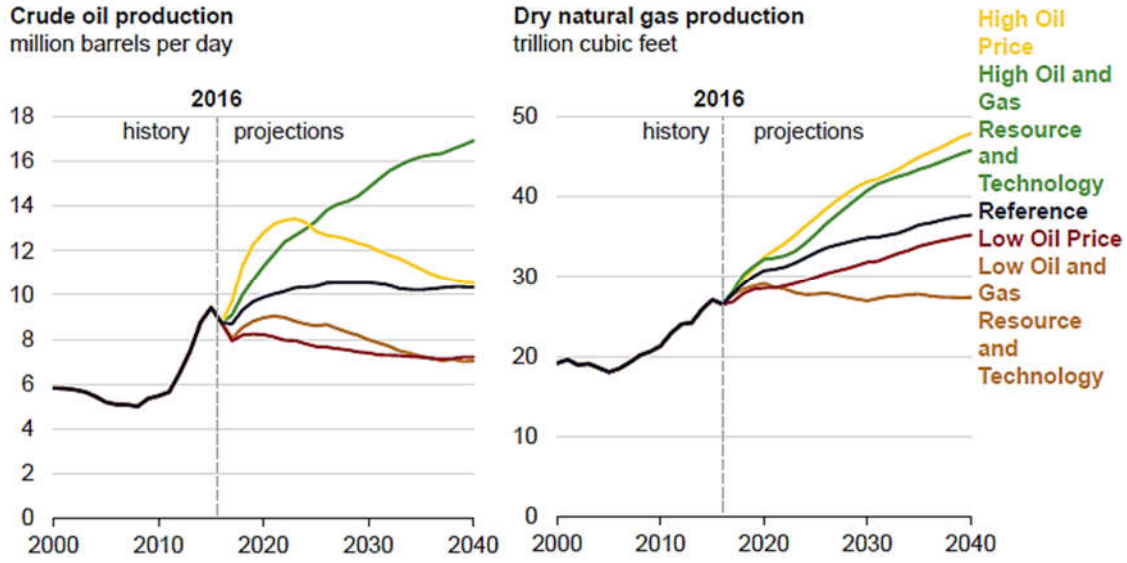

Figure 2- US Crude and Natural Gas Production Depending on Oil Prices and Tech Development (EIA 2017)

Economic growth, energy demand led by non-OECD (Organization for Economic Cooperation and Development) countries, an evolving energy mix, and technological developments, all influence the future energy metrics, according to ExxonMobil. ExxonMobil (2017) foresees oil as the world's primary energy source, and natural gas to become, together with nuclear power, the largest growing fuel source, providing 25% of the global energy demand by 2040. As shown in **Figure 3**, forecasts expect worldwide energy consumption to increase together with the share of natural gas, nuclear and

renewables in the primary energy mix, while the share of crude oil and coal is expected to decrease. Nevertheless, the use of crude oil will continue in the petrochemical industry for products such as jet fuel, asphalt and road oil, petroleum coke, lubricants, special naphthas, petrochemical feedstock, waxes, etc.

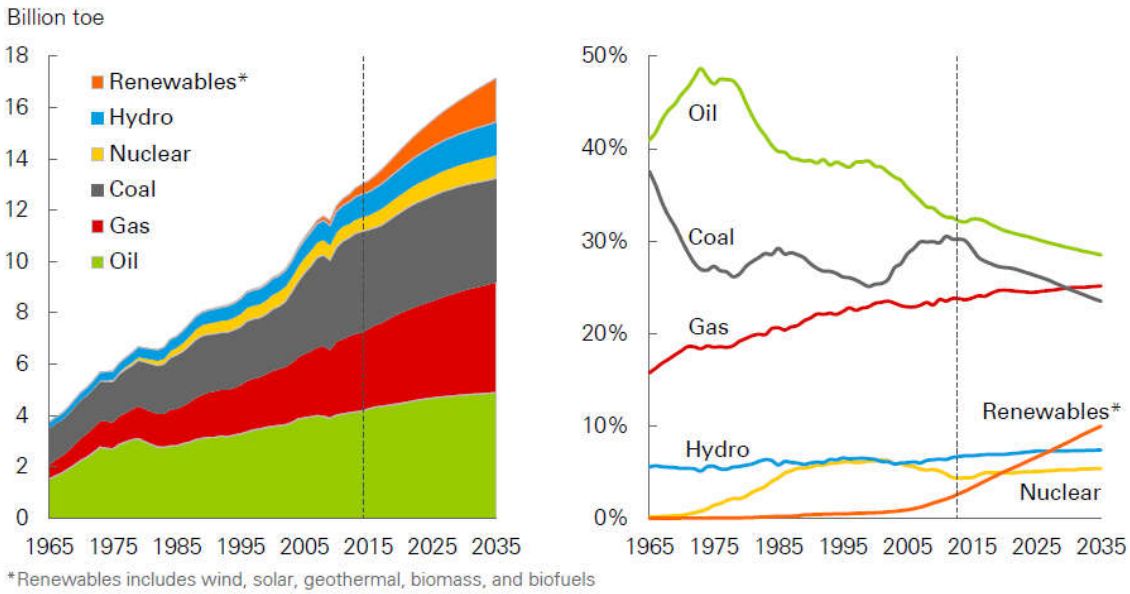

Figure 3 – Primary Energy Consumption by Fuel (left) and Shares of Primary Energy (right) (BP p.l.c. 2017)

Technical developments and data from the energy outlooks show, that independently of the scenario, drilling activity together with plugging and abandonment (P&A) operations will increase in number and complexity. These drilling activities may include oil and gas exploration and production, geothermal wells, water wells and carbon capture and storage wells. Some of the challenges encountered during the well construction process and the production phase will be outlined in the following sections.

Moreover, with the increase in drilling activity and the number of uneconomic fields onshore and offshore, the number of P&A operations rises, as shown in **Figure 4**, which presents P&A data of wells in Texas, USA, between 2008 and 2016, totaling to 59,184

or 20.7% of drilled and completed wells. For the state of Oklahoma, there were approximately 350,000 plugged and abandoned wells (70%) out of 500,000 drilled by the year 2012 (Griffith 2013). In the offshore environment, the decommissioning of the UK Continental Shelf until 2025 is estimated to cost USD 23.2 billion (GBP 17.6), with over 1,800 wells expected to be plugged and abandoned and approximately 7,500 km of pipeline to be decommissioned (Oil & Gas UK 2016).

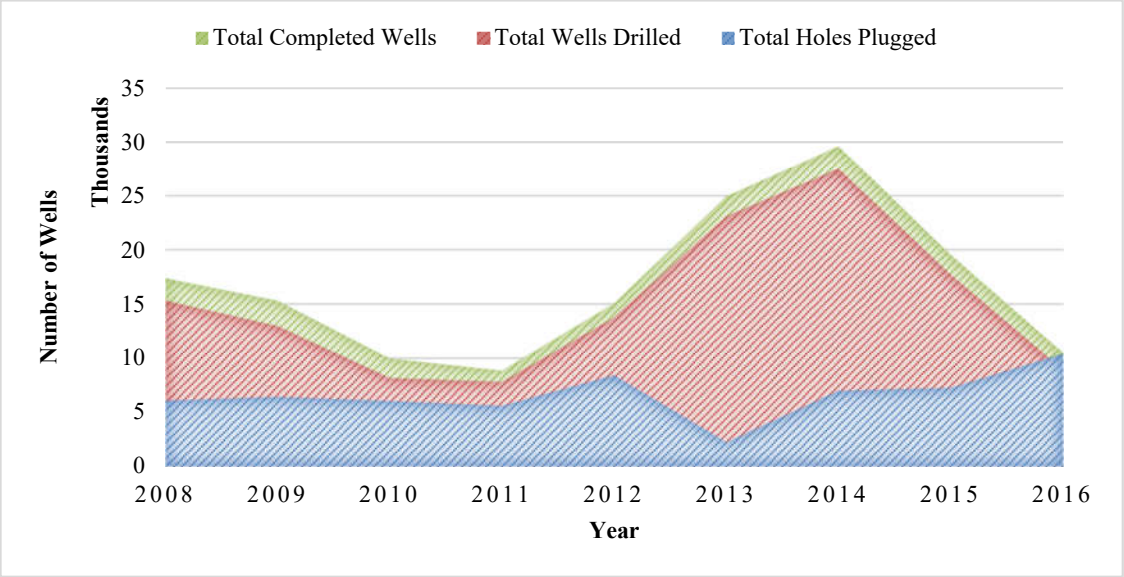

Figure 4 – Completed, Drilled and Plugged Wells for 2008 - 2016 (data acquired from the Texas Railroad Commission, 2017)

It is therefore clear that to safely and economically drill, complete, produce, and abandon wells, a better understanding of well components is necessary. Oilfield cements are a critical element in wellbore construction and well integrity, as well as abandonment. Whether discussing hydrocarbons, which have to be produced in a safe and sustainable manner, plugging and abandonment, which must provide a seal for an undetermined period of time, geothermal wells, which need low well construction costs and integrity at high temperatures over long times, gas storage wells, which must withstand high cyclic

loads, or finally, carbon storage and sequestration wells, which have to seal carbon dioxide in underground deposits, cements are the key component differentiating a successful project from failure.

Often, an insufficient understanding of the evolution of cement properties with time, and limited data are available for well integrity calculations and simulations. This research effort attempts to provide a better estimation of the mechanical property development with time, temperature, and chemical composition – which will lead to an improved assessment of well integrity. First, the process of well construction and the involved equipment is presented, after which a more detailed description of oilfield cement characteristics and testing methods is provided, with a focus on the experimental methods used in the present study. Chapters 4 and 5 cover a discussion of the results, their implication, recommendations for future work, and conclusions.

1.2. Well Construction and Well Integrity

Well construction can be defined as the actions taken to safely and economically reach the designated well target depth, while efficiently planning for the lifetime of the well. These actions consist of drilling, running casing and cementing. Well construction stops after the production casing string has been installed – which is also the common component between well construction and well completion. The well lifecycle can include production, stimulation, re-drills, and plugging and abandonment.

Well integrity is the application of technical, operational and organizational solutions to reduce the risk of uncontrolled release of formation fluids throughout the life cycle of a well (NORSOK 2004). As of 2016, approximately 22,000 technical documents related to the term well integrity have been published in the OnePetro online library of oil and gas

literature, with almost 60% of these being published in the last decade. This highlights the increasing interest of the engineering and scientific community in this topic (Ichim et al. 2016).

Commonly, wells are designed with a two-barrier philosophy, as presented in **Figure 5**. A well barrier is an envelope of one or several interdependent barrier elements preventing unintentional flow or cross-flow of formation fluids. A well barrier element cannot prevent crossflow by itself. Primary well barriers (marked blue) are fluids or mechanical means that can provide closure of well if needed. Secondary well barriers are usually mechanical devices and are shown to be closed in schematics (marked red). These may include casing, cement, casing connections, packers, etc. The following figure gives more definitions (NORSOK 2004).

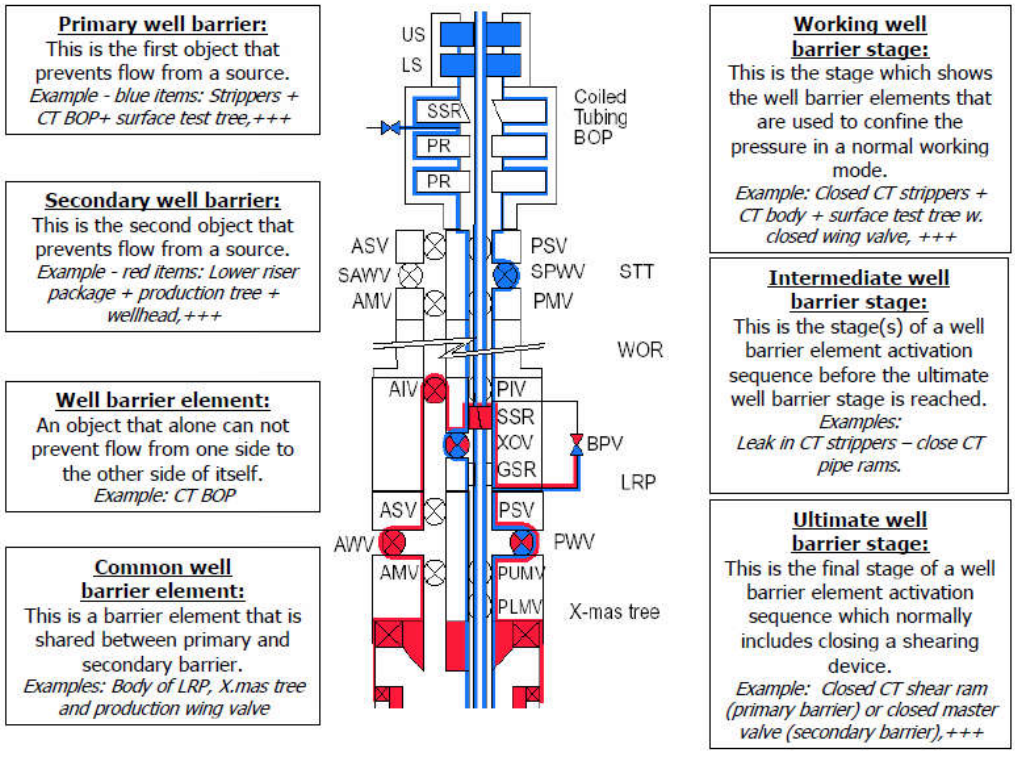

Figure 5 – Example of Well Barrier Schematic (NORSOK 2004)

Wellbore construction begins with the design of the proposed well on paper and finishes when the production casing is cemented and the well is ready for completion.

A brief description of well construction elements follows.

Casing is a seamless steel tubular engineered to withstand internal, external, and axial loads in form of burst and collapse pressures and axial tensions. The cemented casing aids in the (Bourgoyne et al. 1991):

- Prevention of freshwater contamination
- Prevention of formation cave-ins and soft formation fracturing due to high drilling fluid density in deep wells
- Zonal isolation of problem segments
- Control of downhole pressures during drilling and production

Casing also provides means of installation of secondary well integrity barriers (e.g. blowout preventers, wellhead equipment, and subsurface safety valves), production equipment (e.g. packers, tubing) and intervention and workover equipment. The basic types of casing are conductor, surface, intermediate and production casing. Liners may be installed below another casing string and do not extend to surface to reduce costs and limitations while drilling. Tieback liners may extend up to surface and provide additional pressure support if necessary.

Wellbore tubulars are standardized through the American Petroleum Institute (API) 5 standard series and the ISO 11960:2011 (Petroleum and natural gas industries) – Steel pipes for use as casing or tubing for wells. Tubulars are tested for defects, depth of defects, drift, hardness, hydrostatic pressure, impact, shear, temperature, tensile strength and correct wall thickness. Depending on the steel grade used and agreement between provider and buyer, different testing routines are employed on a various number of specimens to ensure tubulars quality and integrity. Common types of steel used for

oilfield casing are J-55, N-80, C-90, P-110 (API Steel Grades), and S-80, V-150 (non-API).

The casing string design considers maximum possible loads during different situations. The final casing design proposal must provide well integrity for the lifetime of the well, which is an unknown in a lot of the production scenarios. When designing a casing string, one must analyze wear and potential loads yielded by drilling, production, injection of water and or gas, steam, hydraulic fracturing and refracturing, workover, etc. This task is sometimes ambiguous since engineers do not plan all operations at the initial phase of the well design. Pressures, temperatures, fluids composition and chemical interaction are few of the significant parameters considered during this step. Choosing a casing connection pertains to the same parameters. A document over Marcellus Shale cementing and well casing violations reports that 90% of casing strings failure happened at connecting points between tubulars (Deane-Shinbrot et al. 2011). Connection failure can be leakage, structural failure, galling (during make-up), internal pressure yielding, jump-out or fracture under tensile load, and excessive torque induced failure (Bourgoyne et al. 1991). After running the casing in hole, it may be cemented in place. *Oilfield cements* are manufactured to comply with API Spec 10A (equivalent to ISO 10426-1:2009 – Specification for Cements and Materials for Well Cementing), and tested according to API RP 10B-2 – Recommended Practice for Testing Well Cements. Other cement-related API documents include deepwater well cements testing, preparation and testing of foam cements, recommended practices for shrinkage and expansion of well cements or determining their static gel strength, and cement sheath evaluation methods.

There are two types of cementing, depending on the application. *Primary cementing* must (Fink 2015):

- Support axial and radial casing loads
- Isolate porous formations
- Seal formation fluid influx
- Protect casing from corrosion.

Secondary cementing, represented by squeeze and plug cementing, maintains or improves well operability. When used correctly, squeeze cementing can repair a faulty primary cementation, stop drilling fluid losses, seal abandoned or depleted formations, and repair casing leaks (Fink 2015).

The three main techniques of primary cementation, also shown in **Figure 6**, are "through the casing", "inner string", and "reverse circulation" (Hole 2008). When cementing through the casing, a pair of plugs (top and bottom) together with a float collar displace the volume of cement. Centralizers and scratchers, placed on the casing outside, are instrumental for achieving casing-to-cement and cement-to-rock bonding.

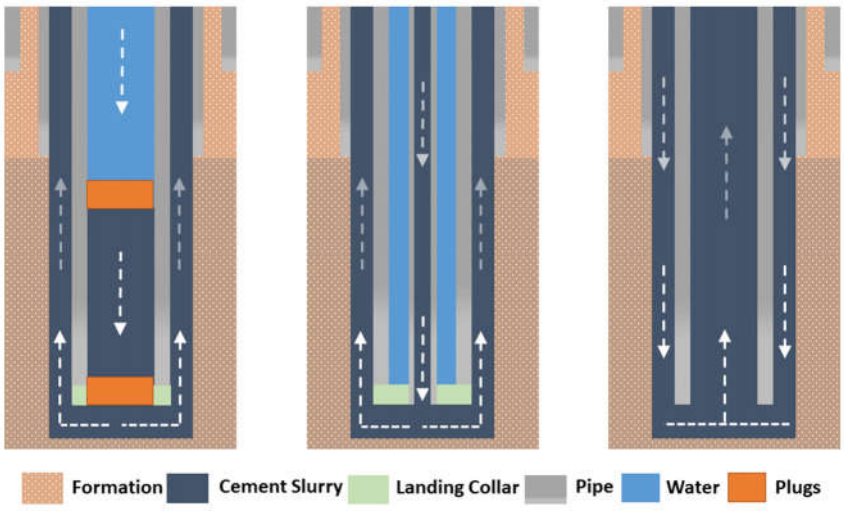

Figure 6 – Two plugs (left), inner-string (center), and reverse circulation cementing (right)

Inner string cementing uses a modified float collar that allows the landing of tubing or drill pipe at the bottom of the well and creates a seal, allowing the pumping of the cement in a shorter time with fewer losses at the joint. In reverse circulation cementing, used when weak formations are encountered at the wellbore shoe, the cement slurry is pumped down the annulus and displaces the mud back up the casing. Special tools (e.g. float collar, wellhead) are used in this case. Since the usage of wiper plugs is impossible, the detection of the end of displacement is difficult, making over-displacement by up to 300 ft. a common practice (Bourgoyne et al. 1991).

After placement and "wait-on-cement time" (WOC) cement bonds to the casing and the formation, acting as an integrity-assuring element. Its ability to withstand potential loads throughout the life of the well strongly depends on the primary cementing job quality. This, in turn, is related to casing centralization (which is standardized through API Spec 10D / ISO 10427-1:2001, and RP 10D-2/ISO 10427-2:2004), curing time, well inclination, cementing slurry quality, and influence of drilling occurring on the same pad. Moreover, the development of mechanical and thermal properties together with the chemical resistance of the cements is unknown in many of the cases, since various parties usually perform testing under conditions hardly resembling the real downhole conditions for a realistic timeframe. Heterogeneity of the wellbore cements can occur due to various factors such as lack of smoothness of the borehole surface, complex geological conditions, thick mud cakes as well as contamination of the cement.

Cement degradation may be mechanical or geochemical, and other factors can simultaneously act against the casing, cement, and ultimately overall well integrity, leading to (Ichim et al. 2016):

- Formation of micro-annulus at casing/cement interface
- Disruption of cement-formation bond
- Cement failure due to mechanical or thermal induced stress
- Corrosion of casing
- Degradation of cement (carbonation, sulfate, acid)

In their overview of identification and evaluation of well integrity, Kiran et al. (2017) classify issues by the type of well and identify various well integrity problems specific to conventional and unconventional development, geothermal and high-temperature injection water wells, high-pressure and high-temperature (HPHT) wells, enhanced recovery methods, deepwater drilling, CO_2 sequestration, and plugging and abandonment, showing that an evaluation of the wellbore as a system by periodic monitoring techniques based on experiments, logging, analytical and numerical modeling, statistical modeling, and risk analysis helps in developing a safe and sustainable engineering solution for the well lifetime..

According to Davies et al. (2014), for a well to leak, a fluid must break one or more well barriers and be driven by a force (e.g. fluid buoyancy, excess pore pressure) through one of the seven possible pathways:

- between cement and surrounding rock formations,
- between the casing and surrounding cement,
- between cement plug and casing or production tubing,
- through cement plug,
- through the cement between the casing and rock formation
- across the cement outside the casing and then between this cement and the casing
- along a sheared wellbore

Loss of well integrity can have multiple consequences from major ones (cross flow, pressurized annulus, well control situation) to catastrophic ones (blow out, infrastructure damage) (Garnier et al. 2007), leading to environmental issues, health and safety risks, social issues, non-productive time and costly repairs, which impact operational as well as capital expenditures.

In an extensive study, Davies et al. (2014) show that depending on the number of wells studied, the region, and their drilling period, up to 75% of the wells dealt with barrier or well integrity failure. For instance, 43% of the wells drilled offshore Gulf of Mexico between 1973 and 2003 and 38% of wells drilled in the North Sea between 1970 and 2011 experimented such issues, whereas the numbers for onshore wells vary between 1.9% and 22% and depend on the sample size. Some examples of well integrity breaches leading to severe consequences are:

- The Aliso Canyon gas leak, where 97,100 tons of methane and 7,300 tons of ethane escaped into the atmosphere. Initially drilled and completed in 1952, the Californian oil field was repurposed for gas storage in 1972. Due to pressure and temperature cycling, and decaying well integrity barriers, leaks started and were observed on October 23rd, 2015, leading to the necessity of drilling multiple relief wells to block gas flow to surface and the possibility of a major surface explosion. Moreover, habitants living close to the well had to leave their homes temporarily. The accident was contained after permanent well plugging on February 18, 2016 (SoCalGas 2017).
- A series of failing well integrity barriers caused the Macondo Well blowout, starting, according to BP's statement, with cement failure, followed by loss of

pressure control through the hydrostatic drilling fluid column, and failure of the blowout preventer to engage. On April 20th, 2010, eleven people working on the Deepwater Horizon drilling rig owned by Transocean died, and an estimate of 4.9 million barrels were discharged into the ocean until containment through capping (July 15th, 2010) and plugging (September 19th, 2010) (Bryant 2011).

- A case of losing primary barrier is the Ixtoc I oil spill (June 3rd, 1979), which resulted in 3 million barrels of oil leaked into the Gulf of Mexico due to loss of pressure control and the blowout preventer not being able to close on drill collars, which were being tripped out of hole. The flow of hydrocarbons from the Pemex exploratory well into the ocean was stopped on March 23rd, 1980 (Woods Hole Oceanographic Institution 2014).
- Another example of losing pressure control is the recent Davis 30 12-26 blowout of a well drilled by Chesapeake Energy in western Oklahoma, where an unexpected pressurized shallow gas zone was encountered at 900 ft. depth. No mechanical barriers were installed at that stage, since surface casing, which allows blowout preventer placement, was not run and cemented in place (Henry 2012).

It is therefore clear that for a safe operation, good communication, sound engineering practice, a good safety culture and compliant materials and well components are necessary together with an understanding of the geology.

1.3. Objectives

This research effort includes mechanical properties and NMR experiments run on Class G cement with and without additives at various temperatures and constant pressure over extended times. The main objectives of this work are:

- Evaluating the influence of time on cement mechanical properties
- Evaluating the influence of temperature on cement mechanical properties
- Determining the influence of extenders and accelerators on cement properties
- Use of non-destructive testing methods to assess mechanical properties and develop more accurate correlations between ultrasonic pulse velocities and unconfined compressive strength, considering curing temperature and additives content

The use of ultrasonic measurements and nuclear magnetic resonance measurements lead to the following additional objectives:

- Assess the development of NMR porosity and T2 spectral changes with time and temperature and test the potential of NMR measurements as a NDT method for porosity and unconfined compressive strength
- Understand the development of NMR porosity
- Assess the development of dynamic elastic properties of cement

Additional testing recommendations will be presented in the final chapter of this manuscript.

2. Wellbore Cements

This section offers information about the manufacturing and composition of cement powder, the reaction of cement powder with water, the main characteristic of cement powder, cement slurry and set cement and how these evolve with time, temperature and pressure, according to different sources. Furthermore, some cement additives and their influence are presented together with novel types of cement.

2.1. Cement Manufacturing and Classification

For cement production, calcareous and argillaceous rocks are dried, ground and mixed in different proportions in a dry or wet environment. Afterwards, this mix is heated to temperatures between 1426 °C – 1540 °C (2600 – 2800 °F) and a clinker is obtained, which is cooled down and mixed with other products (e.g. gypsum) to form the Portland cement (Nelson 1990).The name of Portland cement originates from the resemblance between concrete and Portland stone (or the concrete's ability to replace it).

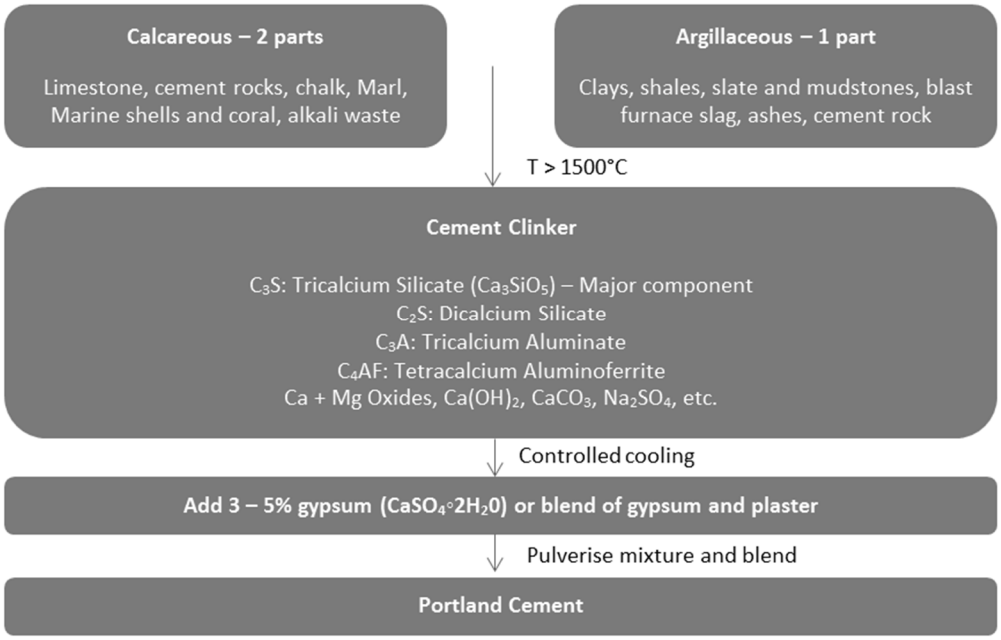

Figure 7 – Portland Cement Production Workflow (Ichim 2015)

The following table shows the typical composition of Portland cement.

Table 1 – Portland Cement Composition (Fink 2015)

Compound	Percentage
CaO – Calcium oxide (burnt lime)	60-69
SiO_2 – Silicon dioxide (silica)	18-24
Al_2O_3 + TiO_2 - Aluminum + Titanium oxide (alumina and titania)	4-8
Fe_2O_3 – Iron oxide (ferric oxide)	1-8
MgO – Magnesium oxide (magnesia)	<5
K_2O, Na_2O – Potassium and Natrium oxide	<2
SO_3 – Sulfur trioxide (sulfite)	<3

Depending on the application, Portland cements are mixed with different substances, leading to:

- Concrete: a mixture of cement powder, water, fine and coarse aggregate (sand, gravel, or a crushed rock like limestone or granite)
- Mortar: when cement powder, water, and a fine sand are mixed together, usually with an additional plasticizer (hydrated lime or an organic wetting agent)
- Cement paste: when cement powder is mixed with water – commonly referred to as grout in civil engineering and cement slurry in petroleum engineering, which also makes the focus of this work.

Oilfield cement is manufactured according to the American Petroleum Institute. There are six cement classes and three grades: ordinary (O), moderate sulfate-resistant (MSR), and high sulfate-resistant (HSR). The different cement classes are (American Petroleum Institute 2010):

- Class A: intended for use when special properties are not required, up to a depth of 6,000 ft. Available only in O grade.
- Class B: for use when conditions require moderate or high sulfate resistance (HSR), up to a depth of 6,000 ft.

- Class C: used when conditions require high early strength (which translates into higher C_3A content), up to a depth of 6,000 ft.
- Class D: recommended at depths from 6,000 to 10,000 ft. under moderately high temperature and pressures. Can be HSR or MSR.
- Classes G and H: can be used as basic well cements (as manufactured) or over a wider range of wells if used with additives. They are available in both MSR and HSR types.

2.2. An Overview of Cement Chemistry

The chemical composition of the cement powder can be divided into four mineral components, as follows:

- Tricalcium silicate: SiO_2•3CaO, simplified C_3S
- Dicalcium silicate: SiO_2•2CaO, simplified C_2S
- Tricalcium aluminate: Al_2O_3•3CaO, simplified C_3A
- Tetracalcium ferroaluminate: 4CaO•Al_2O_3•Fe_2O_3, simplified C_4AF,

Where S stands for silica, C for burnt lime (or calcium oxide), A for alumina, and F for iron oxide (Aïtcin and Flatt 2016). Calcium sulfate is added as an interground additive (American Petroleum Institute 2010).

Cements are mixed with water in different percentages as required by the manufacturer, leading to the hydration reaction, in which the clinker components react with the water, precipitating hydrates and hydroxide, which gives strength to the cement but also leads to the development of internal porosity. Depending on the water-to-cement ratio and the cement components and additives, the “wait-on-cement time” (until cement reaches a required minimum compressive strength of approximately 3.5 MPa or 500 psi) varies.

Being a hydraulic cement, Portland and oilfield cements settle and harden in both a dry and wet environment (e.g. if the slurry is left to stand in air or underwater) (Nelson 1990). The hydration of Portland cement leads to mechanical bonding, heat liberation, and change of the cement paste volume, depending on the curing conditions (Aïtcin and Flatt 2016). Since hydrating cement is not volumetrically stable, whatever the mode of curing, cement pastes can lose between 1% and 8% of their absolute volume, also known as chemical (or Le Chatelier's) contraction (Keating et al 1989; Aïtcin and Flatt 2016).

According to Powers' (1958) quantitative work on cement hydration, a cement paste must have a w/c ratio of at least 0.42 to reach full hydration, and water can be classified as reactive, forming a "solid gel" which produces the bonding properties of the cement, and non-reactive ("gel water"), glued to the hydrated cement paste. The hydration of cement pastes can be observed in two systems: closed, and open to an external source of water (Powers 1958). **Figure 8** shows the chemical contraction modeled mathematically for a sample mixed at a 0.42 w/c ratio. It is observed how in the case of hydration in a dry environment, the relative volume of air increases with time, whereas if the sample hydrates in an open wet environment, water enters the sample through the network of pores.

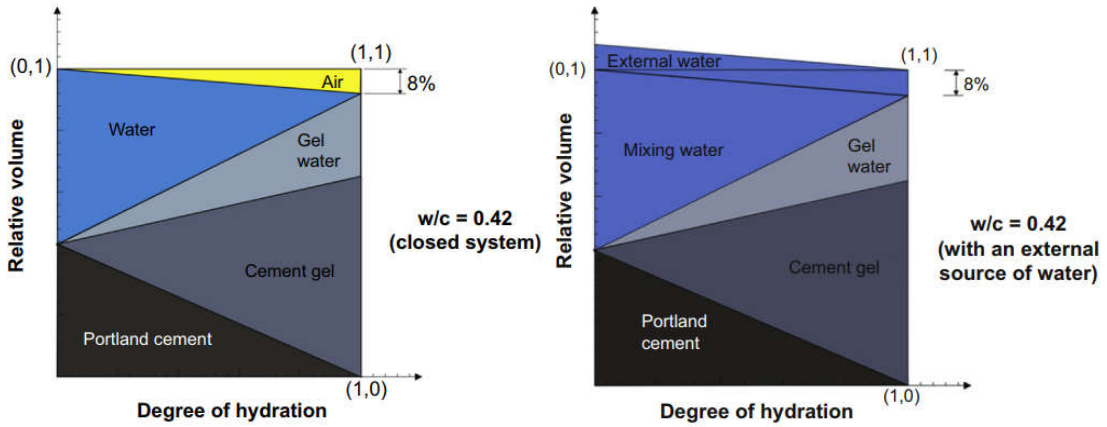

Figure 8 – Relative Volume Evolution of Cement Components During Hydration in a Dry Environment (Left) and Under Water (Right) (Aïtcin and Flatt 2016)

The hydration of Portland cement involves dissolution and precipitation in a complex chemical system, resulting in the formation of hydrates and the hardening of cement. Cement hydration is an important example of inhibited autocatalytic or chemical clock reaction, the chemical clock starting when water first contacts the anhydrous cement powder (Luke et al. 1995), reason why storage conditions for cement powder are very important. The products of hydration are (Aïtcin and Flatt 2016):

- Calcium silicate hydrate (CSH), a gel
- Calcium hydroxide (CH), a crystalline phase, also called portlandite
- Trisulfoaluminoferrite hydrates (AFt), with ettringite being the most important phase
- Monosulfoaluminoferrite hydrates (AFm)

The hydration of C_3A is important in the very early stage of hydration and influences mechanical and rheological properties of cement. Because C_3A's reaction with water is fast and leads to "flash-setting" (due to the precipitation of irregular hexagonal platelets

of calcium aluminate hydrates on the clinker surface), calcium sulfate is added to the clinker during its production process. This leads to the precipitation of ettringite.

$$C_3A+3C\underline{S}H_2+26H \rightarrow C_6A\underline{S}_3H_{32}$$

Once the sulfate ($\underline{S}$) is used up, ettringite reacts with the remaining C_3A, forming monosulfoaluminate (Aïtcin and Flatt 2016):

$$2C_3A+C_6A\underline{S}_3H_{32}+4H \rightarrow 3C_4A\underline{S}H_{12}$$

Silicate hydration (or the hydration of alite and belite) dominates hydration kinetics because it is the main component of cement powders (clinkers). The stages of this reaction are dissolution (I in **Figure 10**), induction (II), acceleration (III), deceleration (IV), and diffusion (V), with the following outcomes (Nelson 1990; Aïtcin and Flatt 2016):

$$2C_3S + 6H \rightarrow C_3S_2H_3 + 3CH$$

$$2C_2S + 4H \rightarrow C_3S_2H_3 + CH,$$

leading to the precipitation of CSH (amorphous, poorly structured crystalline phase), and CH (also called portlandite, a crystalline phase). Tricalcium silicate is responsible for strength development during hydration time, whereas dicalcium silicate is only responsible for final strength development (Fink 2015).

Gutteridge and Dalziel (1990) measured the hydration reaction over 100 days for cement clinker phases mixed individually with a water to phase ratio of 0.71. The consumption of the phases was measured using X-ray diffraction analysis. The mass composition of the cement was 68% C_3S, 14% C_2S, 6% C_3A, 7% C_4AF, and 2% calcium sulfate. The cement density was 3160 kg/m^3, with a Blaine fineness of 320 m^2/kg. They also analyzed the hydration of the cement over the same period. The data in **Figure 9** show a logarithmical behavior of the hydration reaction plots for all phases except the C_2S, with

most of the reactions happening between 0 and 40 days. Note that these developments only apply to this specific cement paste mixture.

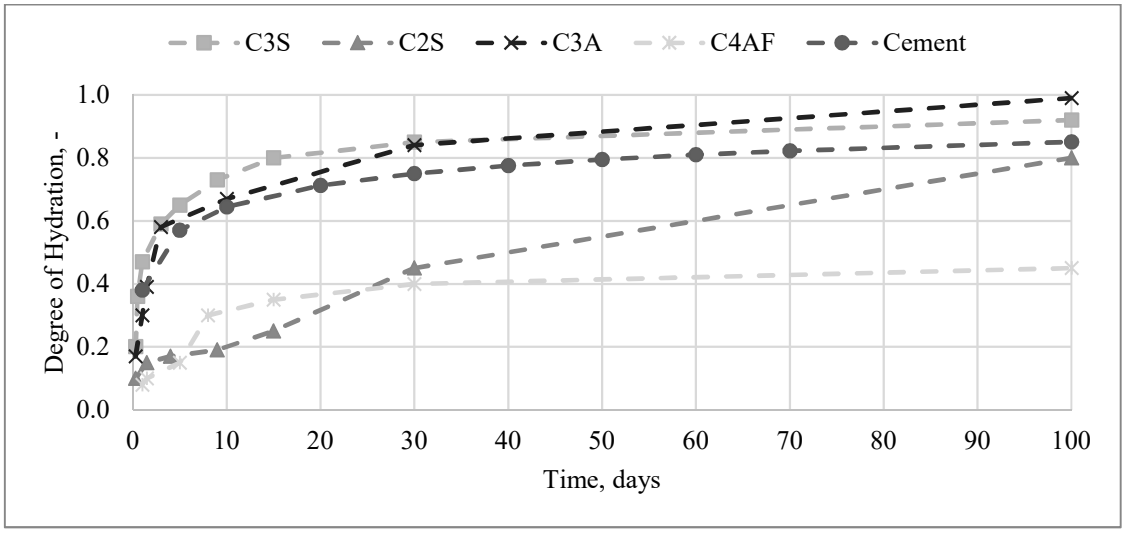

Figure 9 – Hydration of Cement and Its Phases over 100 days (Gutteridge and Dalziel 1990)

The monitoring of heat produced by cement hydration shows that although hydration takes place over extended time periods, heat flow rate and temperature increase only during the dissolution and acceleration phases of the exothermic reaction, over the first few hours after the cement is mixed with water.

Dissolution (I), induction (II), acceleration (III), deceleration (IV), and diffusion (V)

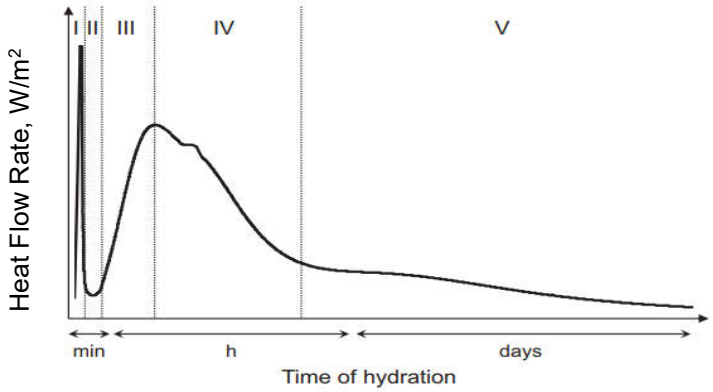

Figure 10 – Heat Flow vs. Hydration Time in Cement (Aïtcin and Flatt 2016)

Not only do products of chemical reactions precipitate, leading to the formation of hydrates and development of cement strength, but also, while water is consumed in these reactions, cement porosity changes. Since solidified cement is composed of randomly aggregated particles, it is both porous and permeable (Powers 1958). Porosity depends on various factors (cement clinker, w/c ratio, mixing method, curing conditions), and can strongly vary. The densest possible completely hydrated pure cement paste has a porosity of 26% (Powers 1958). According to Muller (2014) and his research on hydrated cement pastes, three main categories of pores can be classified by size, and are presented in the following table.

Table 2 – Cement Porosity Definitions, after (A. Muller 2014)

Type	Size	Definition/Observation
Compaction or air voids	Few µm to few mm	Created during mixing or triggered by special chemical products (air entrainment agents)
Capillary porosity	> 10 nm to a few µm	Remaining spaces not occupied by hydration products or unreacted cement grains. Some originate from chemical shrinkage.
Gel pores	<10 nm	Intrinsic porosity, generic term defining all pores within CSH. Completely saturated with interlayer water.

Depending on the measurement method, different values for cement porosity and pore sizes can be obtained. **Figure 11** shows how different authors describe the different types of pores encountered in cement pastes.

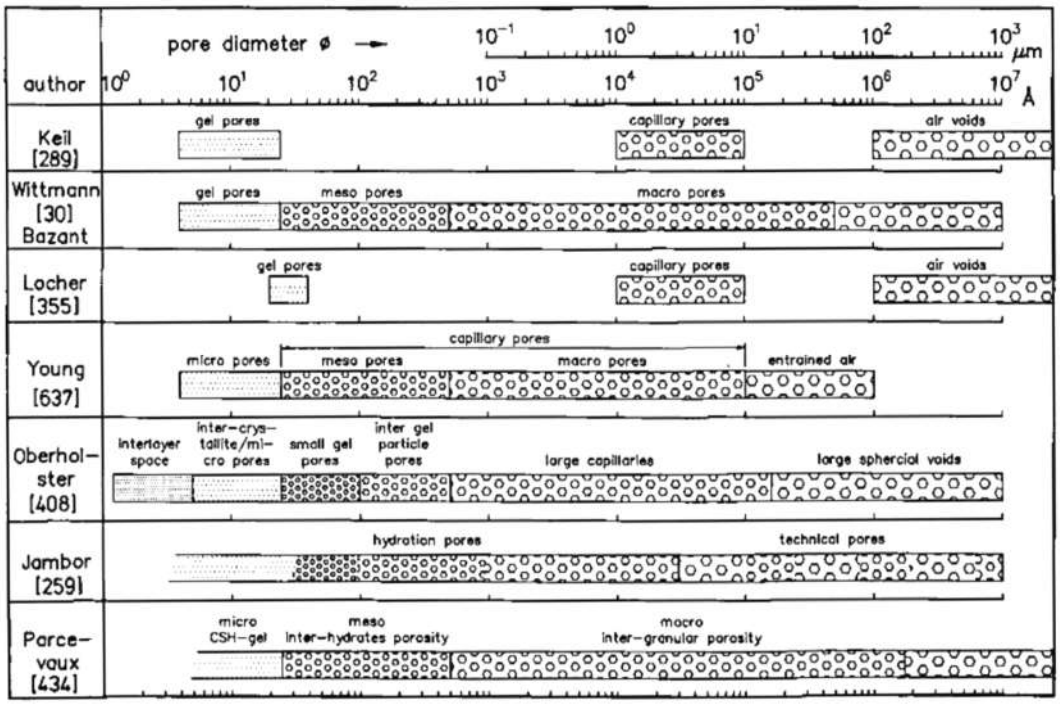

Figure 11 – Definition of Cement Porosity and Their Sizes (van Bruegel 1991)

According to Powers (1958), the permeability of a set cement mostly depends on its capillary porosity, since the resistance to flow through pores smaller than 10 nm in diameter is very high. Moreover, the curing temperature, environment, and the use of special materials can change these values.

Cementing additives control different properties and modify the behavior of the cement slurry under different conditions, which is crucial to run a proper cementing job. They can be classified in (Fink 2015; Nelson 1990):

- Accelerators: reduce the wait on cement (WOC) time – salts (depending on concentration - calcium or sodium chloride), sea water

- Retarders: increase the cement setting time; used in high-temperature mediums - sugar; lignosulphonates, hydroxycarboxylic acids, inorganic compounds and cellulose derivatives
- Extenders: lower the density and increase the yield strength of set cements; used in weak formations – water, bentonite, sodium silicates, nitrogen, ceramic microspheres, and furnace slag.
- Weighting agents: increase density – barite, hematite
- Dispersants: polymers used for a better particle distribution and the improvement of rheological properties
- Fluid-loss additives: polymers, cellulose
- Lost circulation control agents
- Strength retrogression: additives used at temperatures higher than 230°F, where cement's permeability increases and its strength decreases – Silica Flour (usually 30 – 40% by weight of cement (BWOC))
- Miscellaneous agents: anti-foam agents, fibers, latex

2.3. Considerations for Cement Design

According to Hibbeler et al. (2000), the first oilfield cementing operation was conducted in 1903 to shut off water flow of a Union Oil Corporation well in California. Modern cementing, however, started with the introduction of the two-plug method by A.A. Perkins. The first committee to study oilfield cements was established in 1937 by API, which acknowledged that the ASTM testing framework was not fit for the well applications of cements (due to increased temperatures and pressures). This resulted in the API Code 32, published in 1940, which later became API RP10B, adopted as the standard for well cement testing in 1956, while the actual Specification for Oilwell Cements was introduced in 1953. At that time, this document did not include Class G nor H Cements, which appeared in the document in 1964 and 1977, respectively.

As mentioned, cements have a variety of functions in primary and secondary cementing operations. The ability of cements to perform according to expectations depends on a multitude of factors related to the properties of the cement slurry and its components, the well design, and the geological conditions. Cements can also be used to seal the interior of a pipe from the formation below during plugging and abandonment or sidetracking operations.

Various factors must be considered when designing a cement system to withstand loads over the lifetime of the well. Since the cement is pumped as a slurry and then becomes solid, both its fluid and solid properties must be well defined and assessed.

Formation properties that influence cement placement are temperature, pore and fracture pressure, formation type, and formation fluids. According to these, the cement slurry (in liquid form) is designed by considering properties like slurry density, viscosity, thickening time, fluid loss, and free fluid. Finally, when cement is set (solid), its mechanical properties influencing the performance of the cement layer over the lifetime of the well are compressive and tensile strength, elasticity modulus, Poisson's ratio, porosity, permeability, resistance to fatigue, etc.

Figure 12 presents the influence of temperature and pressure on cement strength development in the first 24 hours of curing. In the range of 35 – 77°C and 3.5 – 30 MPa, with increasing pressure and temperature, samples of class H cement develop higher initial strength in less time (shorter WOC time). This behavior is not linear and changes at higher temperatures, where cement strength retrogression (to be discussed further) occurs.

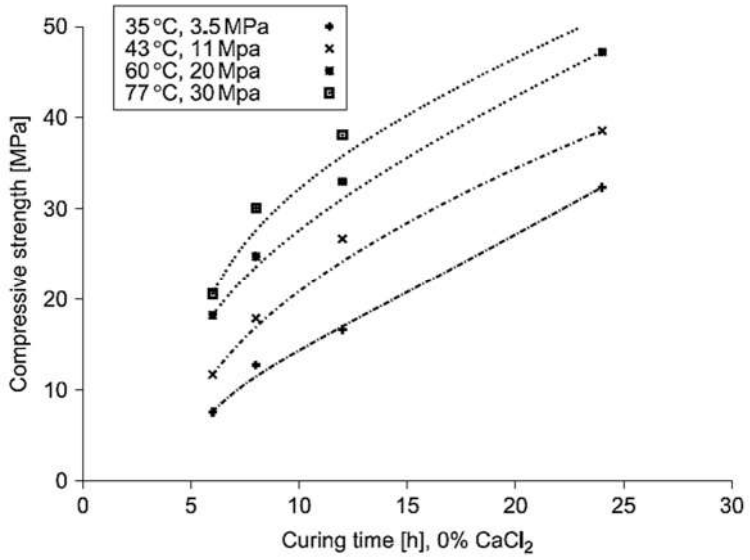

Figure 12 – Pressure and Temperature Influence on UCS over One Day (Fink 2015)

A study by Elkhadiri et al. (2009) on the effect of curing temperature on cement hydration of several samples of different ages shows that mechanical strength closely relates to how and where hydration products precipitate. For instance, low initial rates of hydration (at standard surface conditions) favors controlled precipitation of reaction products in the cement interstitial space. On the other hand, higher curing temperatures accelerate the hydration reactions in early age cement, leading to higher initial compressive strengths. With the increase in time, the same authors noticed a strength decline in pastes cured at 85 °C and a gradual increase in strength of pastes cured at 22 °C and 40 °C. At low placement temperatures, hydration reactions can continue over extended time (De Bruijn et al. 2010).

With technological advancements and increase in the number of high-end applications, special types of cements are tailored to operators' needs. These include (Fink 2015):

- Resin cements, which provide abrasion resistance, impact resistance, better tensile and flexural strength (depending on the curing methods), more resistance

to acids and salts and freeze-thaw cycles, but exhibit a higher porosity and risk of gas migration

- Oil-based cements, where cement particles are kept in suspension in hydrocarbons and only start reacting when they encounter formation water – used as plugging and squeeze cements
- High-temperature cements, where the addition of chemicals like polymers and silica flour or silica fume inhibits cement strength retrogression
- Low-temperature cements contain large amounts of accelerators, freezing point depressants, ethylene glycol, which increase the pumpability at low temperatures, but also the cement resistance to freeze-thaw cycles.
- And other types of cements, still under development: acid gas resistant cement, magnesian cement, fiber cement, etc.

Another development in well cementing worthy of mention is Liquid-Cement Premix – a storable cement slurry that can be maintained in a liquid state for a certain period and consists of a mixture of API cement, set-retarding and conditioning agents, which slow the hydration reaction of cement powder with water. These cements are activated before pumping downhole by means of a special chemical and have shown positive results in environmentally sensitive areas, areas with operations footprint constraints, remote zones, or in situations when deployment of conventional cementing equipment and personnel is unfeasible (Pike 1997; Eid and Mays 2007).

The abundance of combinations between cement types and cement additives can lead to reliable cement layers and integrity-assuring well barriers. Nevertheless, this also

increases the probability of bad practices and errors during the design and service phase, and the necessity of dependable testing.

For example, in some HPHT applications, foam cements are used because of their lower density and improved flow characteristics when compared to conventional cementing systems (Ahmed et al. 2009). In CO_2-rich environments (e.g. carbon sequestration and storage projects or geothermal wells), cements must be designed to withstand chemical degradation through special additives or changes in chemical composition (e.g. high alumina cement), with temperature and time playing a major role in these mechanisms (Omosebi et al. 2017).

At high temperatures, the addition of silica in the slurry prevents strength loss. A loss in compressive strength of neat Portland cements has been reported with the early development of high-temperature wells in the 1950s. A compressive strength loss of up to 50% over 14 days of curing and permeabilities up to 10 md have been measured in cements cured at 160°C for seven days (Saunders and Walker 1954; Patchen 1960). For HPHT conditions, sand and microsilica or silica flour are added to oilwell cements to maintain strength and low permeability at temperatures above 120°C (Eilers and Nelson 1979). This discovery seems to date back to 1934, when Menzel acknowledged that finely divided silica components within Portland cements increases the compressive strength at curing temperatures of 175°C (Patchen 1960). This addition prevents the conversion of the CSH phases to alpha-dicalcium silicate, which yields the decrease in strength and increase in permeability. Such Portland cement blends have been successfully used at temperatures up to 380°C (Doherty and Brandl 2010). Same authors successfully added graphite/metakaolin to standard class G cements to withstand dry heat temperatures of up

to 1000°C in an Australian underground coal gasification project. Furthermore, Noik et al. (1998) noticed that a better control of the dry blend cement/sand/microsilica composition and an optimization of the grain size distribution improves both the HPHT slurry rheological and mechanical properties. In these formulations, because the amount of water is less than the required volume for completing the hydration reaction, some amount of reactive powder (usually calcium silicate and/or microsilica grains) remains in the mixture – giving also the name of reactive powder cements (RPC) to this design approach. An extensive study showed that these formulations perform better than standard oil well cements, as shown in Table 3.

Table 3 – Strength (MPa) of RPC and Class G Cement (Noik et al. 1998)

	Formulation A	Formulation B	Class G Cement
90°C – 3 days			
Compressive Strength	160 ± 13	192 ± 13	57 ± 7
Flexural Strength	20 ± 3	17 ± 2	10 ± 2
140°C – 3 days			
Compressive Strength	137 ± 23	165 ± 29	59 ± 8
Flexural Strength	23 ± 3	28 ± 2	10 ± 1

A - RPC, 20% sand BWOC, 24% microsilica BWOC, w/c 0.27; B- RPC, 35% sand BWOC, 24% microsilica BWOC, w/c 0.27; G - w/c 0.44

Additionally, compressive and flexural strength measurements for samples aged at 120°C for 15 days and 1 year show an increase of approximately 60% in the unconfined compressive strength and a decrease of 30% in the flexural strength of cements cured in deionized water, sea water, and a mixture of seawater and H_2S. No strength retrogression was observed, and RPC cement maintained high strength and low permeability properties under temperature conditions over one year at least (Noik et al. 1998).

For extenders, **Figures 13** and **14** depict the decrease in cement compressive strength with the addition of bentonite. Adding up to 12% bentonite to a mix of class G cement and water decreases the slurry density from 1.9 to approximately 1.5 SG (15.8 to 12.6

ppg). Moreover, bentonite addition leads to low water loss, savings of 15 to 25% in the cost of cementing materials, and additional savings because it reduces the need of performing stage-jobs (Morgan and Dumbauld 1953). Bentonite cements were also recommended for perforation zone cementation because of their lower compressive strength. However, a compressive strength decline by up to 93% due to high bentonite addition renders such a slurry unusable for sealing wellbores, depending on the downhole conditions.

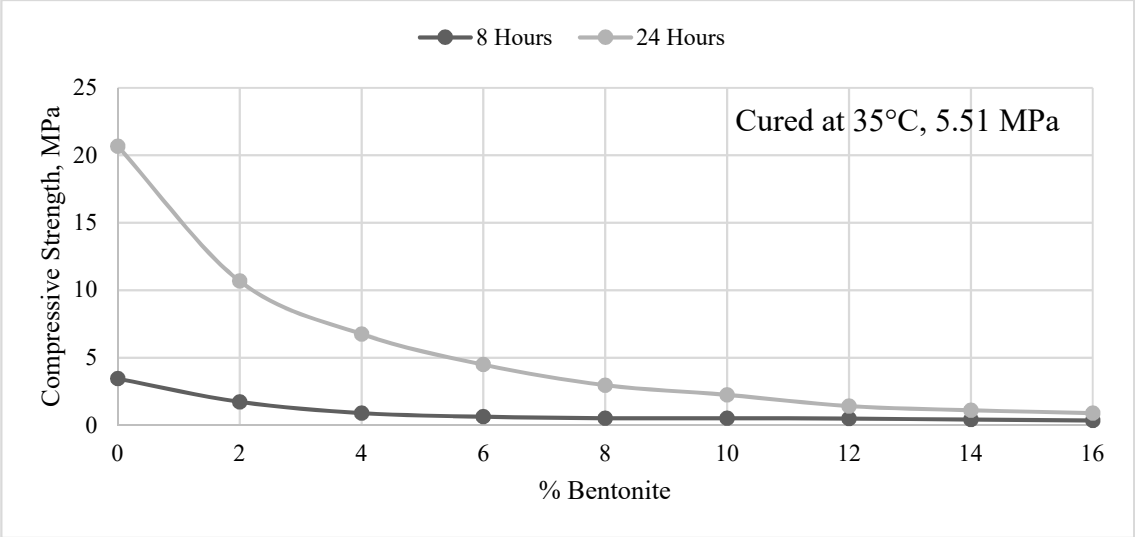

Figure 13 – Compressive Strength as a Function of Bentonite Addition (Halliburton 1994)

With increasing curing temperature and pressure, the overall cement performance in terms of compressive strength is better, showing the importance of exposing cement samples to curing schedules close to wellbore conditions for a true assessment of strength development and cement behavior.

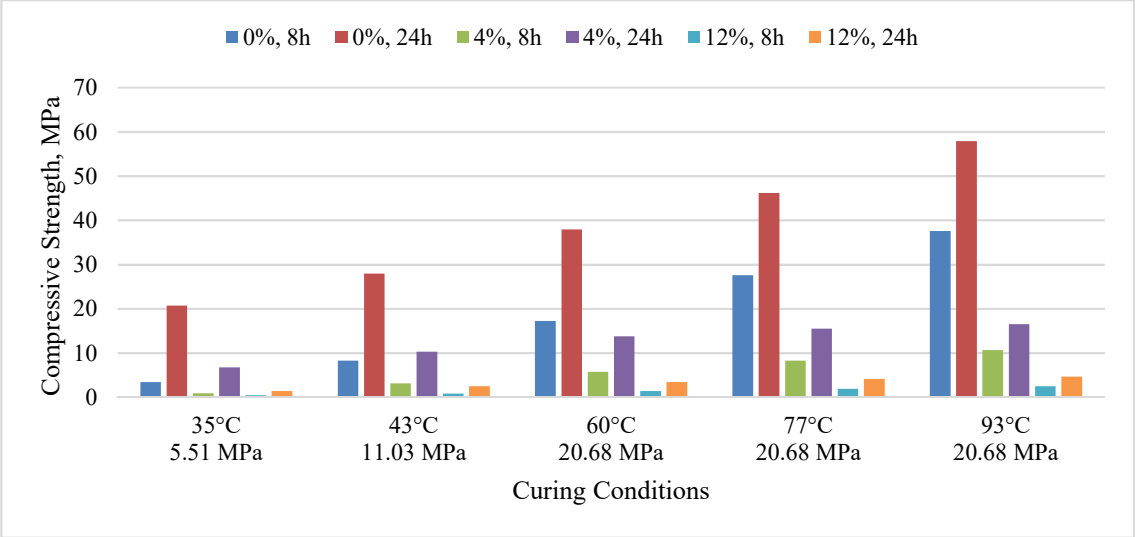

Figure 14 – Compressive Strength of Bentonite Cements cured at Various Conditions (Halliburton 1994)

Cement slurries mixed with Sodium or Calcium salts (NaCl or $CaCl_2$) have been used to mitigate formation salt dissolution due to contact with fresh water, and swelling of clays sensitive to fresh water, and to reduce the freezing point of the slurry during cementing jobs at low temperatures. Salt, in an optimal amount, improves flow properties of cement slurries, and influences the thickening time, increases slurry density, accelerates cement setting and its ability to gain compressive strength, reduces slurry rheology, while being compatible with most other additives (Slagle and Smith 1963). From a chemical standpoint, NaCl can easily penetrate the CSH membrane, formed after the initial contact of cement clinker with water, increasing the accessible area of clinker and leading to a more open and flocculated structure. The rate of formation of ettringite increases due to the presence of chloride ions, which consume the gypsum, accelerating the hydration process (Teodoriu and Asamba 2015).

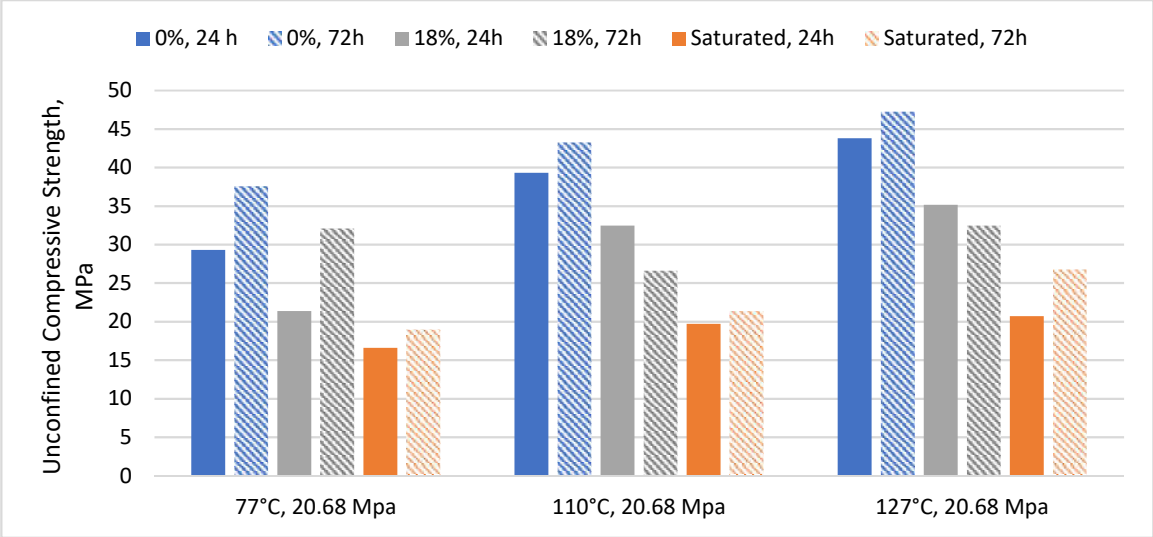

Figure 15 – Compressive Strength of Cements with Salt (Halliburton 1994)

Teodoriu and Asamba (2015) also presented the best and worst development of cement properties in relationship to salt content, showing that for low temperatures, a salt concentration of 5% by weight of water (BWOW) has the best effects on thickening time (7.5 hours), rheology, compressive strength, Young's modulus, and permeability. For higher temperatures, they show that concentrations of salt higher than 25% perform better. Nevertheless, such high salt concentrations have an adverse effect on the other parameters.

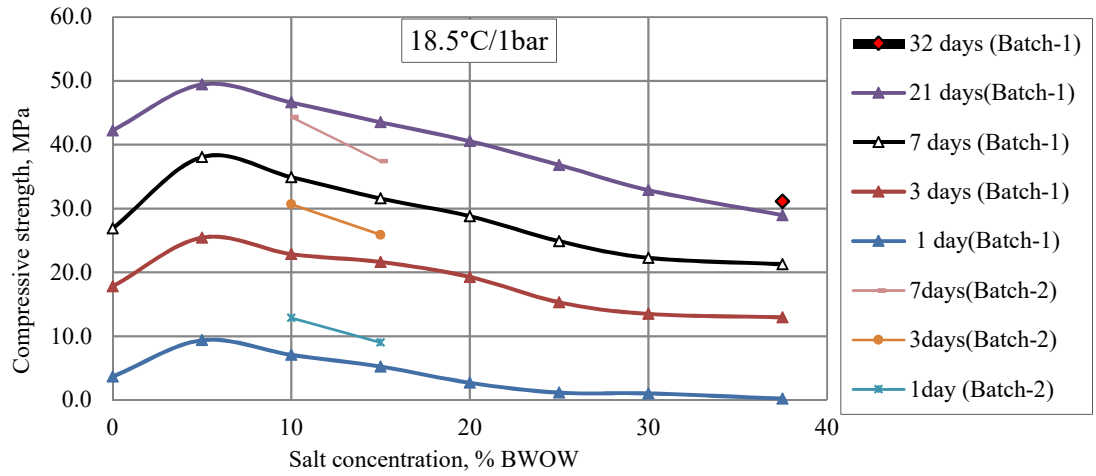

Figure 16 – Compressive Strength Evolution of Class G Cement with Time and Salt Concentration (Teodoriu and Asamba 2015)

As shown in **Figure 16**, a salt concentration of 5% BWOW has the best effects on the compressive strength of Class G cement cured at surface conditions. A salt concentration between 0 and 15% improves or does not affect cement's compressive strength, after which compressive strength decreases by up to 42%.

The experimental assessment of cement properties strongly depends on the materials used, the curing conditions, and the equipment used for the measurements, and of utmost importance to carefully document and explain chosen curing conditions and methods of measurements.

3. Experimental Procedures, Background, and Previous Related Work

Five different cement slurry mixes were cast in cube molds and glass cylinders and were kept at 25°C, 50°C and 75°C, over extended periods. This section covers mechanical, ultrasonic testing, and NMR measurements. Mixing procedures, casting, curing, and measurements of the samples' dimensions are covered in Appendix B. Moreover, the underlying principles of ultrasonic and NMR measurements are covered in Appendices C and D.

3.1. Cement Mechanical Testing

We used the compression testing machine CM-2500 (**Figure 17**), manufactured and calibrated by Test Mark Industries, to determine the unconfined compressive strength of the cement cube specimens. According to the manufacturer, the machine has an accuracy of ± 0.5%. The device applies a uniaxial load to the cement cube at a rate of 72 kN ± 7 kN per minute and measures the force necessary to generate a permanent (or plastic) deformation of the cube. Then, the compressive strength is calculated by dividing the maximum applied force by the measured surface area, which was in complete contact with the load-bearing plate of the load frame. Results are reported to the nearest 0.3 MPa (50 psi) and averaged among samples from the same slurry and tested at the same time (when applicable), according to API RP 10B-2.

$$\sigma = \frac{F}{A} \tag{1}$$

Figure 17 – CM-2500 Compression Testing Machine (Romanowski et al. 2017)

Uniaxial compression tests were run on samples cured for 1, 3, 7, 21, 40, 60, 80, 120, 150, 200, and 300 days. To determine the sample tensile strength, a few samples were tested at early and late times by using the Brazilian test.

Cement layers are subjected to compression and tension, making it important to understand the development of tensile stresses of cement with age. Brazilian test indirectly measures the tensile strength of rocks. Because of its efficiency and simplicity, it is one of the most common tensile strength measurement. In this test, two opposing strip loads, generated through a special fixture, presented in **Figure 18**, load a disc shape specimen of cement with a thickness/diameter ratio of 0.5 to 0.6. The loading, produced by the same machine used in the compressive testing scenario, causes a tensile

deformation perpendicular to the loading direction, which yields a tensile failure. The tensile strength is then calculated as (ASTM International 2016):

$$\sigma_{tensile} = \frac{2P}{\pi DL} \quad (2)$$

Where P is the force at failure (N), D is the sample diameter (m), and L is the sample length (m).

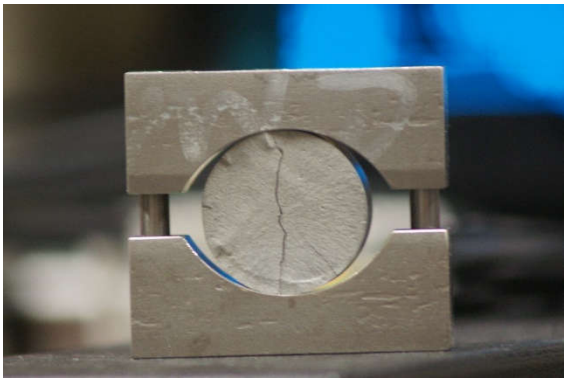

Figure 18 – Brazilian Test Fixture with Split Sample after Testing

3.2. Ultrasonic Measurements

Ultrasonic measurements as a non-destructive method to estimate the strength of oilfield cement started being used in the 1980s, by Rao et al. (1980). The physical principle behind this measurement is constituted by the emission and reception of longitudinal and traverse waves at high frequencies across the sample lengths. The practice of measuring ultrasonic speed in materials is standardized through ASTM E494, ASTM C597, and API 10 B-2. These procedures are recommended for samples with a thickness greater than 5 mm, and smooth, parallel surfaces, to determine their modulus of elasticity, Poisson's ratio, acoustic impedance, shear modulus, bulk modulus, reflection, and transmission coefficients. Measurements can be performed in-situ (e.g. downhole through modern logging tools) or in the laboratory. For oilfield cements and ultrasonic cement analyzers,

depending on the propagation medium, waves travel at different speeds, which are correlated with the sample strength. Other applications of this method are the estimation of concrete strength and the determination thickness for various components (e.g. wall thickness of steel pipe).

3.2.1. Ultrasonic Hardware

An ultrasonic testing apparatus consists of a time base, a set of transmitter and receiver, an A-scan indicator circuit to generate, receive and show electric signals related to the ultrasonic waves. A couplant is used to facilitate the transfer of energy from the transmitter to the sample and from the sample to the receiver. The PosiTector™ ultrasonic couplant has been used for the measurement of longitudinal waves. For the transverse waves measurement, a viscous shear gel produced by Magnaflux for Sonotech has been used.

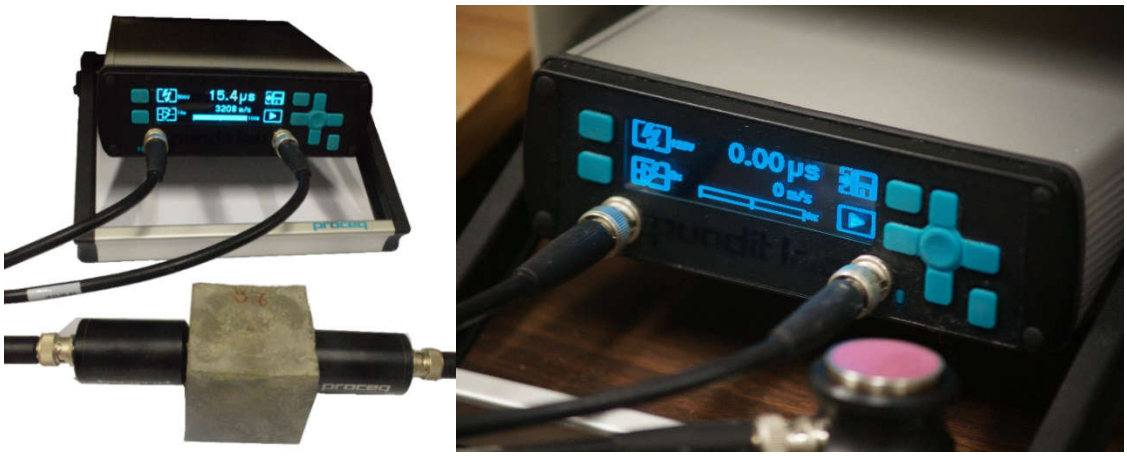

Figure 19 – Proceq™ Ultrasonic Device

Transducers with a frequency of 250 kHz were used for the experiments. Before each set of measurements, the system was calibrated with a reference sample with a transient time of 25.4 µs. **Figure 19** shows the Proceq™ device used in the present research. The

limitations of this device are the testing frequency, temperature and pressure, which are 35°C and atmospheric pressure.

Commercial cement ultrasonic analyzers monitor the development of acoustic velocity at set temperatures and pressures. The machine presented in **Figure 20** can test samples at up to 200°C and 140 MPa by using the same principles outlined earlier in this section (OFITE 2017). By using a linear variable differential transformer, the sample length is measured to an accuracy of ±0.05 mm, reducing measurement errors.

Figure 20 – OFITE Ultrasonic Cement Analyzer (OFITE 2017)

3.2.2. Cement Ultrasonic

Various authors have shown that the ultrasonic response of a cement sample depends on the cement slurry recipe – which influences its density, viscosity, setting time, etc. However, there is no direct correlation between the velocity of the compression waves and the UCS. Consequently, experimental correlations have been empirically established based on UCS values measured by crushing cube specimens of various recipes. This means that these correlations may not be valid when using a recipe that has not already been tested, and some important discrepancies can be observed when using this method on special systems such as resilient cements (Garnier et al. 2007).

Keating et al. (1989) have shown that different cement recipes (containing low CaCl, CaSO4, and bentonite percentages) may generate different ultrasonic responses, mentioning that the cube strength prediction accuracy through ultrasonic measurements is about ±25% of the measured value through conventional crush tests at temperatures between 20 and 50°C. In their work, the authors measure a pulse velocity of 2900 m/s and cube strength of 16 to 21 MPa for neat class G samples cured 24 hours at 50°C, comparable to values acquired in this study. When using 8% bentonite, the measured speed at 24 hours is 2000 m/s and the compressive strength of the samples is between 3.5 to 4.3 MPa. This accuracy is also strongly related to the hardware quality, which improved drastically in the last decades in terms of transducers frequency, sensitivity, and data acquisition system quality and resolution.

Rao's (1980) long-term investigation of the ultrasonic cement response in the presence of additives like bentonite, pozzolan, and hematite, evaluated slurries with densities between 1654 and 2025 kg/m^3, showing that an "average correlation" between longitudinal transit time and compressive strength may be applicable for various cement recipes, providing a "reasonable estimate of the observed compressive strength". At measurements done at elevated pressures and temperatures, only small and predictable changes in the correlations were observed. However, the equation of the used correlation was not published, and the authors only use density as the main parameter of the ultrasonic response. Other similar studies to observe early-age strength development.were done by Labibzadeh et al. (2010) and Shuker et al. (2014).

With improvement in computational technology and testing capabilities, and increased complexity of cementing systems, more correlations can be established and programmed

in laboratory cement analyzing tools to better assess the development of cement mechanical properties.

Romanowski et al. (2017) show how the cement recipe can influence the results obtained through measurements of ultrasonic pulse velocity. It was shown that in the case of bentonite addition, for a UCS below 5 MPa, samples with 4 and 10% bentonite show a very similar relationship between UCS and ultrasonic pulse velocity (UPV, or the velocity of the principal wave -V_p) and different correlation behaviors above the 5 MPa threshold. Moreover, the authors plotted various available correlations (**Figure 21**) and calculated unconfined compressive strength for various speeds, showing the discrepancy between some of the models found in the literature (Romanowski et al. 2017).

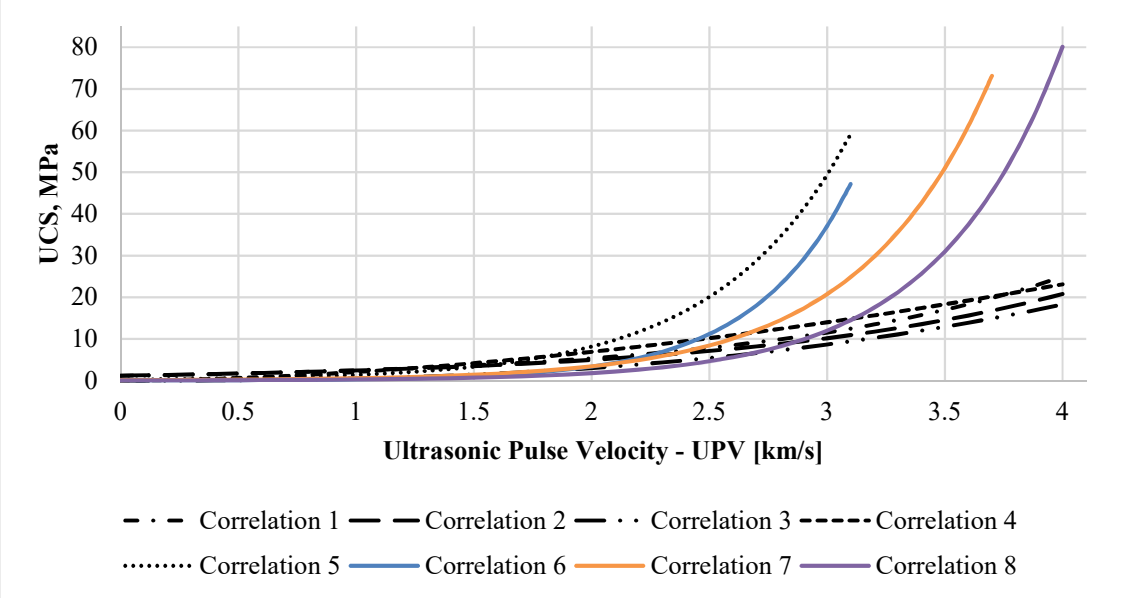

Figure 21 – Calculated UCS According to Various Correlations for Different Cement Types

Table 4 presents the correlations used in Figure 21, with UCS expressed in MPa and V_p in m/s.

Table 4 – Correlations from Figure 21 and Their Coefficient of Determination

Correlation 1	$UCS = 1.146\exp(0.77V_p)$	R^2=0.80
Correlation 2	$UCS = 1.19\exp(0.715V_p)$	R^2=0.59
Correlation 3	$UCS = 8.4 * 10^{-9}(V_p * 10^3)^{2.5921}$	R^2=0.42
Correlation 4	$UCS = 1.2 * 10^{-5}(V_p * 10^3)^{1.7447}$	R^2=0.41
Correlation 5	$UCS = exp[(-3.3 \pm 1.8) + (0.0014 \pm 0.0004)(V_p * 10^3)]$	R^2=0.48
Correlation 6	$UCS = 0.0277\exp(0.024V_p)$	R^2=0.979
Correlation 7	$UCS = 0.0937\exp(0.018V_p)$	R^2=0.9595
Correlation 8	$UCS = 0.0401\exp(0.019V_p)$	R^2=0.982

Correlations 1 to 5 – Cement recipe not mentioned, Correlation 6 – Class G cement, Correlations 7 and 8 – Class G cement with 4% and 10% bentonite BWOC, respectively.

3.3. Nuclear-magnetic Resonance Measurements

Nuclear magnetic resonance (NMR) became a valuable tool in physics, chemistry, and biology since its discovery in 1946 by scientists at Stanford and Harvard universities. NMR tools for petroleum exploration were built as early as the 1960's but did not gain popularity until the beginning of the 1990's (Dunn et al. 2002). In this approach, well logging tools are constructed as 'inside-out' NMR equipment with large static magnetic fields and high-frequency oscillating magnetic fields. The amplitude of the ^{1}H NMR is used to estimate the porosity of the surrounding formation (e.g. fluid content), and the relaxation times are used to evaluate the pore size distribution. When water and hydrocarbon have significantly different relaxation times, the amount of oil/gas can be estimated in-situ. It has been found that the hydrostatic pressure does not have an important influence on relaxation times of water within porous space (Barrie 2000). These principles are further explained in Appendix D.

3.3.1. NMR Hardware

A common NMR setup (see **Figure 22**) consists of two superconducting magnets, shim coils, and a probe which contains the RF coils, and optional, gradient coils. Connected to a computer are: shim power supply, RF source, pulse programmer, a digitizer, the RF

detector, and an RF amplifier. For the gradient coils, a separate amplifier and pulse programmer are used.

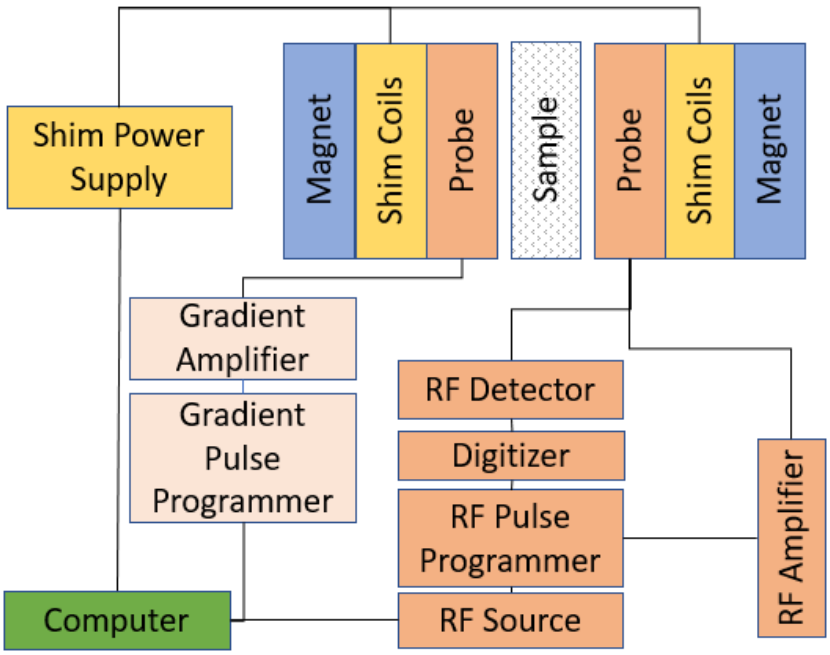

Figure 22 – Typical NMR System Components, adapted after Hornak (2017)

Figure 23 – NMR System Used in Present Work

We used a GeoSpec2 NMR system, manufactured by Oxford Instruments (**Figure 23**). This operates at a frequency of 2 MHz, similarly to. NMR logging tools, and is paired with the Green Imaging Technology (GIT) software, enabling hardware control and samples database access. Before running a series of measurements, the system is calibrated with a pre-configured calibration sample (see Appendix D).

3.3.2. NMR Data Acquisition

Two T_2 measurements, $T_1 - T_2$ measurements and DHK SPRITE (gradient measurements for saturation profile distributions) have been acquired for samples mixed with different additives and cured at various temperatures and times. Some of the common parameters necessary to define experimental conditions are:

- Tau, τ, (ms) – the time between the 90° pulse and the first acquired echo. Usually set to a minimum, 57 μs, it defines the fastest resolvable relaxation time.
- T_{2max} (ms) – the maximum expected T_2 in the sample. Used, together with Tau, τ, to compute the necessary echoes number.
- Recycle Delay (ms) – the time from the end of a scan to the start of the next signal acquisition. Must be five times T_1max for accurate results.
- Hydrogen Index – the amount of hydrogen atoms per unit volume of the detected fluid compared to that of water
- Number of Echoes – calculated as $5T_2/(2\tau)$

For the gradient measurement used for the saturation profile distributions, additional necessary parameters are:

- Sequence – NMR sequence used to acquire signal (DHK was used in this work)
- Field of View -the length of the saturation profile acquired

- Resolution – the number of points defining the profile
- Encoding Time – the duration between the excitation pulse and acquisition
- Flip angle – excitation flip angle

The cement samples poured in glass vials are used for the NMR tests. Since they are kept under water, a damp paper towel is used to remove excess surface water and the glass cylinder is capped with a sealing glass piece covered in Teflon tape to prevent. water evaporation during long tests. Usually, the samples are placed in the NMR spectrometer after the observed temperature at the surface of the sample (measured with an infrared thermometer) is close to the room temperature.

To make sure that the cement-glass contact does not influence the acquired data, separate measurements for samples poured in vials and samples taken out of vials after a few days of curing have been performed and show consistency within 1%. Moreover, testing has been performed on samples cored from cubes, and results are reproducible. Since samples' casting took place at different times, the evolution of the samples' response and their reproducibility has been assessed to check for results reproducibility, which may be influenced by cement powder variations, water variations, mixing technique, and small differences in the exact timing of measurement after casting.

More than 1000 tests have been performed at different times on various samples.

T_2 *relaxation time*s are commonly acquired through a spin-echo sequence, such as the Carr-Purcell-Meiboom-Gill (CPMG) method (90°- τ -180°- τ). Accurate T_2 values depend on the static magnetic field strength and the length of the echo spacings.

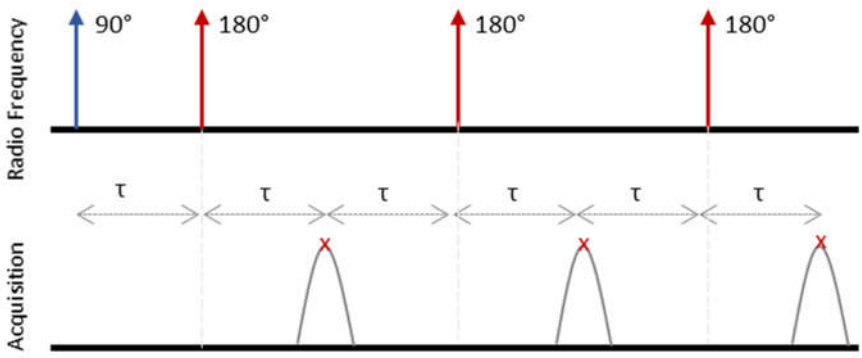

Figure 24 – CPMG NMR Sequence (redrawn after GIT 2016)

Since each 180° pulse produces a signal echo and its peak amplitude decays at a rate of T_2, for materials with multiple decay constants, the governing equation is:

$$S(t) = \sum_{i=1}^{N} A(i) e^{\frac{-t}{T_2(i)}} \quad (3)$$

N – number of T_2 relaxations, $A(i)$ – amplitude of signal at each relaxation value

$T_1 - T_2$ *Measurements* use a combination of inversion recovery and CPMG pulse sequence to acquire the data. The figure below shows how first, a 180° inversion recovery radio frequency is applied. After the inversion time (TI), a 90° excitation RF is applied, and the first T_1 signal is acquired. After a set time (τ), the echo sequence begins, and another 180° pulse is applied, which is followed by acquisition and the next pulse (after TE, or echo time, or 2τ)

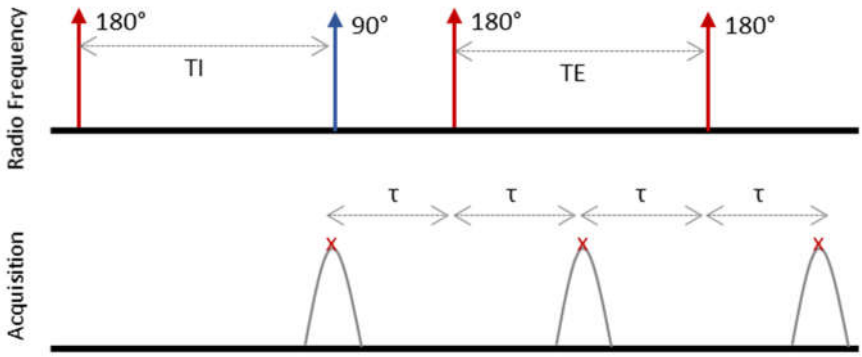

Figure 25 – T_1-T_2 NMR Sequence (redrawn after GIT 2016)

Saturation Profile Measurements use the double half k-space (DHK) SPRITE method. Data are sampled in one half of the k-space by incrementing the gradient, then, after a relaxation delay of $5 \times T_1$, the data in the second half of k-space are sampled by incrementing the gradient in the opposite direction, as shown in **Figure 26**. Data acquisition is performed between the RF pulses.

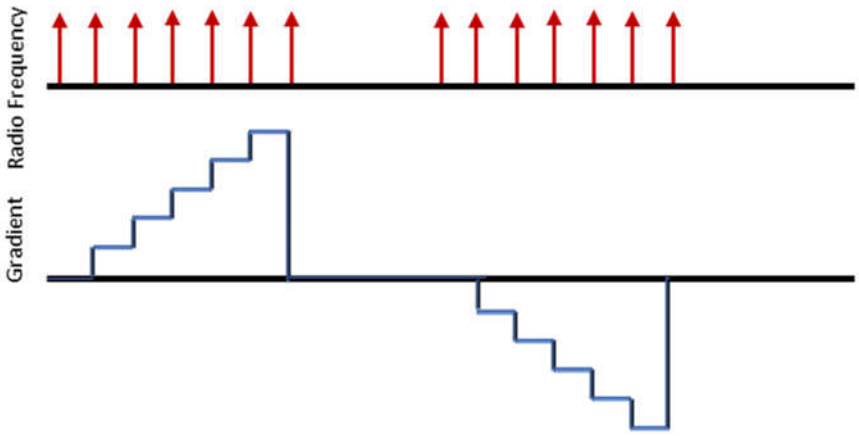

Figure 26 – DHK Sprite NMR Sequence (redrawn after GIT 2016)

3.3.3. Cement NMR

As shown in chapter two, water is an integral part of the cement hydration reaction and its microstructure, so its removal to characterize various properties (e.g. cement porosity, pore size distribution) is not recommended, reason why NMR measurements on cement pastes gained in popularity over the last 40 years as a nondestructive and noninvasive measurement method. Measurements can be repeated on the same sample, which reduces errors stemming from sample variability, and since no drying is required, the sample microstructure is not damaged. However, because of relatively large quantities of paramagnetic impurities (especially in the so-called gray cements), signal times are

shorter compared to other mediums, which adds to the experimental complexity (Valori et al. 2013).

The first analysis of cement pastes by ^{1}H NMR dates to 1978, when Blinc et al. (1978) measured T_1 and T_2 relaxation times of adsorbed water in Portland cement (w/c ratio of 0.42) and tricalcium silicate pastes at room temperature for up to 28 days at a frequency of 60 MHz. A sharp decrease of relaxation times in the first 3 hours of measurements was noticed, with stabilized values after 24 hours. The initial measured T_2 value of 2 ms was tracked up to 10 h of hydration and showed a decreased to 0.7 ms. They concluded that T_1 and T_2 decreased with increase in hydration due to the increase in the active surface and the number of adsorptive sites, showing that NMR is a convenient tool to study the hydration process (Blinc et al. 1978).

Schreiner et al. (1985) used different measurement methods to track relaxation times during hydration and quantified different magnetization factors of water in micropores, solid gel, and solids representing hydroxy groups (e.g. $Ca(OH)_2$). The measurements were done at 38 and 19 MHz on cement pastes mixed with 0.33 and 0.63 water BWOC and cured for almost 1 year in an environment with 70% humidity (Schreiner et al. 1985). Three years later, more hydrogen components were identified by Lasic et al. (1988) through T_1 measurements, distinguishing hydrogen in CH, aluminate, adsorbed water, CSH, and near paramagnetic centers (Muller 2014). Greener et al. (2000) monitored spin-spin relaxation on white cement as a function of time and resolved the multiexponential behavior of measurements in cement pastes, reporting T_2 relaxation times for the fractional magnetizations. They mention that the proton magnetization factor is proportional to the number of spins which make up a group of protons, allowing the

monitoring of cement constituents with hydration time. A 26 MHz system was used to run FID and CPMG sequences on samples mixed with a w/c ratio of 0.42. Based on the acquired signals, five distinct spin groups were resolved and components were assigned T_2 relaxation times, with a good correspondence between NMR results and known chemical reactions and stoichiometric changes within cement structure during hydration. To determine the surface relaxivity of cements, Dalas et al. (2014) used NMR and gas adsorption measurements (Brunauer-Emmet-Teller, BET) on individual hydrated components equivalent to the ones found in a hydrating cement paste and applied the acquired data in the biphasic fast exchange model. By plotting transverse relaxation rate (T_2) versus surface water fraction (calculated with BET), they found that at all tested phases except for ettringite have surface relaxivities close to common values for rocks at early stages of hydration. The following values were found for anhydrous and hydrated phases.

Table 5 – Surface Relaxivity of Cement Components, after (Dalas et al. 2014)

Phase	Formula	BET Specific Surface Area (m^2/g)	Surface Relaxivity (µm/s)
Crushed Calcite	$CaCO_3$	0.7	5.04
Synthetic Calcite	$CaCO_3$	21.1	2.74
CSH	$CaOSiO_2H_2O$	101	5.51
Ettringite	$Ca_6Al_2(SO4)_3(OH)_{12}26H_2O$	10.8-17.3	38.5-44.7
Gypsum	$CaSO_42H_2O$	0.22	6.2
Monocarboaluminate	$Ca_4Al_2O_6CO_311H_2O$	26.5	1.65

Work done on the distribution of pore sizes, total surface area, and consumed water is observed by Halperin et al. (1994) who used Laplace inversions on CPMG data and application of the fast exchange model on a white cement paste (w/c = 0.43). Spin-spin (T_2) relaxation was continuously monitored for up to 60 days, showing two different pore

populations (capillary and gel pores) and their evolution with time (**Figure 27**). The authors define the radius of gel pores between 1 nm and 6 nm, and the capillary pore radius between 0.01 μm and 0.02 μm over the measurement period.

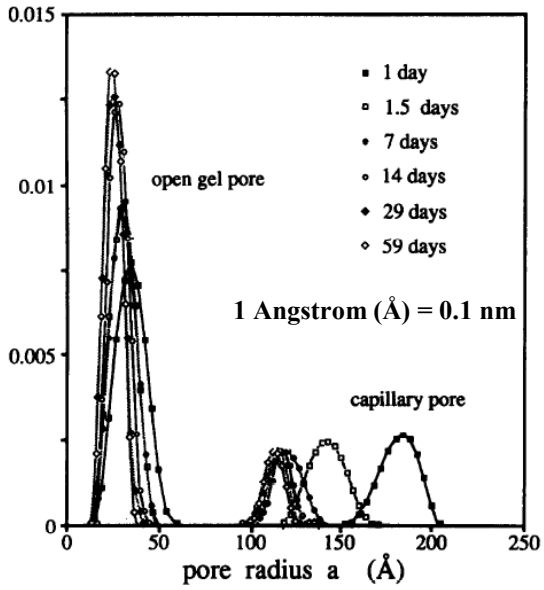

Figure 27 – Pore Radius Evolution with Time (Halperin et al. 1994)

Using T_2 measurements supported by XRD measurements of the degree of hydration and ettringite mass fraction, Muller et al. (2012) updated Powers' hydration model by proving the nonlinear growth of the gel porosity and differentiating between CSH and calcium hydroxide while separating the interlayer water within the CSH. According to the authors, gel pores have a size of 3 – 5 nm during the first few days of hydration, and capillary pore diameters starts at around 10 nm. Based on their findings, Königsberger et al. (2016) developed an analytical hydration model related to the evolution of clinker, solid hydrates, and gel and capillary porosities as functions of w/c and degree of hydration, and suggest that CSH density governs the different mass fractions of different bound water in cements due to the available precipitation space.

$T_1 - T_2$ correlation experiments have been performed by McDonald et al. (2005) at an NMR frequency of 20 MHz, proving for the first time the exchange of water between gel and capillary pores occurring over the first 14 days of white cement paste hydration, and supportive evidence for the surface diffusion model and for a multimodal pore size distribution. The effects of silica fume paste additions were also evaluated. Popular for fluid typing (differentiating between oil, water, and gas), T_1-T_2 measurements can couple nuclear spin relaxation with relaxation or self-diffusion at subsequent timesteps.

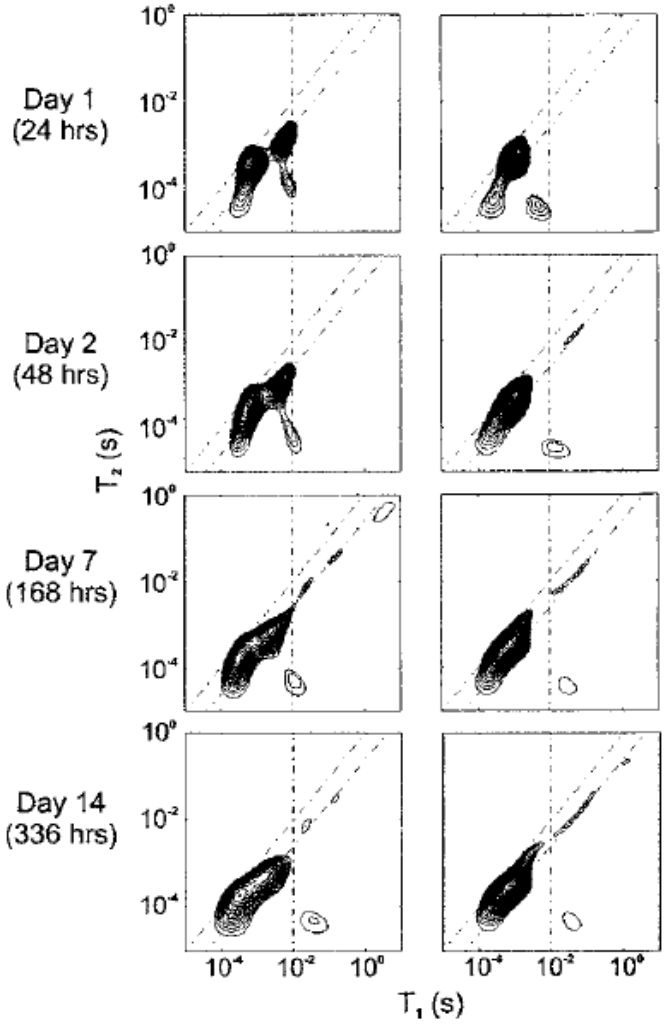

Figure 28 – White cement sample (left), cement and silica (right) spectra (McDonald et al. 2005)

McDonald et al. describe the T_1 and T_2 relaxation times for water confined in the previously described cement pores as follows:

Table 6 – Relaxation Times of Water in Different Pores, after McDonald et al. (2005)

Type	T_1	T_2	Comment
Bound water	>100 ms	~ 10 μs	Chemically combined in the CSH gel – no mobility
Water in gel pores	0.5 – 1 ms		Relaxation heavily dominated by surface reactions – more mobile
Water in large capillary pores	5 – 10 ms		Much less than the bulk liquid times

In an extensive overview of NMR measurements performed on cements, Valori et al. (2013) conclude that numerous experiment lead to the consensus that in T_2 measurements of white cement pastes at 10-20 MHz, the CSH interlayer water (bound water) has a relaxation time of the order of 100 μs, whereas gel water finds itself in pores of 2 – 5 nm and has a relaxation time of 300 – 400 μs. The total volume of free water (water in large capillary pores) decreases throughout the curing process and after 1-2 days of hydration, most of the water is in pores of about 10 nm, the number of capillary pores being smaller than expected, probably due to desiccation (which empties the pores). Full capillary pores can be achieved by curing small samples under water, case in which the capillary pore total volume is still small (5%, or 33 to 50% of what Powers' model predicts).

SPRITE measurements have been used to monitor the freeze-thaw cycle in concrete, which makes use of the fact that the T_2^* of ice in concrete is very short (<9 μs) that the proton signal will not be observed from ice, and therefore only unfrozen water will be imaged the experiment, providing insights into the dynamics of this process, detrimental to concrete strength and integrity (Muir and Balcom 2012).

NMR measurements offer novel and unique insights into cement properties. Relaxation measurements performed on cements by multiple researchers show similar observations but also notable differences. Most of the published works agree that after mixing, there is a single T_1 and T_2 component characteristic to the bulk water, which then evolves into a multi-modal distribution. Different components are associated with the different forms of water (within capillary pores, gel water, CSH water, and water bound to solid phases), and relaxation times seem to be in line with the development of hydrate phases and micro- to nano-pores. Observed differences can relate to sample composition (powder, w/c ratio), curing conditions and age, measurement conditions (measurement frequency, τ, etc,), data analysis methods, and NMR hardware. For example, grey cements exhibit shorter and more homogeneous relaxation times than white cements, which in turn are shorter than those in C_3S or synthesized CSH. The w/c ratio of the mixture influences the initial content of capillary water, leading to differences in the relaxation times, as well as the type of curing: sealed, open to a dry environment, or open underwater (Valori et al. 2013). Moreover, curing temperature can also influence the NMR response.

Not a lot of effort has been spent in understanding oilfield cements from the same perspective as the concrete industry or cement manufacturer. Maharidge et al. (2016) designed an intra-laboratory test program for Class G cement to better comprehend when and if micro-texture changes can be observed and correlated to mechanical and flow properties, when these responses become steady, and if the water in the cement correlates to these observations. They acknowledge that ambiguity is encountered when studying the water content of hydrating cement pastes because the water that chemically reacts and/or is adsorbed to the solids' surface has a different T_2 relaxation than the unreacted

water. After 3 hours of hydration, they report a T_2 peak of 10.6-10.9 ms, which shifts to 0.35 ms after 8-10 days, reaching steady state. The reduction of the area under the T_2 spectrum, related to the total water content in the sample, is attributed to the ongoing chemical reactions, which transform the hydrogen available in water in chemically bonded hydrogen, implying that the areas might be divided in reacted and unreacted water. This hypothesis would necessitate an independent measurement of connected and unconnected porosity, to determine a common T_2 cutoff value for each sample. Moreover, the authors correlated T_2 spectral peaks with permeability measurements done in a Hassler-type core holder, and their results support the idea that permeability decreases because of a decrease of porosity and an increase in the number of small pores. Their NMR measurements were performed using a Geospec II 2 MHz NMR rock core analyzer from Oxford Instruments (Maharidge et al. 2016).

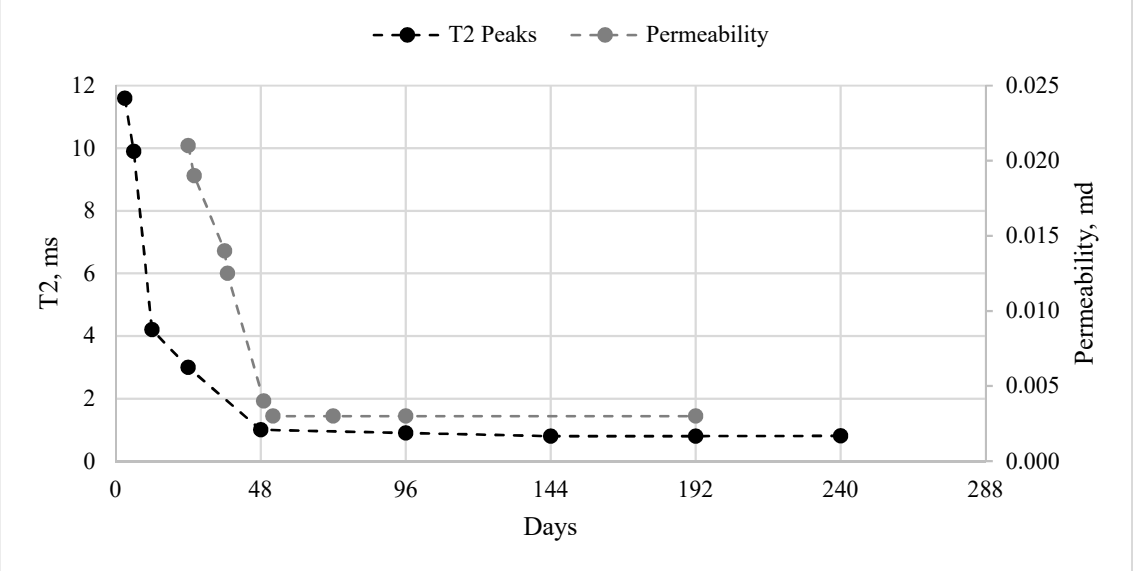

Figure 29 – Monitoring of T₂ Peaks and Permeability of Class G Cement (Maharidge et al. 2016)

Other acquired data correlated with the T_2 peaks and T_2 NMR water content included unconfined and confined compressive strength, tensile strength, and Young's modulus over 10 days, and the authors drew conclusions on what properties may or may have not reached a plateau in their evolution.

Through this work, a better evaluation of long-term water content evolution in cement samples cured at various temperatures is attempted.

4. Acquired Data and Analysis

4.1. Samples Conditioning

The following cement slurry recipes were mixed on different dates by the procedure outlined in Appendix B.1. and are summarized below and in Table 7:

- Neat Cement – CN – Class G cement mixed with 44% water by weight of cement (BWOC)
- 4% Bentonite Cement – CB4 – Class G cement mixed with 4% bentonite powder BWOC and water in excess (65.2% water BWOC)
- 10% Bentonite Cement – CB10 – Class G cement mixed with 4% bentonite powder BWOC and water in excess (97% water BWOC)
- 4% Salt Cement – CS4 – Class G cement mixed with 44% brine BWOC containing 4% salt (salt added by weight of water – BWOW)
- 12% Salt Cement – CS12 – Class G cement mixed with 44% brine BWOC containing 12% salt (BWOW).

Table 7 – Cement Recipes

ID	Cement mass g	Water mass G	Bentonite mass g	Salt mass g	Calculated Density SG
CN	792	348.5	-	-	1.9
CB4	608	396.5	24.3	-	1.71
CB10	451	437.6	45.11	-	1.56
CS4	773.4	340.2	-	13.6	1.88
CS12	737.9	324.5	-	38.9	1.85

4.1.1. Slurry Density

The post mixing densities of the slurries were measured by using an oilfield balance. Table 8 gives a comparison between the calculated and the measured densities, showing good agreement. If the measured density of a slurry was different by more than 0.3 s.g., it was not used in the casting process.

Table 8 – Cement Slurry Densities

Cement	CN	CB4	CB10	CS4	CS12
#1	1.89	1.68	1.52	1.9	1.87
#2	1.9	1.69	1.54	1.89	1.86
#3	1.91	1.69	1.53	1.89	1.89
#4	1.9	1.7	1.54	1.87	1.89
#5	1.88	1.69	1.53	1.88	1.87
Average	**1.896**	**1.69**	**1.532**	**1.886**	**1.876**
Calculated	**1.9**	**1.7**	**1.54**	**1.88**	**1.85**
% Difference	0.21	0.59	0.52	0.32	1.4

4.1.2. Samples Geometry and Associated Error

The dimensions of the samples are determined by using a Vernier caliper and the procedure from Appendix B.3. For the *cube* samples, the standard error of the length measurements is calculated to be ±0.003 mm (standard deviation of ±0.08 mm for a population of 552 measurements), whereas for the width, the standard error is ±0.065 mm (standard deviation of ±1.41 mm for 465 measurements). The latter is larger because the width edge corresponds to the top of the cement, where shape irregularities were difficult to control. The two lead to a standard error for the area of the cube equal to ±0.066 mm^2. For the cylindrical samples, the standard error for the cylinder length measurement is ±0.14 mm, with a standard deviation of ±3.26 mm from 220 sample measurements. The glass cylinders are standardized and their diameter does not show notable variations from the producer given dimension, as also confirmed by laboratory measurements.

The dimensions of sample slices cored and cut for indirect tensile strength measurements exhibit a standard error of ±0.004 mm for the diameter and ±0.006 mm for the length.

4.2. Mechanical Testing

Various batches of samples were tested over approximately 2 years. The first test series, of samples kept at room temperature, started in September 2015 and concluded in November 2017, the oldest samples being 300 days old. Because these samples did not need special curing conditions, and space was not a constraint, a large number of specimens was tested.

The samples cured at elevated temperatures were initially mixed in May 2017 and kept until November 2017. These were initially tested in September 2017, when a new batch of samples was mixed to test the same recipes at a younger age but same temperatures. To confirm results, an additional batch of samples has been mixed in October 2017. Because of logistical constraints, with only four water baths being available, a smaller number of samples was kept at higher temperatures, leading to a smaller samples pool to average from. To determine the error for these measurements, four to five samples from the same recipe and batch, kept at the same temperature, were tested at the same day. The following standard errors were calculated for samples from various recipes, cured at 50°C for approximately 180 days.

Table 9 – Unconfined Compressive Strength Standard Error and Deviation

Recipe	Name	UCS Standard Error	UCS Standard Deviation
Neat	CN	0.57	1.14
4% Bentonite	CB4	0.56	1.12
10% Bentonite	CB10	0.9	2.01
4% Salt	CS4	4.42	9.93
12% Salt	CS12	2.75	6.15

4.2.1. Unconfined Compressive Strength Results

Because of the time, temperature of curing, and different recipes used, there is more than one way to represent the experimental data acquired in this study. Same cement recipes can be compared at different temperatures over the same time, their evolution can be tracked at longer times than that recommended in various standards, and the performance of different cement recipes can be compared at the same or different temperatures. The following graphs presents the evolution of Unconfined Compressive Strength (UCS) over time at 25°C, 50°C, and 75°C.

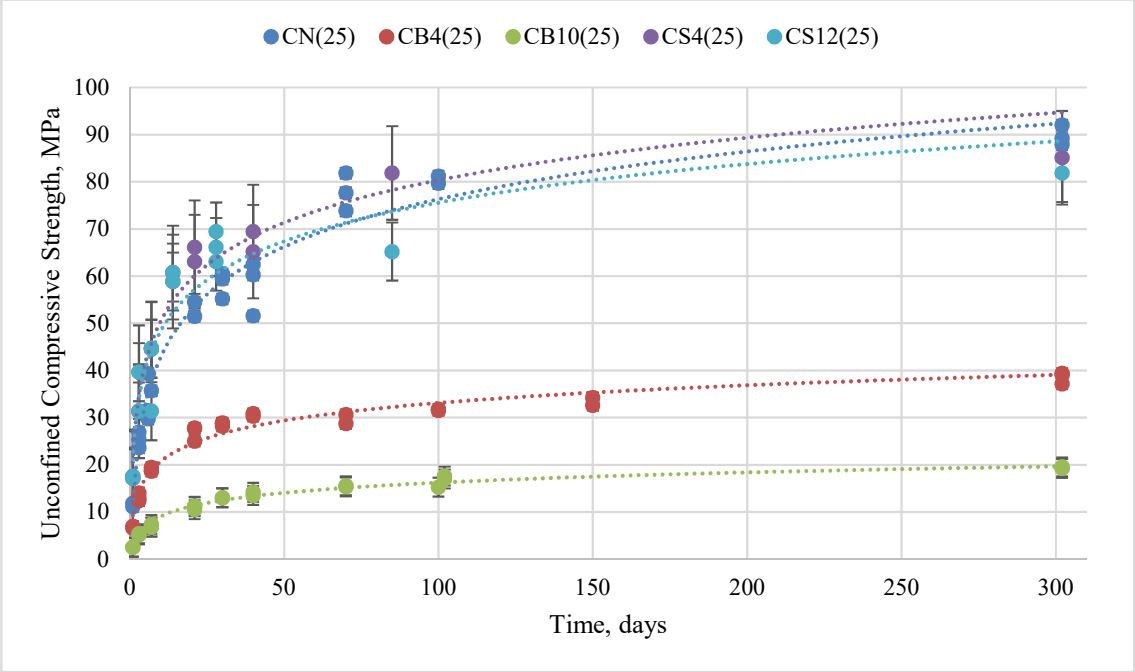

Figure 30 – Unconfined Compressive Strength Evolution with Time at 25°C

At 25±2°C, the most increase in strength is observed within the first 40 days for all samples (see **Figure 30**). Comparable results are observed for neat Class G cement and cements mixed with salt (4 and 12%). The addition of 4% bentonite BWOC reduces the ultimate UCS of the cement by 55%, whereas 12% bentonite reduce the compressive

strength by 78% at day 300. An additional gain in strength is noticed past day 40 for the neat and salt cements, where the UCS increases by 20% until day 300. All 5 evolutions for the various cement recipes exhibit a logarithmical increase of the form $UCS = a * ln(Age) + c$ (where c is the compressive strength at day 1) with high R^2 values, as shown in Table 12 (UCS in MPa, Age in days).

Table 10 – Equations Describing Cement Strength Evolution With Time at 25°C

Cement Recipe	Describing Equation	R^2
Class G Neat	UCS = 14.572ln(Age) + 9.2199	0.97
4% Bentonite	UCS = 5.3978ln(Age) + 8.2538	0.97
10% Bentonite	UCS = 3.1265ln(Age) + 1.8179	0.99
4% Salt	UCS = 12.998ln(Age) + 20.502	0.96
12% Salt	UCS = 11.825ln(Age) + 21.126	0.89

These effects are not as obvious at higher temperatures, where the exothermic nature of the hydration reaction is influenced by the curing temperature. In this case, the different recipes show an increase in compressive strength until days 21-28, after which, deviations from the expected trend are observed.

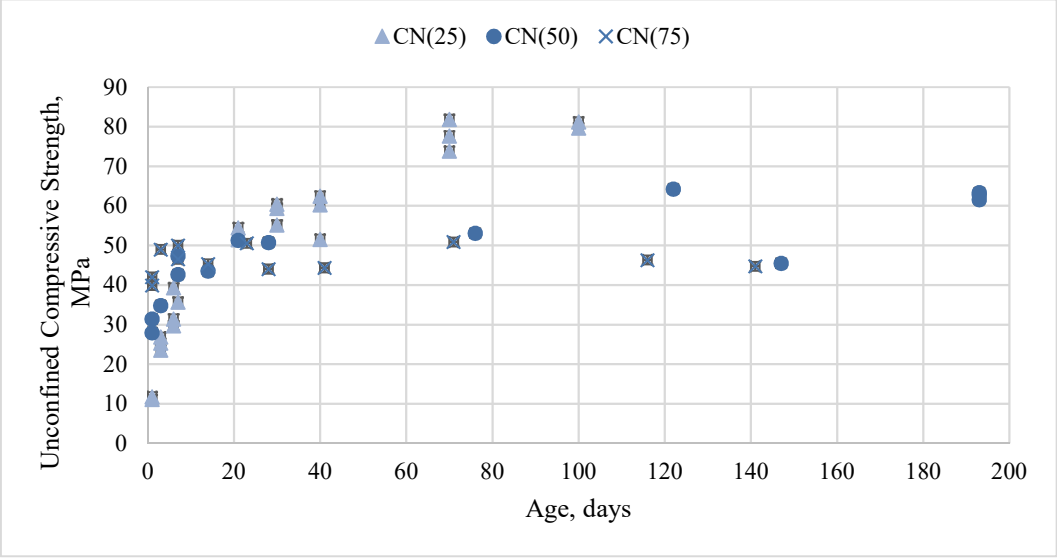

Figure 31 – Comparison of Neat Cement at Various Temperatures

In the case of neat cement, the samples cured at different temperatures show comparable results until day 21, after which the samples cured at 25°C and 50°C exhibit a further increase in their UCS, whereas a small decrease in the compressive strength of the samples cured at 75°C is observed. The final strength of samples cured at the lowest temperature of the three is the highest (see **Figure 31**).

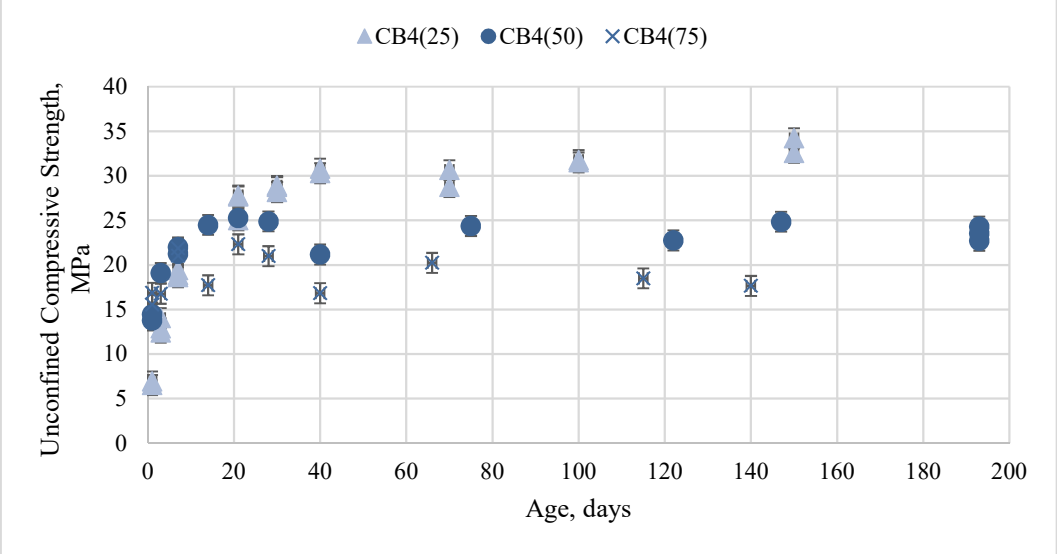

Figure 32 – 4% Bentonite Cement at Various Temperatures

A similar tendency is observed in the samples containing 4% bentonite BWOC (**Figure 32**), where after 21 days the compressive strength continues to increase in samples cured at 25°C, remains constant for samples cured at 50°C, and slightly decreases in samples cured at the highest temperature of 75°C. For the samples with 10% bentonite, increasing temperature leads to a lower final compressive strength and different evolutions starting day 21 (**Figure 33**).

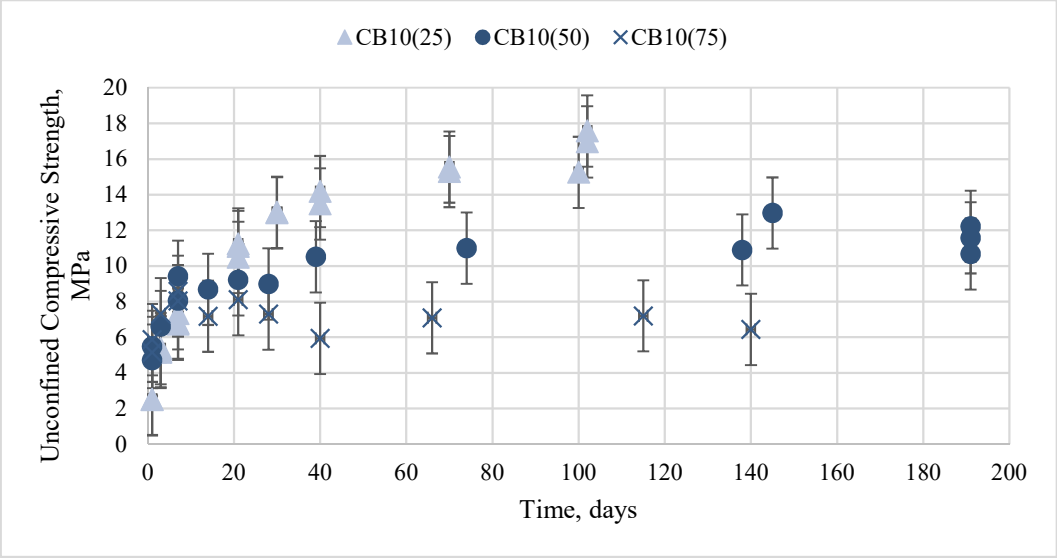

Figure 33 – 10% Bentonite Cement at Various Temperatures

In cements with 4% salt BWOW, different behaviors can be observed starting day 14, after which samples cured at 25°C continue to gain in strength, whereas samples cured at higher temperatures exhibit comparable UCS values until day 200. In samples containing 12% salt BWOW, a greater decrease in the UCS of samples cured at 50°C and 75°C is observed.

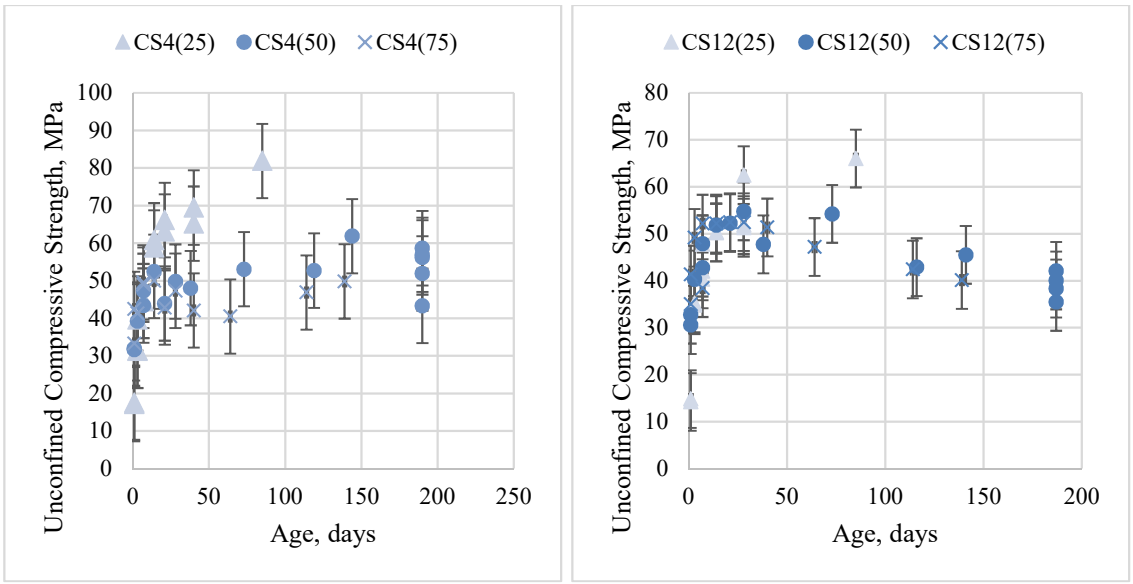

Figure 34 – 4% (Left) and 12% (Right) Salt Cement at Various Temperatures

Qualitative analysis of Figures 31 to 34, indicates that for all five cement recipes, an increase in temperature leads to higher initial UCS (at day 1), but lower UCS values as time advances. All cements show comparable values up to day 28, which is also commonly used as the last day in compressive test testing over extended timeframes, after which values either decrease (Neat and 4% Salt Cement) or stay constant (4% and 10% bentonite, 12% salt).

4.2.2. Indirect Tensile Strength Measurements

For the measurement of tensile strength of samples cured at 50°C and 75°C, the procedure outlined in Chapter 4.4. has been used. Brazilian tests were used to measure tensile strength of samples cured at 50ºC and 75ºC. Samples were removed from their water baths and cored from the cubes by using a 1-inch diameter coring bit, and then polished on a coarse (40-grit) and fine (120-grit) sandpaper. Care was taken to avoid induced cracks. Samples were labeled according to age, as shown in Table 11, with the shorter time corresponding to the 75°C samples, which were mixed later. Two samples were tested for each temperature and age, and reported results were averaged.

Table 11 – Ages of Tensile Strength Samples

Sample	A	B	C
75°C – 50°C	12-13 days	63-73 days	180-190 days

Figure 35 shows a comparison of the tensile strength for all tested cements at different times and temperatures. The maximum tensile strength acquired is 7.9 MPa for the neat class G cement cured at 50°C for approximately 190 days. The same cement recipe shows a lower compressive strength at 75°C. The bentonite cements (B4 and B10) exhibit lower tensile strength, ranging between 3 and 6 MPa, whereas cements mixed with salt show

tensile strengths averaging at approximately 5.5 MPa (4% Salt) and 4.5 (12% Salt) MPa. In all cases, the higher temperature led to a lower tensile strength. No obvious trends were observed with different times.

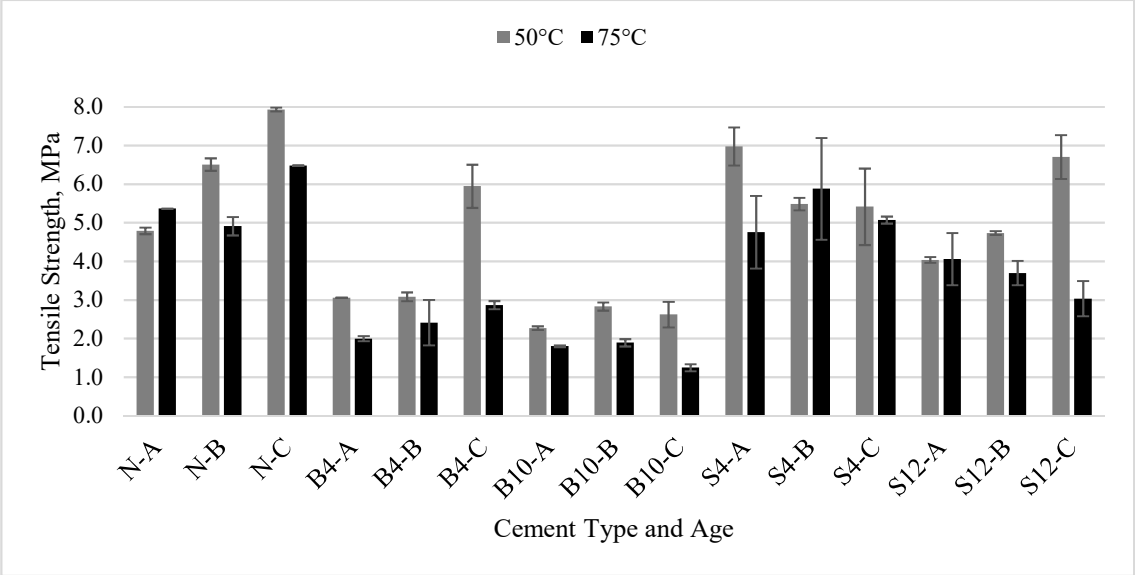

Figure 35 – Tensile Strength Measurement Results

4.3. Ultrasonic Testing

Measurements of V_P and V_S were performed using the Proceq™ equipment presented in Chapter 3.2.1. and analyzed in the Punditlink™ software provided by the same manufacturer. This allows picking the arrival times, as shown in the following signal curve exported from the software (**Figure 36**). Here, *t1* represents the arrival time of the compressional wave, and *t2* is the arrival time of the shear wave. The software allows picking time to within ±0.1 µs and care was taken to ensure consistency (see **Figure C1** in Annex C for additional examples of the signal curves).

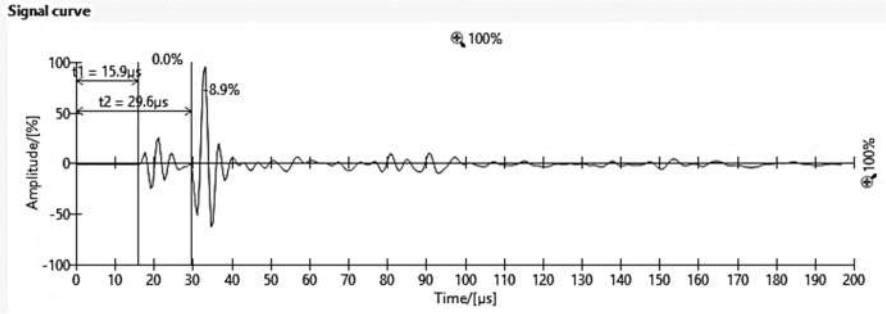

Figure 36 – Signal Curves as Acquired from PunditLink™

4.3.1. P-Wave

In the following, the correlations between the acquired compressive strength values and the ultrasonic pulse velocities will be presented.

A correlation for all data points acquired at all curing temperatures throughout this work is presented in **Figure 37**. The data follow an exponential behavior proposed by previous authors and offers a coefficient of determination of 0.93. The governing equation can be used for cement recipes containing bentonite and salt, or no additives at all (UCS in MPa and Vp in m/s), and is similar to the ones presented in Table 4.

$$UCS = 0.3622e^{0.0014Vp} \quad (4)$$

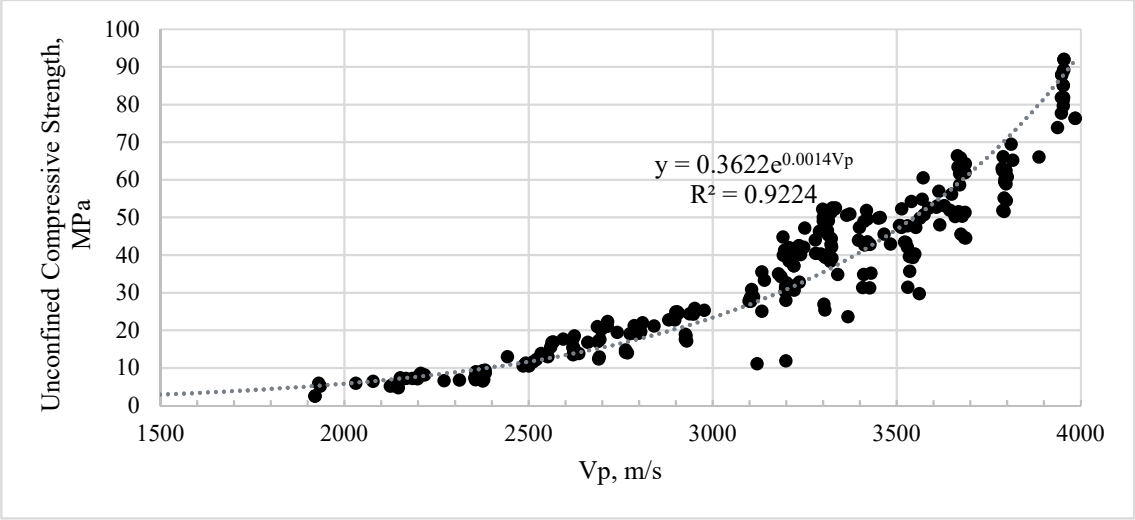

Figure 37 – UCS vs. V_p – All Samples – All Temperatures

When plotting the calculated compressive strength versus the measured data points, it is observed that at compressive strengths between 5 and 25 MPa, the presented correlation performs well, but large deviations from the 1:1 line are observed at UCS values between 25 and 95 MPa, as the general correlation overestimates the cement strength.

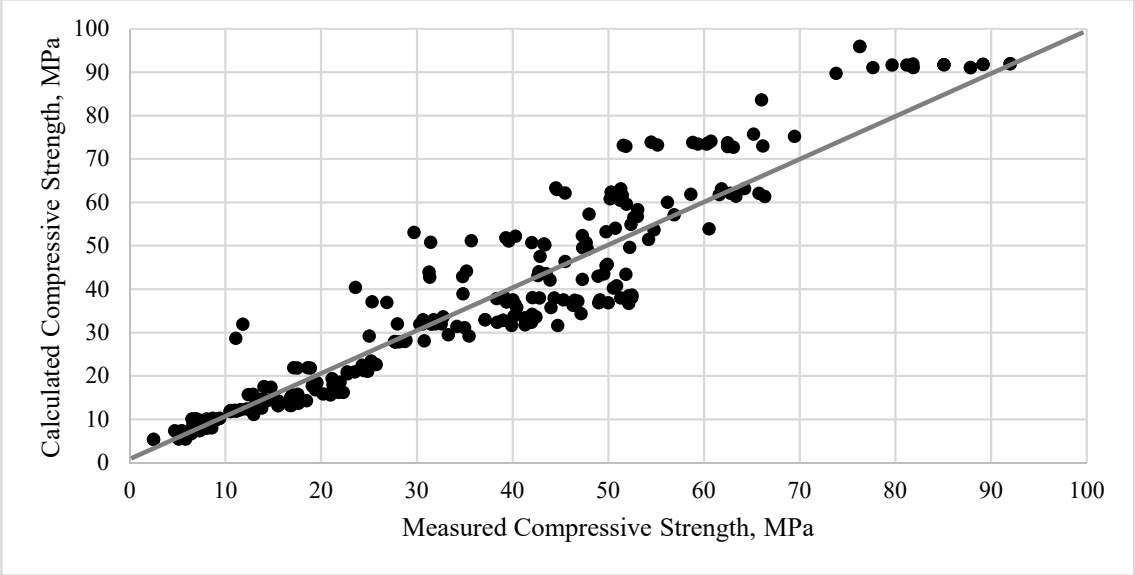

Figure 38 – Error Sensitivity Graph from Equation 4

When splitting the datasets by the main additive, different correlations are obtained, as shown in **Figure 39**. Nevertheless, these correlations have a low coefficient of determination (varying from 0.58 to 0.88) due to lower V_p at similar UCS when samples are cured at higher temperatures, which implies poor estimations when temperature effects are not considered.

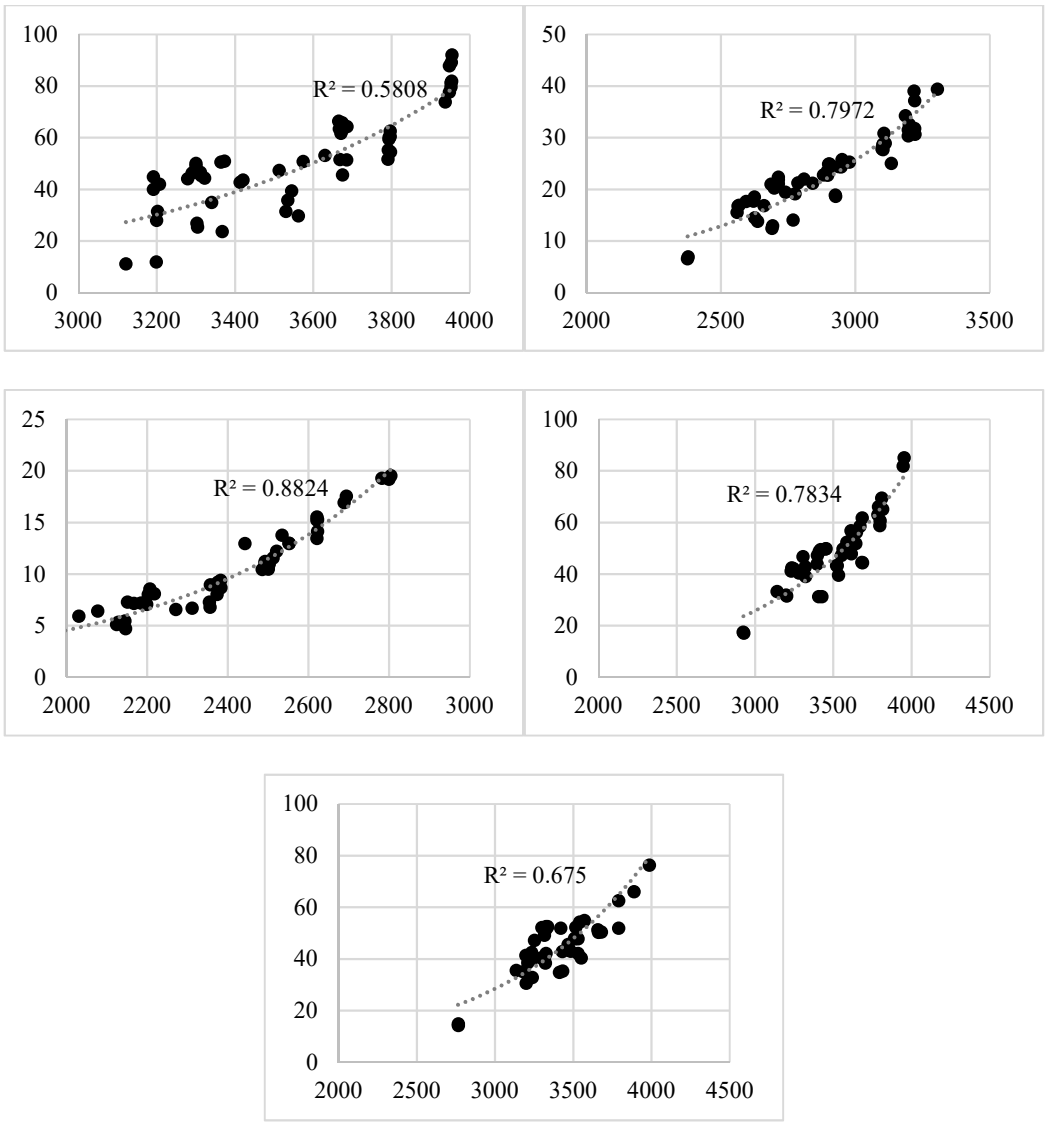

Figure 39 – UCS (y-axis) versus V_p (x-axis). From left to right: CN, CB4 (top), CB10, CS4 (center), CS12 (bottom).

In the following, different correlations between the measured UCS and V_p will be presented based on the additives and the curing temperature of the samples.

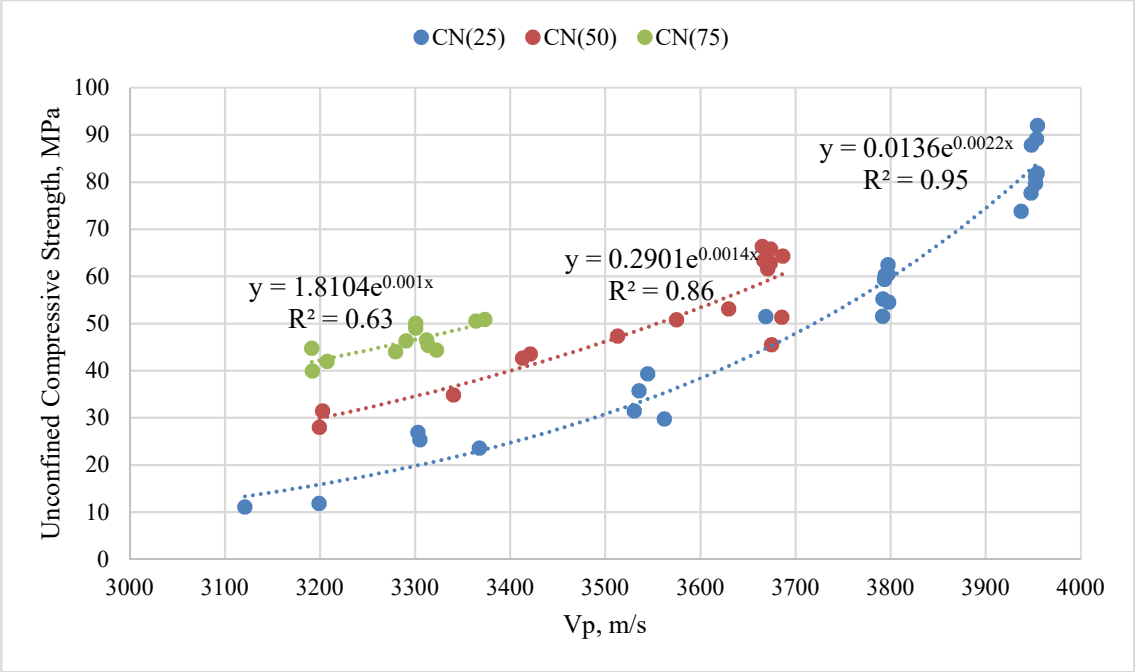

Figure 40 – UCS vs. V_p – Neat Cement – Various Temperatures

We present three different correlations based on temperature for each type of cement used in this research. **Figure 40** shows that at 25°C, the velocity of the principal wave is between 3100 and 3950 m/s, and corresponds to UCS values between 10 and approximately 90 MPa, acquired in approximately 300 days. With higher temperature, the upper limit of V_p becomes smaller (3200 to 3700 m/s for 50°C and 3200 to 3400 m/s for 75°C), Fitting the data points for the 75°C samples through an exponential function does not offer a high coefficient of determination.

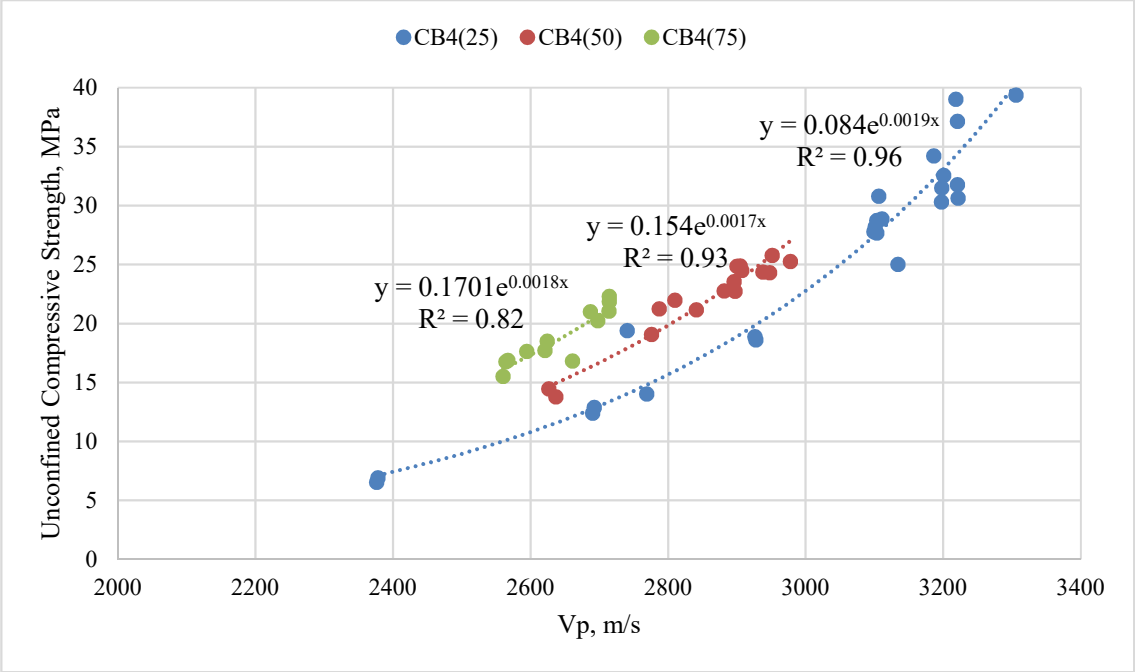

Figure 41 – UCS vs. V_p – 4% Bentonite – Various Temperatures

The above figure presents UCS and V_p measurements for the 4% bentonite cement. Better correlations (when comparing to the neat cement) are observed at all temperatures, with speeds ranging between 2400 and 3300 m/s. At higher temperatures, the lower boundaries increase (approximately 2600 m/s) because of the higher initial UCS.

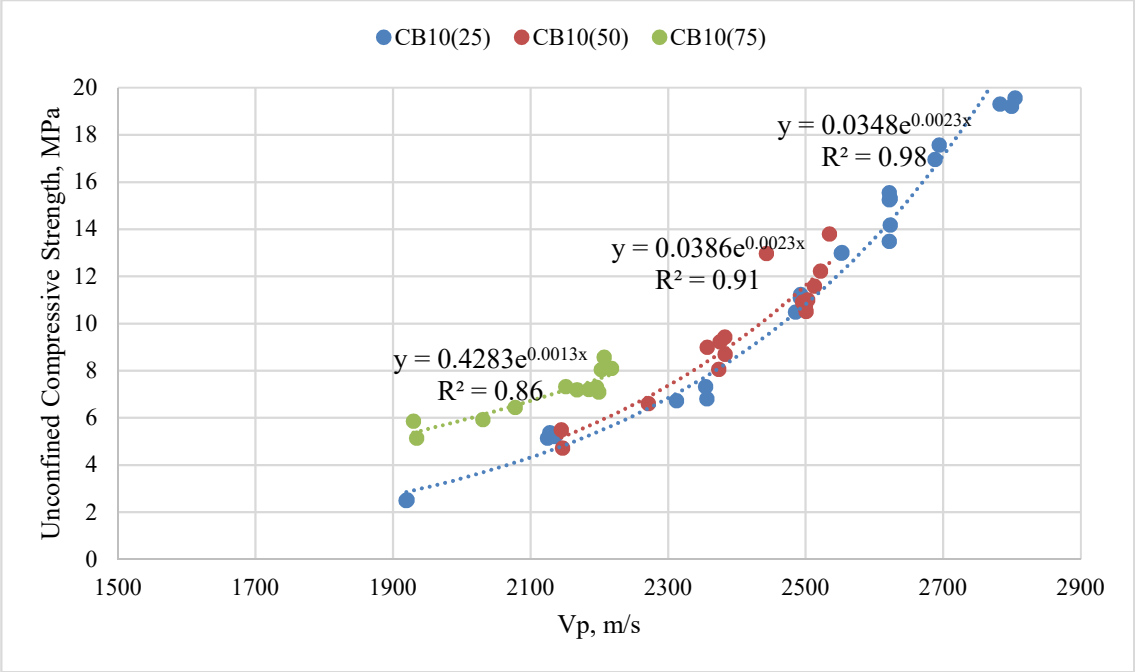

Figure 42 – UCS vs. V_p – 10% Bentonite – Various Temperatures

In the case of cement mixed with 10% bentonite, no large influence on UCS and Vp is observed when curing samples at 50°C, with both the blue and red curve following a similar trend. At 75°C, V_p ranges between 1900 and 2200 m/s and strength ranges between 5 and 8 MPa.

The 4% salt cements (**Figure 43**) exhibit V_p values between 2900 and 3950 m/s and a differentiation between the values acquired at the 3 temperatures. In the case of 4% salt cement cured at 75°C, the correlation between UCS and V_p is almost linear, behavior also observed in the case of 12% salt cement (see **Figure 44**).

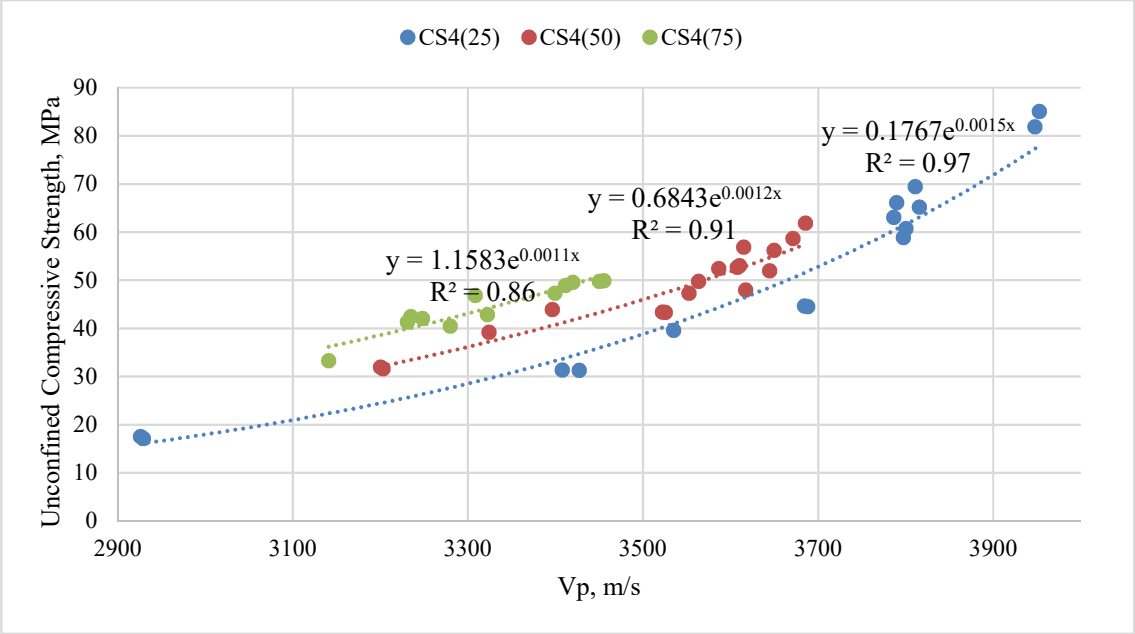

Figure 43 – UCS vs. V_p – 4% Salt – Various Temperatures

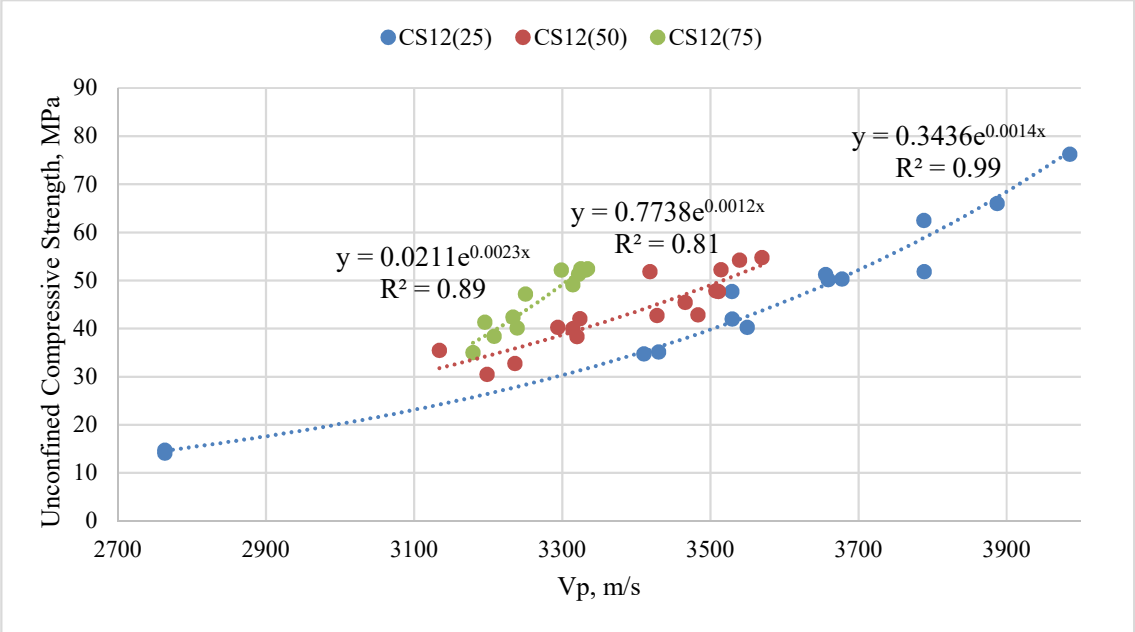

Figure 44 – UCS vs. V_p – 12% Salt – Various Temperatures

As seen in Figures 40 to 44, the exponential fits of UCS increase with V_p can be more accurately fit through temperature-sensitive curves. Appendix D shows calculated versus

measured UCS for all cement recipes cured at 25°C, 50°C, and 75°C and their deviation from the 1:1 lines.

4.3.2. Young's Modulus and Poisson's Ratio

By using the equations C1 to C7 presented in Appendix C and the acquired velocities of the P and S waves, the dynamic Poisson's ratio, shear modulus, and Young's modulus have been estimated. Because the acquired measurements do not present large differences at different times, the following chart presents values averaged over the entire measurement time span for each cement recipe at 50°C and 75°C.

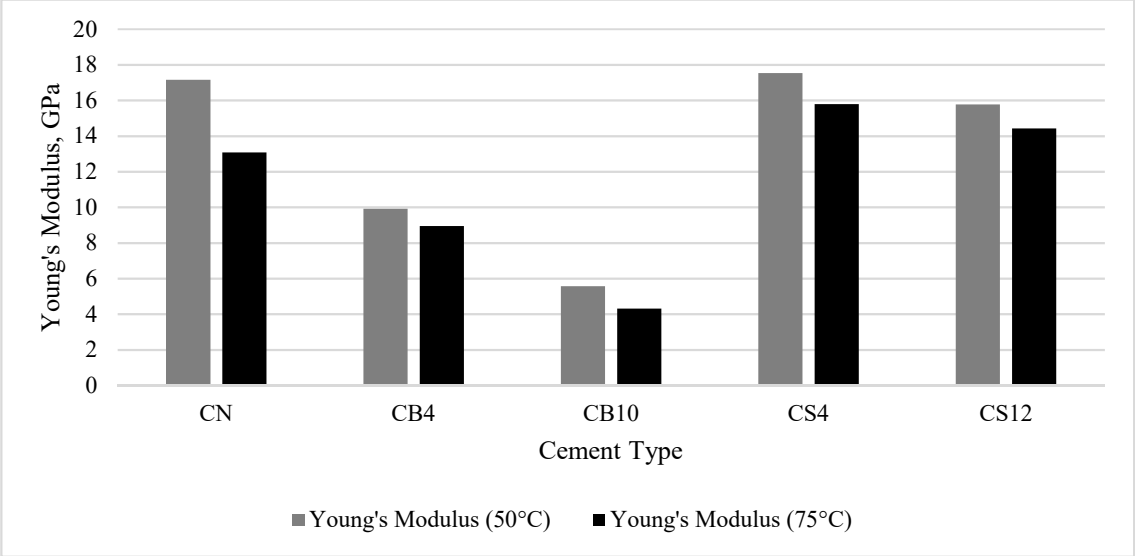

Figure 45 – Average Young's Moduli Comparison

Figure 45 shows comparable results for Young's moduli of neat and salt cements cured at 50°C of 16 to 17 GPa, and lower values for the 4% bentonite cement (10 GPa) and 10% bentonite cement (5.5 GPa). In average, the 25°C temperature increase only decreases the elasticity modulus of the samples by approximately 2 GPa, except for the neat cement formulation, where it decreases by 24%, as compared to approximately 10%

for the salt cements. This implies that the addition of salt reduces the decrease of Young's modulus of Class G cement.

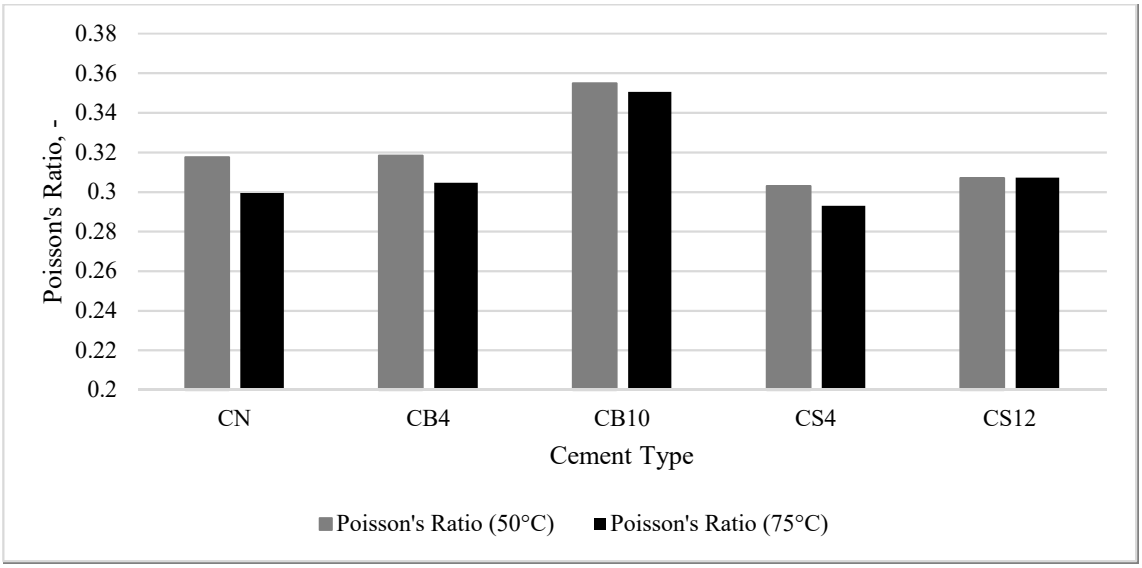

Figure 46 – Average Poisson's Ratio Comparison

As seen in the figure above, the values for Poisson's ratios vary between 0.29 and 0.35 in the five cement recipes cured at 50°C and 75°C. The addition of 4% bentonite does not strongly influence Poisson's ratio, whereas 10% bentonite increases it by approximately 12%. Salt cements show slighter lower values than neat cement, averaging at approximately 0.3.

4.4. T_2 NMR Measurements

Nuclear-magnetic resonance measurements were performed on samples mixed and cured at room temperature under water in an open vial during 2016-2017, and cured at 50°C and 75°C starting May 2017. These samples were mixed with the same slurry. cast as cement cubes for the mechanical and ultrasonic tests.

4.4.1. Error Determination and the Influence of Glass-Cement Contact

Because the NMR samples were cast in a glass vial, the influence and reproducibility of results was assessed by performing measurements using the same parameters on samples of same age cored out of cement cubes from the neat cement slurry, and on samples after removal of the glass vial. Since glass cracking and the development of a water film or water intrusion between the glass and the cement was a bigger concern for samples cured at higher temperatures, these tests were run for samples cured at 50°C and 75°C.

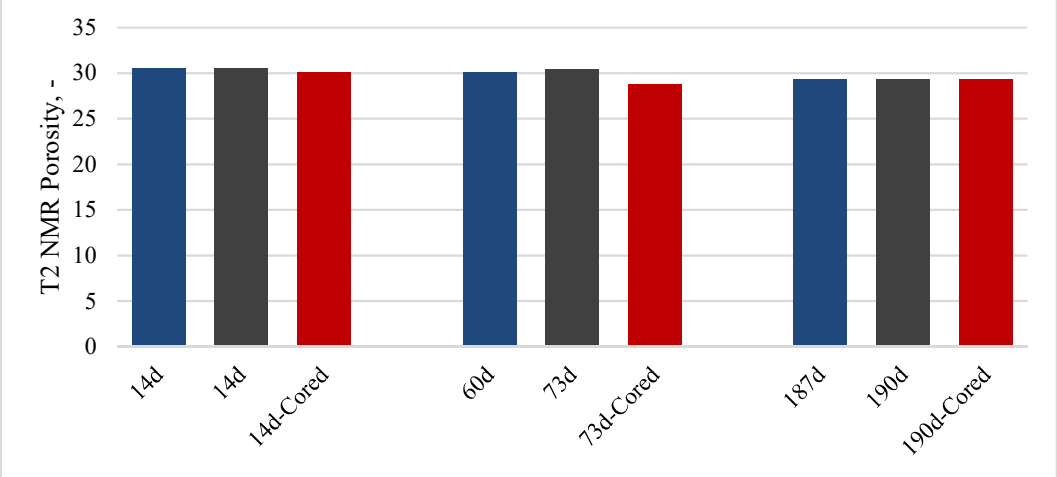

Figure 47 – NMR Results Reproducibility (50°C)

As seen above, the measurements show reproducibility across batches (as represented through blue and gray) at same times, and between samples cured in a vial and cored samples, represented through red bars, with differences between 0.34% and 5.26%).

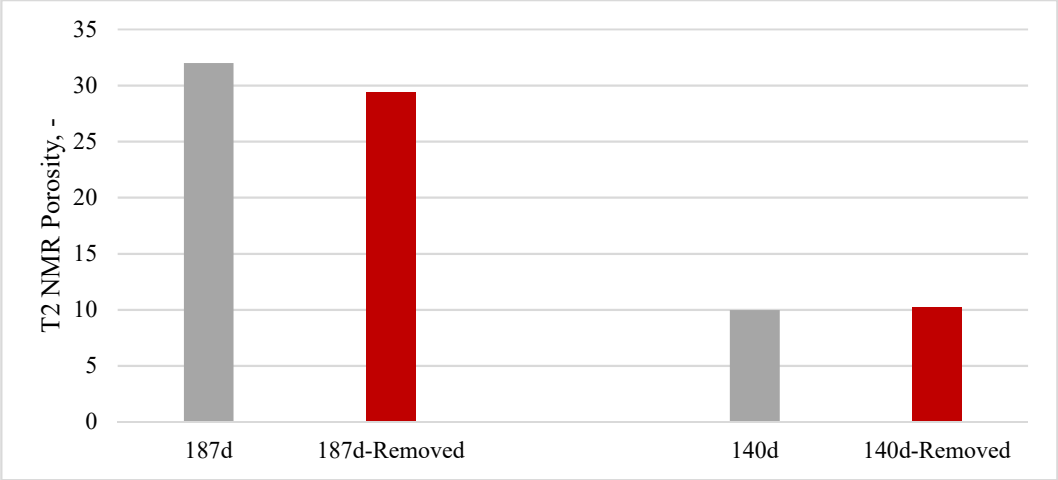

Figure 48 – NMR Results Reproducibility at 50°C and 75°C for Samples in and Removed from Glass Vial

Similar results are displayed before and after the glass vials are removed (**Figure 48**). Nevertheless, a larger deviation is shown in this case (2.9% porosity difference at 187 days, but only 0.2% difference at 140 days), because even though care was taken during glass removal, minor volumes of cement rock may have still been removed together with the glass, leading to a smaller test volume.

4.4.2. NMR Porosity at Time and Temperature

As mentioned in Chapter 4.2.1, at higher temperatures, initial unconfined compressive strength is greater for samples from the same cement slurry. The following graph shows the values of the T_2 NMR Porosity (or water content) in samples at day 1 across the three temperatures.

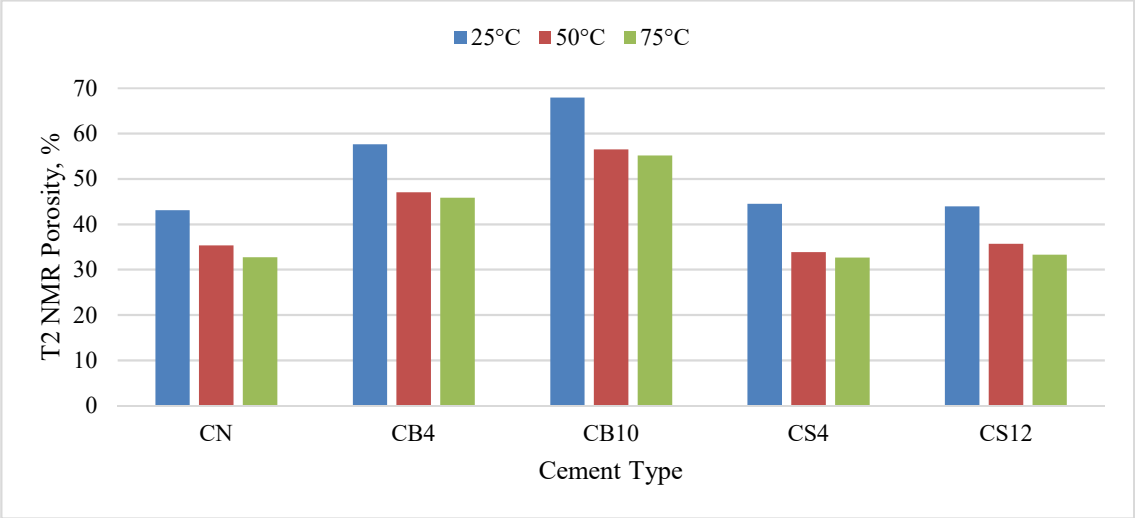

Figure 49 – Day 1 NMR Porosity of Various Samples at 25°C, 50°C, and 75°C

Lower water content is correlated with an increase in temperature, meaning that more water is being consumed in the hydration reaction (which is exothermal and accelerated by the increased temperature) and transformed into chemically bound water. Moreover, the effect of the additional water used when mixing bentonite cements can be observed, CB4 and CB10 displaying initial average porosities of 57% and 68%, respectively. No large difference in porosities is observed between salt cements and cement without additives at day 1.

The principles and parameters of the T_2 NMR measurements made on the cement samples are explained in Appendix E. In what follows, the evolution of T_2 NMR porosity with time and temperature are described.

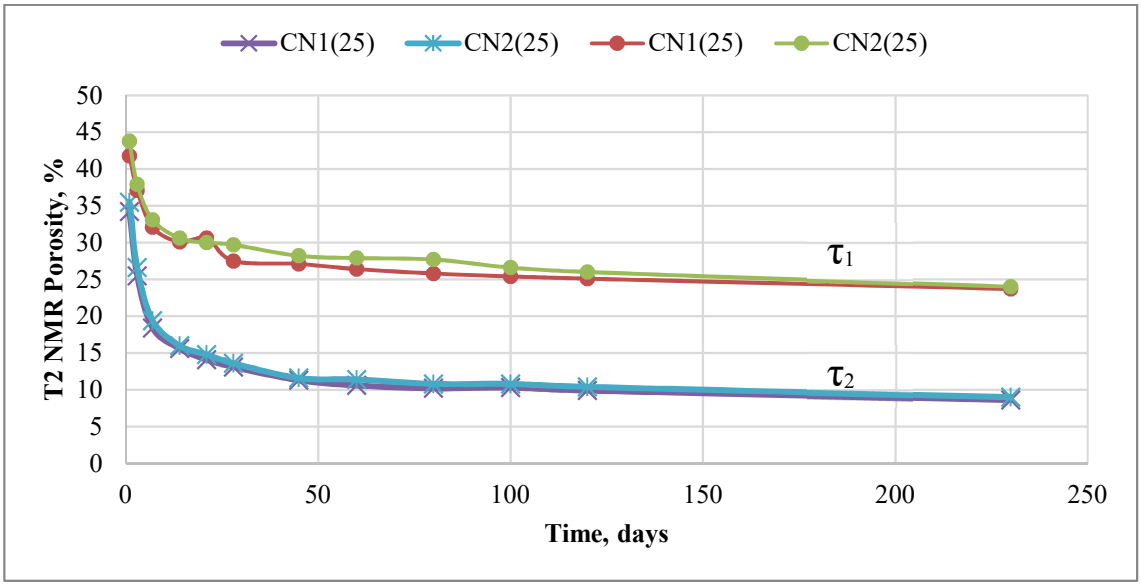

Figure 50 – T_2 NMR Porosity – Neat Cement – 25°C – τ_1=57 µs, τ_2=150 µs

The figure above shows results of the T_2 measurements performed on two different samples and the influence of τ on the results up to 230 days. As mentioned in Chapter 3.3.2, the τ parameter represents the time between the 90° pulse and the first acquired echo. The larger this number is, the lower the resolution of the measurement, so less signal coming from the water trapped inside the sample's pores is acquired. With a large τ, the signal comes from the big pores, whereas a smaller τ value will also capture small pores. On average, there is a difference of 14.5 porosity units between the two measurements. This difference starts smaller (between day 1 and day 14 of measurements) because initially the fluid filled pore sizes of the cement are larger. With increasing hydration, the fluid filled pore sizes get smaller and the water is consumed, so the difference between the two measurements becomes constant. A similar behavior is

observed for the other samples containing salt, which exhibit comparable porosity at 25°C. The samples with bentonite exhibit larger T_2 NMR porosities because of higher w/c, and slightly larger differences between the τ_1 and τ_2 plots, as shown in **Figure 51**.

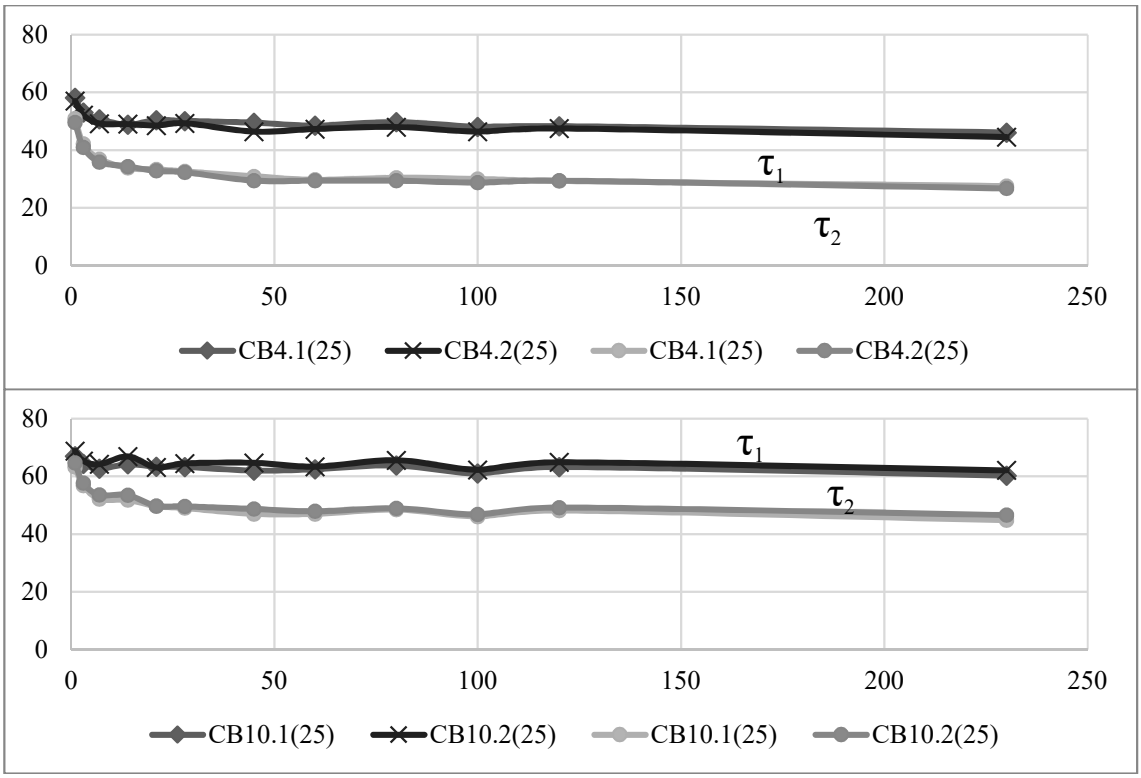

Figure 51 – T_2 NMR Porosity – Bentonite Cement – 25°C – τ1=57 µs, τ2=150 µs

Once again, the reproducibility of the results is confirmed by the overlaying curves with measurements performed on different samples at the same times. Another general trend observed across all samples is the steep decrease in measured porosity until day 28-40, and a slow, linear decrease afterwards, in samples cured at 25°C. In what follows, only measurements performed with τ=57 µs will be presented.

Samples cured at higher temperatures exhibit a different behavior with time. Porosity data over an extended timeframe are shown in **Figure 52** for Neat cement samples (CN) cured at three different temperatures.

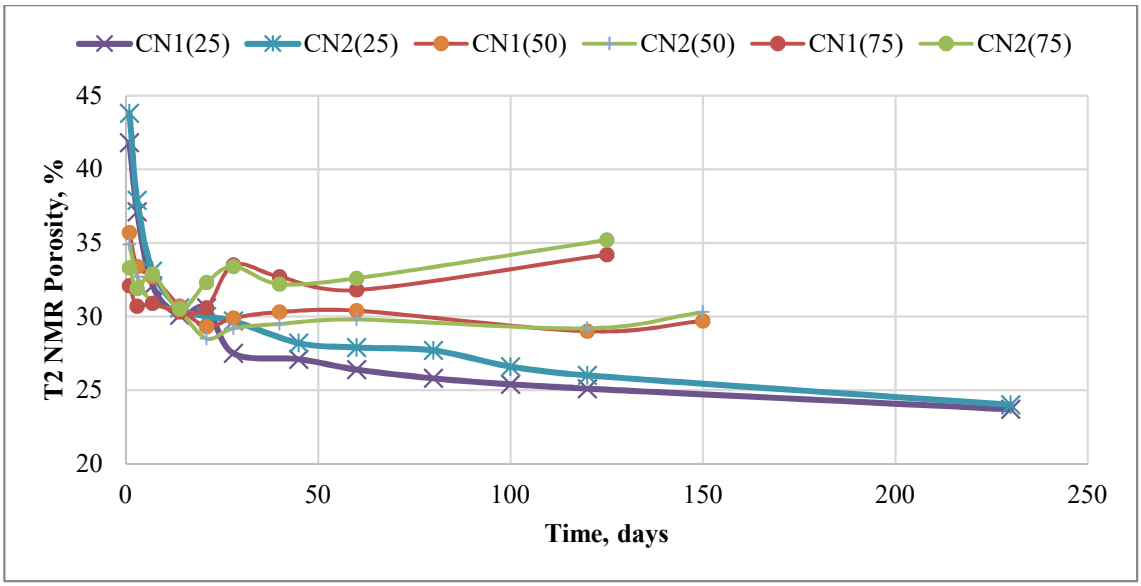

Figure 52 – NMR Porosity Evolution in Neat Cement at 25°C, 50°C, and 75°C

At higher temperatures, the water "seen" through the NMR measurements starts increasing after day 21, measurements showing different final porosities after day 125, the largest T_2 NMR porosity being observed at the highest temperature of 75°C. These effects are observed for all samples and will be discussed in what follows.

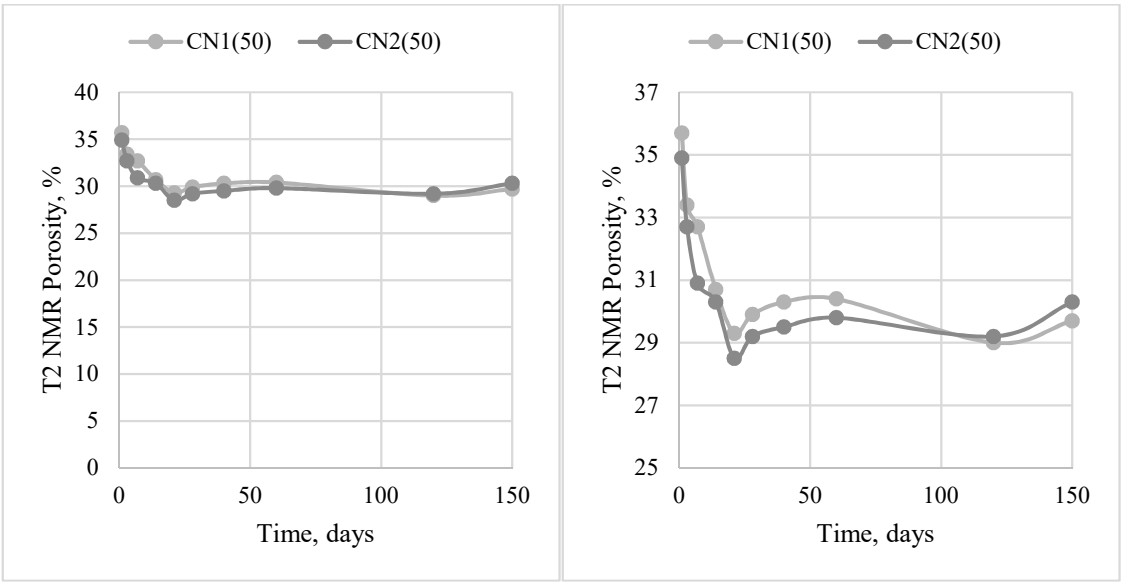

Figure 53 – T_2 NMR Porosity Evolution for Neat Cement (50°C)

At 50°C, porosity decreases until day 21 of measurements for neat Class G cement, after which it slowly increases until day 60, decreasing back to approximately 20% at day 120. This behavior is intensified at a higher temperature, where, starting day 3, the NMR porosity oscillates between 30.3 and 33.4%, increasing to 35.2% at day 120.

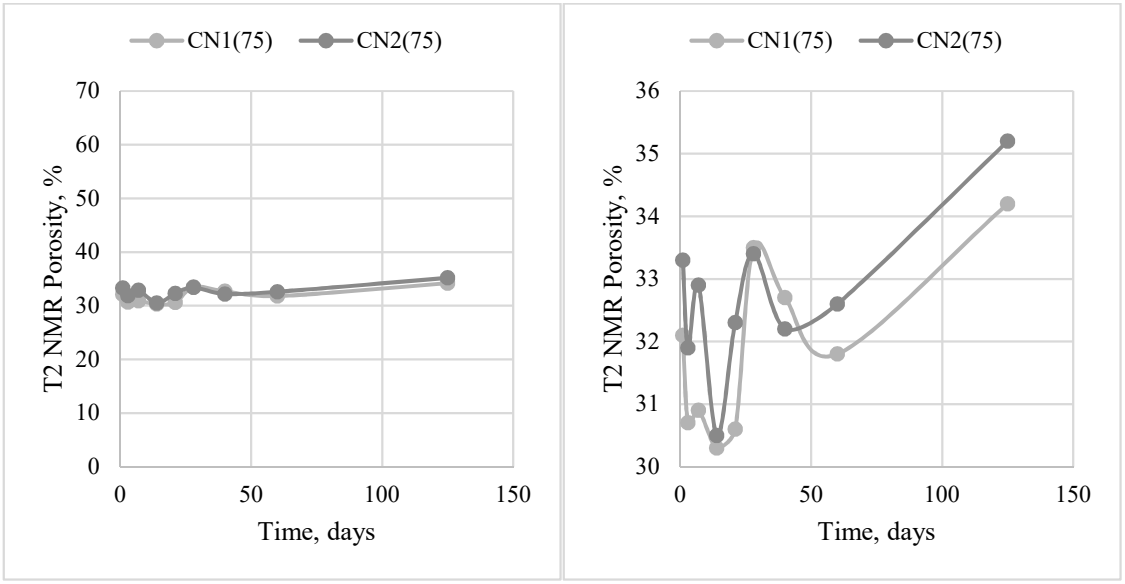

Figure 54 – T_2 NMR Porosity Evolution for Neat Cement (75°C) with Expanded View (Right)

For the 4% bentonite cement cured at 50°C, a slight porosity increase is observed at day 14, followed by a quick decrease, and a steady behavior until day 150, when the T_2 NMR porosity increases.

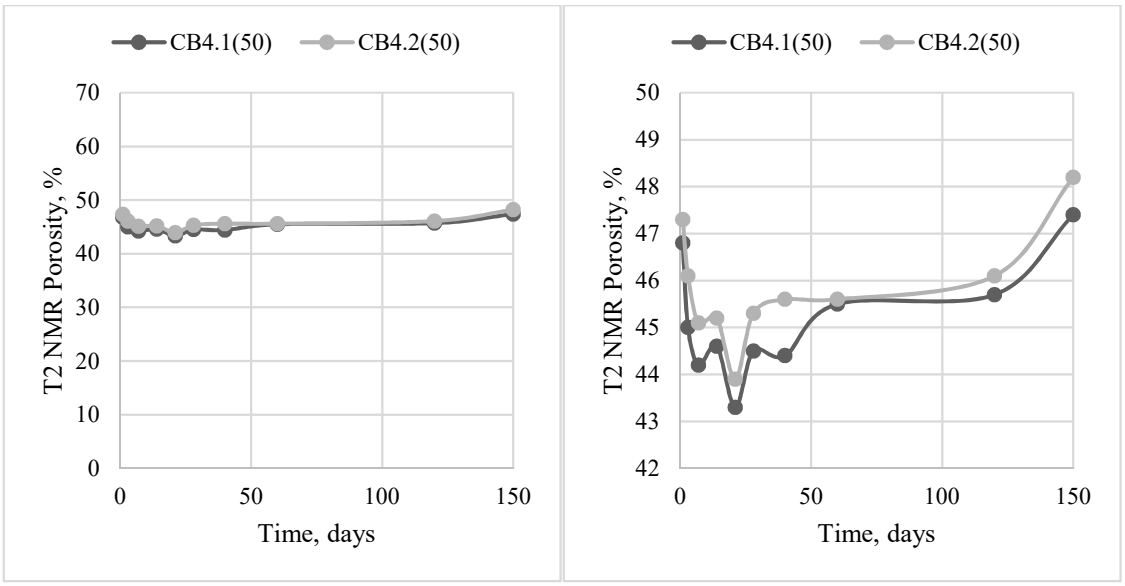

Figure 55 – T_2 NMR Porosity Evolution for 4% Bentonite Cement (50°C) with Expanded View (Right)

At 75°C, the increase in porosity is observed earlier, at 21 days. The measured porosity of the samples oscillates, converging to a value of approximately 47% at day 125.

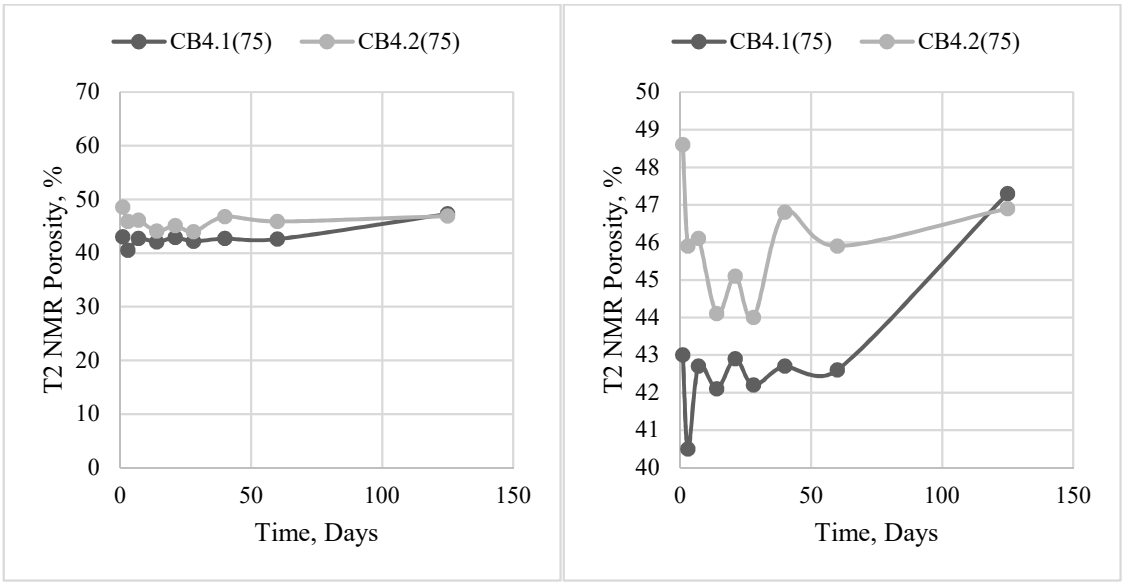

Figure 56 – T_2 NMR Porosity Evolution for 4% Bentonite Cement (75°C) with Expanded View (Right)

The porosity of samples with 10% bentonite cured at 50°C seems to follow a steady increase starting day 7, ending at approximately 61% porosity at day 150.

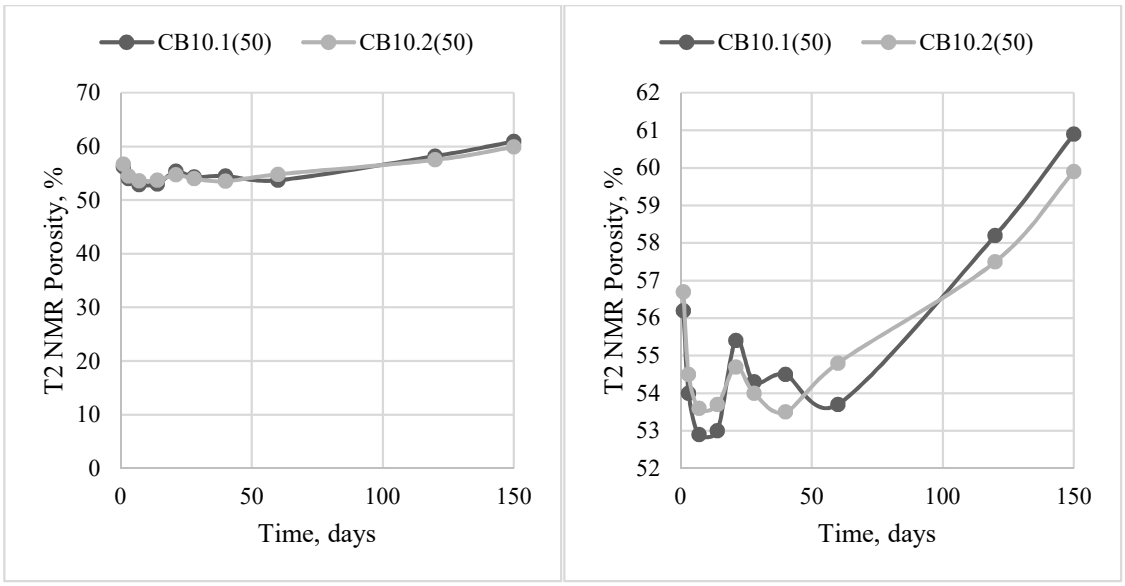

Figure 57 – T_2 NMR Porosity Evolution for 10% Bentonite Cement (50°C) with Expanded View (Right)

At 75°C, the porosity of the same cement recipe shows a similar behavior, with oscillations of ±3% starting day 7 of measurement and an increase ending at day 125.

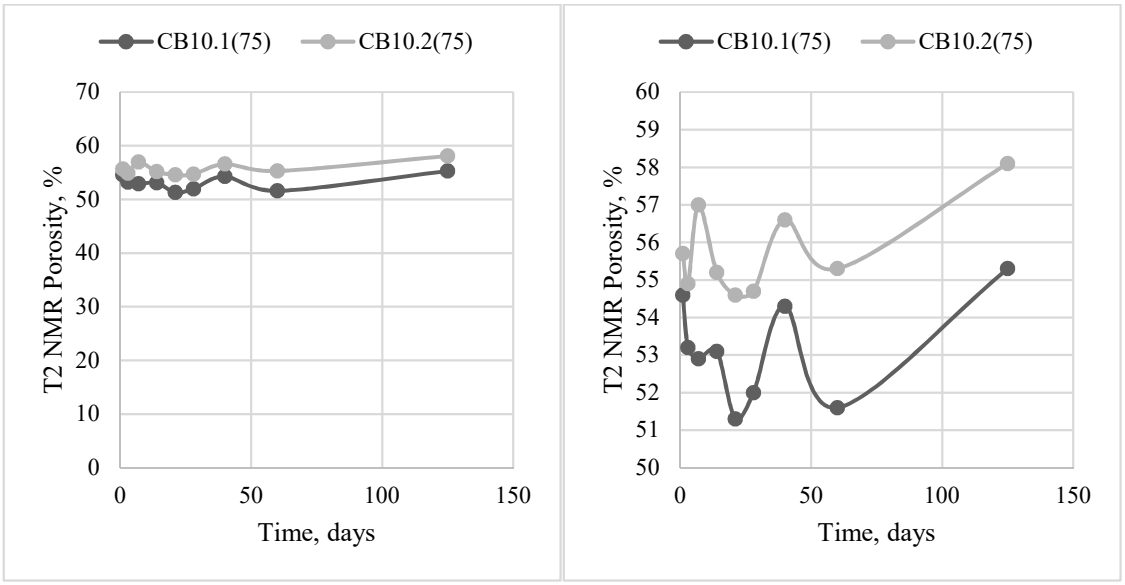

Figure 58 – T_2 NMR Porosity Evolution for 10% Bentonite Cement (75°C) with Expanded View (Right)

Similar developments are observed for the samples containing salt, as shown in **Figures 59** to **62**. As a general trend, the change in T_2 NMR porosity is smoother at 50°C, and oscillates stronger at 75°C, leading to higher values at longer times.

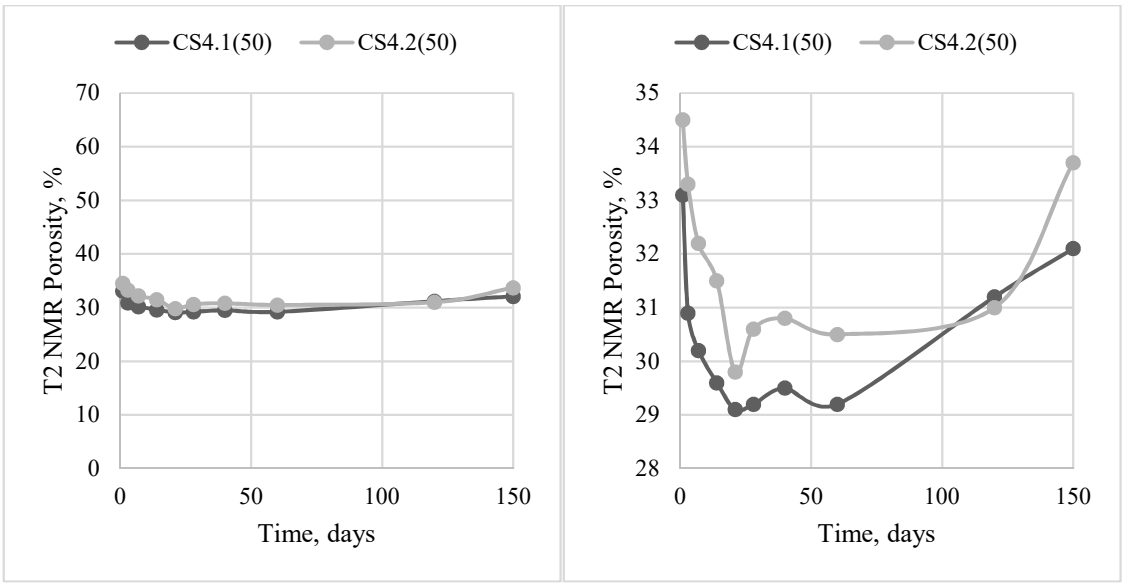

Figure 59 – T_2 NMR Porosity Evolution for 4% Salt Cement (50°C) with Expanded View (Right)

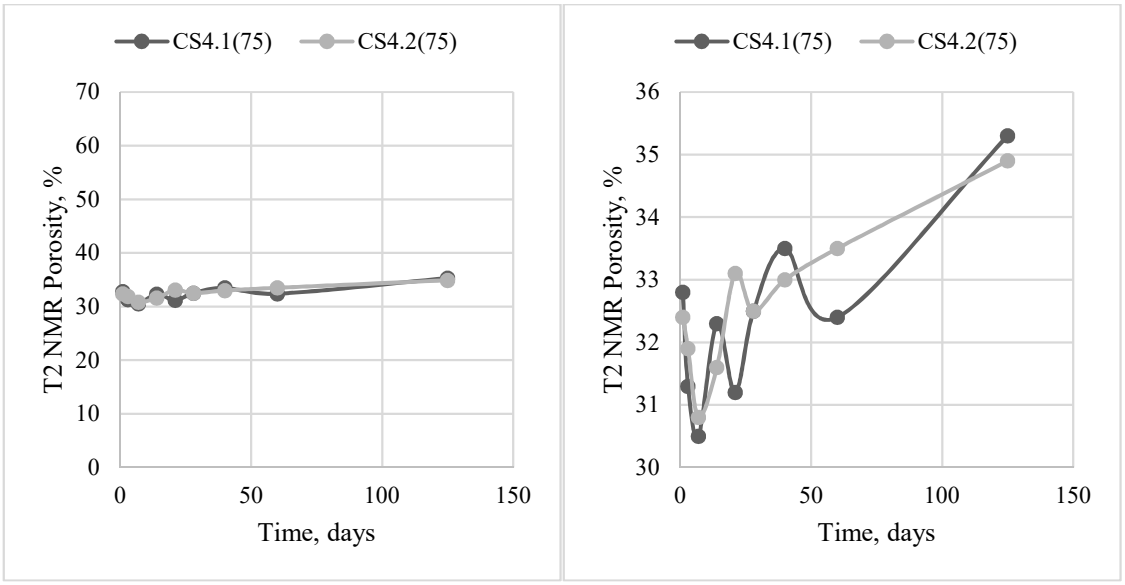

Figure 60 – T_2 NMR Porosity Evolution for 4% Salt Cement (75°C) with Expanded View (Right)

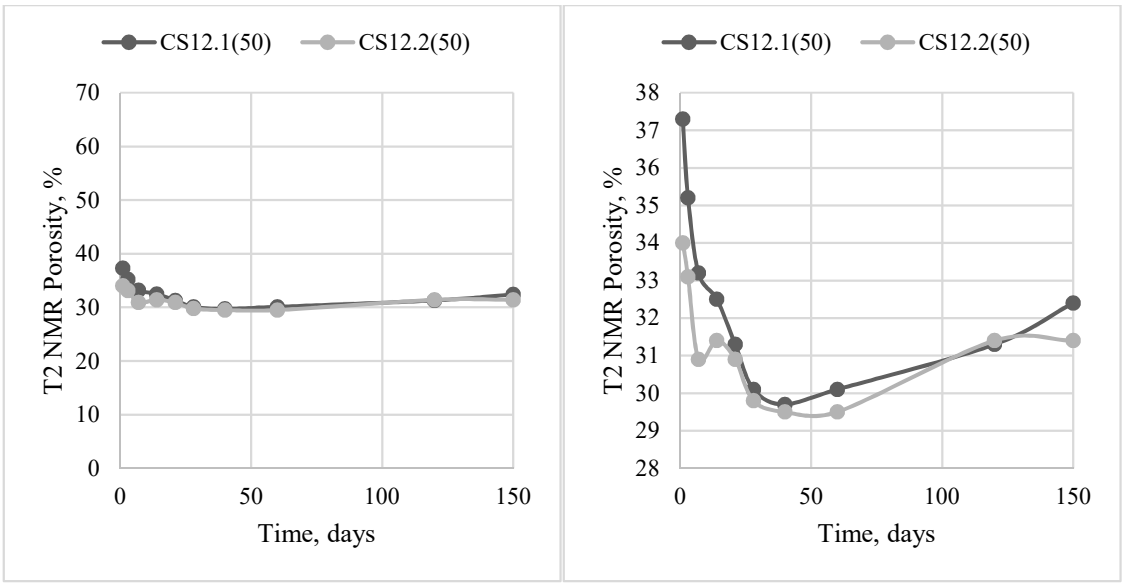

Figure 61 – T_2 NMR Porosity Evolution for 12% Salt Cement (50°C) with Expanded View (Right)

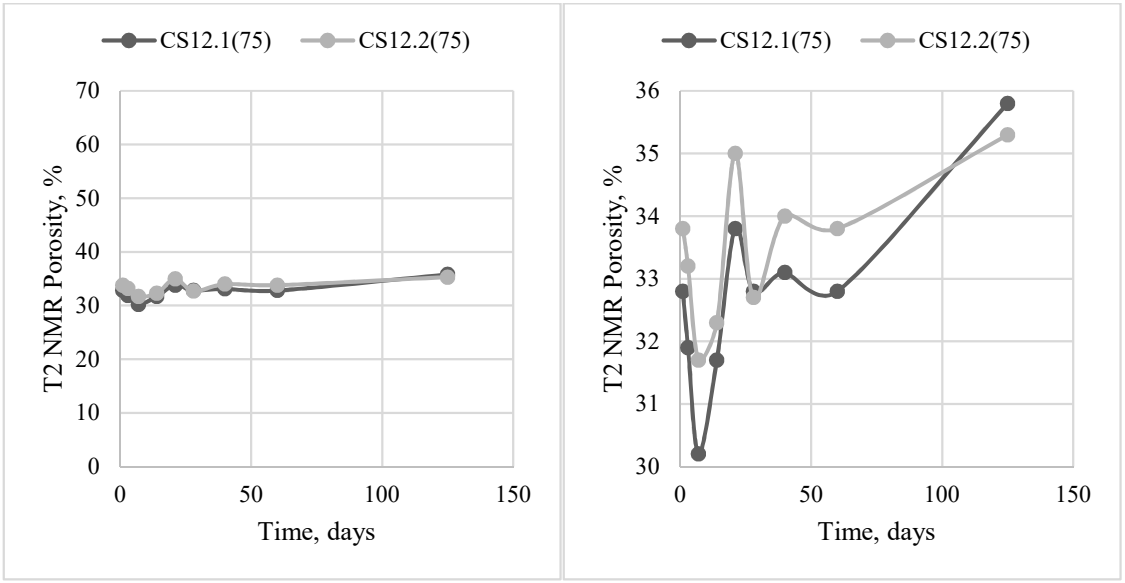

Figure 62 – T_2 NMR Porosity Evolution for 12% Salt Cement (75°C) with Expanded View (Right)

A varying porosity is different than the expected decrease of cement porosity with time, which is related to the water content in the sample. Since the water content is a function of the hydration time and should decrease with hydration progression during sample curing, another mechanism must be responsible for the water producing an increase in

the acquired NMR signal and subsequent porosity values. At 25°C, the water content in all samples follows an expected decreasing trend, as shown in Figures 50 and 51 (for Neat and Bentonite Cements), and in the following figure for salt cements (4% and 12% salt bwow).

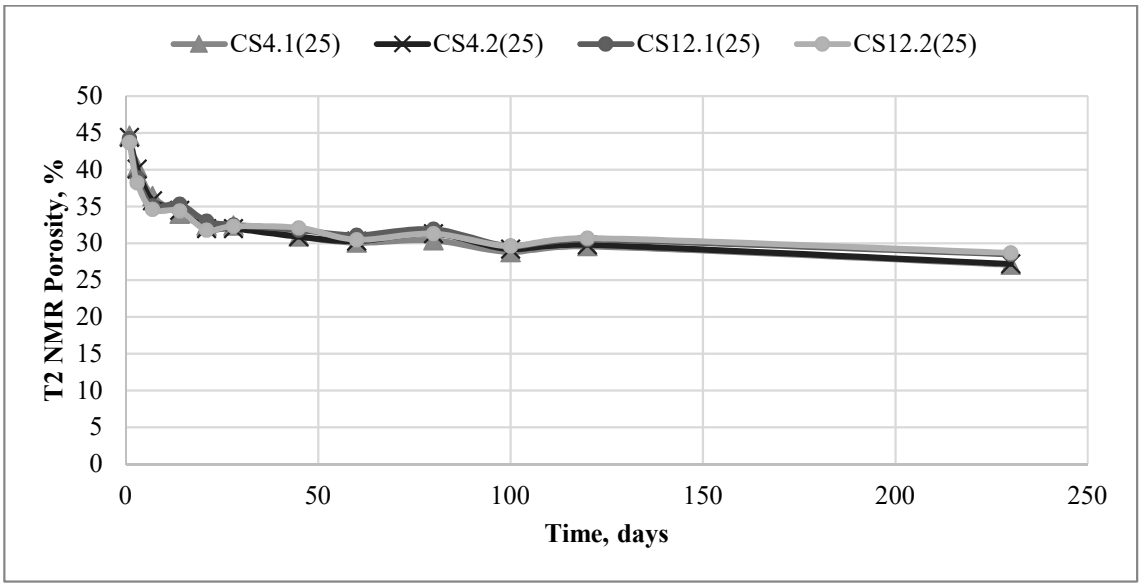

Figure 63 – T_2 NMR Porosity Evolution for 4% and 12% Salt Cement (25°C)

Since the samples were cured in open vials, water may have invaded empty pores from the top of the sample, as presented in Figure 8, Chapter 2.2. The invasion of external water and subsequent increase in T_2 NMR fluid volume might explain the increasing porosity with time, and its oscillation could be explained by the fact that this additional water might engage in further hydration reactions with anhydrous cement. This effect is stronger at higher temperatures, where reaction rate is accelerated, and is in line with observations made by Valori et al. (2013), who mentions that desiccation might decrease the observed water content, and that full capillary pores can be achieved by curing small samples under water (see Section 3.3.3.).

4.4.3. NMR T_2 Distribution Profiles at Time

The data presented in the previous section is the area below the curve obtained when plotting water volume at different relaxation times, which is then divided by the sample bulk volume to be converted into sample porosity (see Appendix E for more information). A few points can be made regarding the pore sizes of the presented cement recipes at different times and temperatures. Because surface relaxivity dominates, these NMR spectra can be analyzed to evaluate where the water is contained at various times during the hydration process, and during the observed water invasion. With average relaxivity values, T_2 times can be converted to effective radii, where short times relate to small radii and large times mean large radii of the pores (see Equation E3).

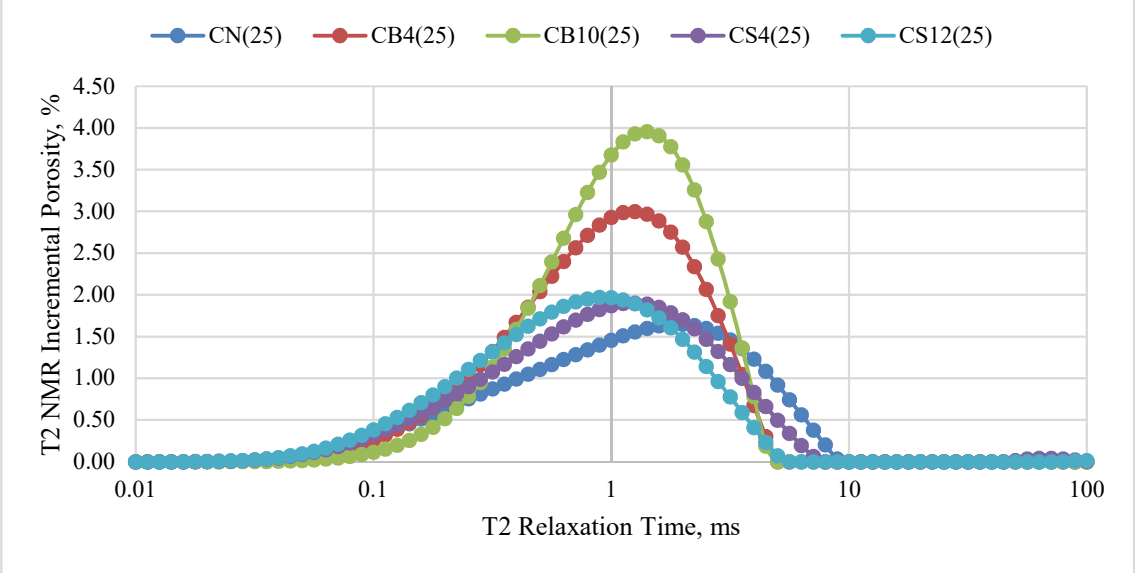

Figure 64 – T_2 Relaxation Time Distributions for All Recipes at 25°C – Day 1

For instance, **Figure 64** above shows that at the first day of measurement, the water in samples kept at 25°C is mostly in pores of the same size for the neat and salt cement recipes, and in larger sized pores in the 4% and 10% bentonite recipes, where the curve

shifts slightly to the right, larger pores. The higher peaks of the bentonite curves also correspond to the higher initial water content in the samples.

When comparing the spectra of similar samples cured at various temperatures for the same time duration, the effect of temperature on the hydration reaction can be observed, as shown in **Figure 65**. At 50°C and 75°C, the curves observed in the room temperature curing scenario shifts to the left, meaning that most of the pore population became smaller, but there is a second peak observed between 10 and 100 ms, suggesting that during the accelerated hydration reaction, some water got trapped in larger pores which may be an effect of the temperature, or mixing inhomogeneity.

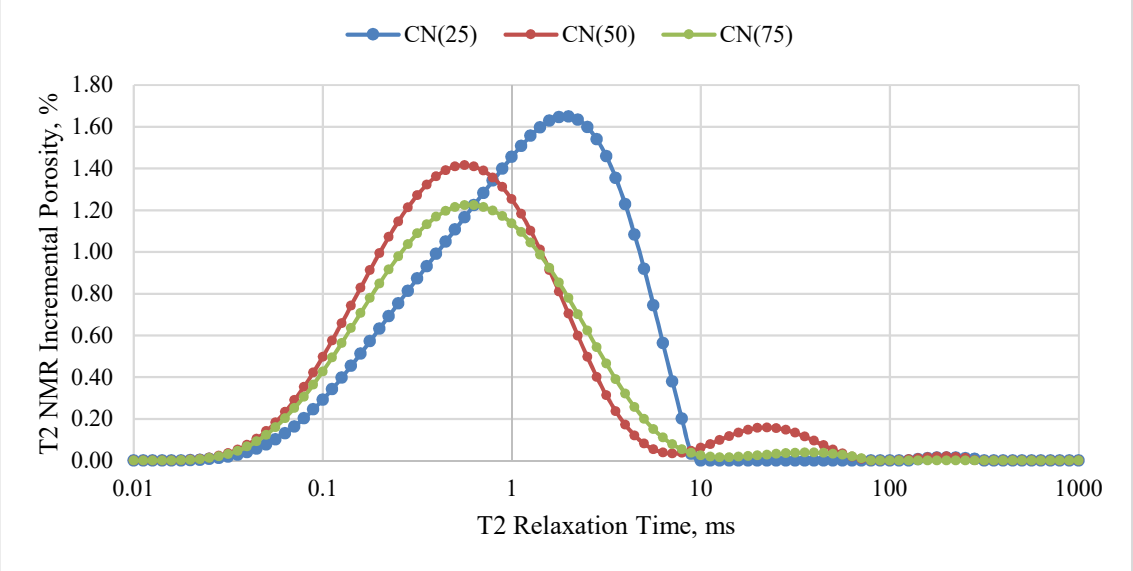

Figure 65 – T_2 Distribution for Neat Cement at Day 1

In the case of cement mixed with bentonite, only a slight increase of the signal is observed in those ranges (see **Figure 66**). Nevertheless, the decrease in T_2 NMR porosity and the curve becoming flatter of the curve is a behavior consistent throughout the samples.

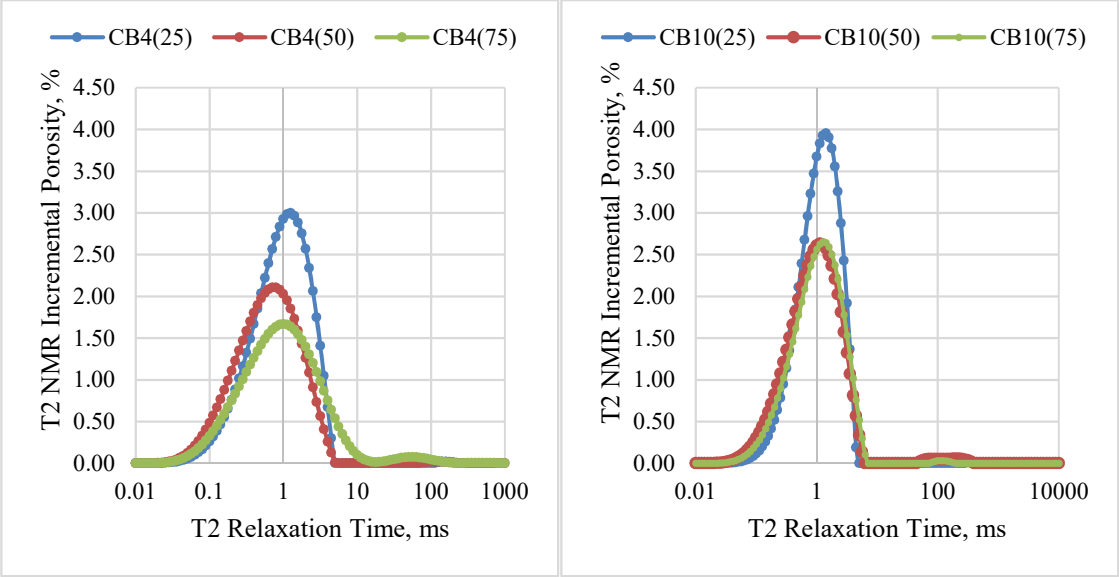

Figure 66 – 4% (Left) and 10% (Right) Bentonite Cement T_2 Distributions at Day 1

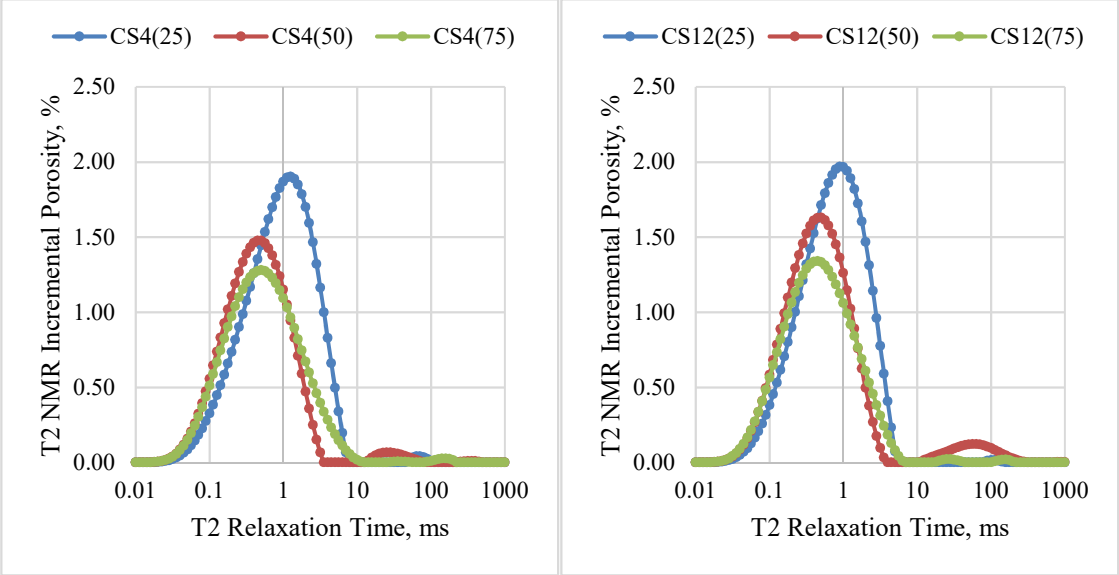

Figure 67 – 4% (Left) and 12% (Right) Salt Cement T_2 Distributions at Day 1

It is possible to follow the evolution of the pore size distribution in a sample for extended times and at different temperatures, as exemplified in the following graph, which shows how at 25°C, the changes in T_2 distribution appear to stabilize after day 60.

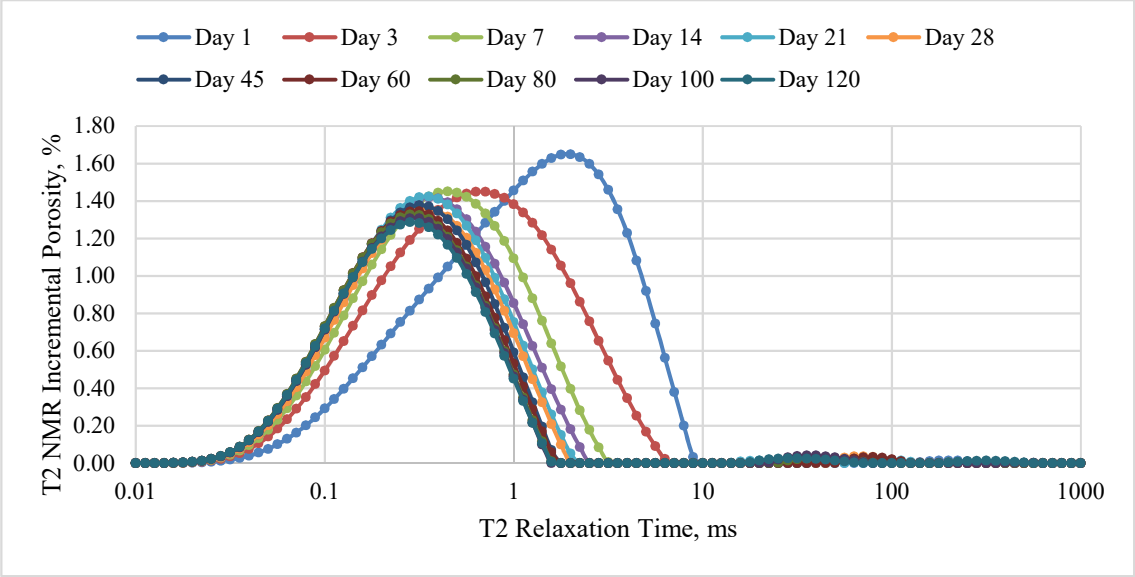

Figure 68 – T_2 Distribution in Neat Cement until Day 120

Since the pore size evolution at 25°C seems to be predictable through a logarithmical decline curve (see Figures 50, 51, and 63), the T_2 relaxation time distribution at 50°C and 75°C will be discussed next, especially at time intervals where unexpected increases in the T_2 NMR water content are observed.

For example, in the neat cement samples cured at 50°C (**Figure 69**), porosity decreases from 30.3% (day 14) to 28.5% (day 21). By analyzing the spectrum of T_2 relaxation times, we observe how at both days 21 and 28, most of the water relaxes at T_2 between 0.1 and 10 ms. However, the day 21 curve (blue), has a lower peak than the curve acquired at day 14. Moreover, a look at the spectral behavior between 1 and 1000 ms shows how the water moves into smaller pores between days 14 and 21, and how additional water is observed moving into the sample at day 28, when the porosity increases by 0.7% to 29.2%.

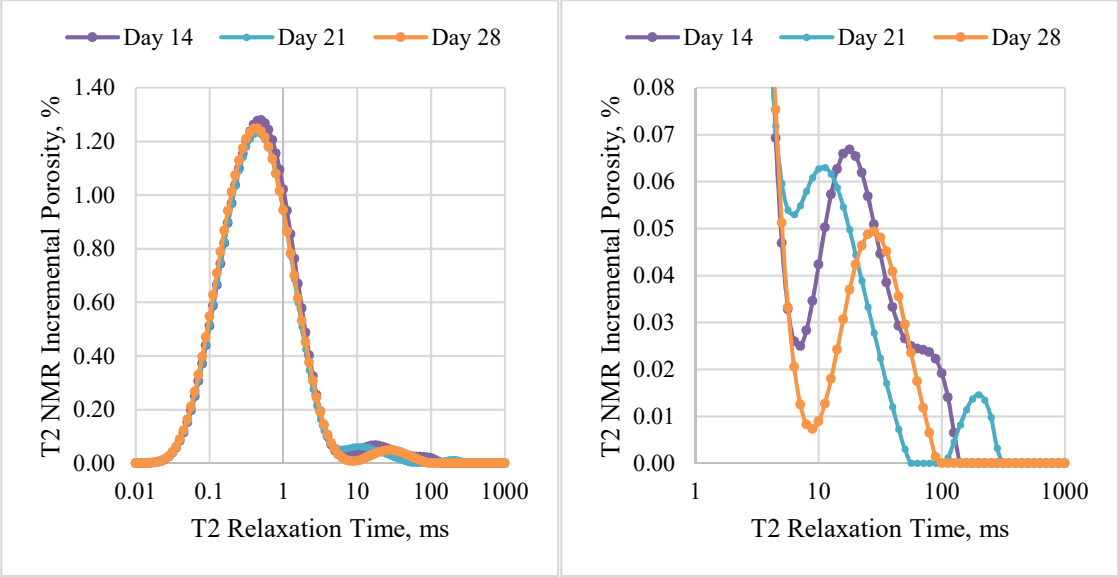

Figure 69 - T_2 Distribution - Neat Cement - 50°C – Days 14, 21, and 28 with Expanded View (right)

The increase in porosity may imply that water invaded the sample from the exterior while other water moved into smaller pores, or engaged in reactions with potential anhydrous cement. As observed, these behaviors are amplified at higher temperatures, where porosity values appear to oscillate with time. Nevertheless, these small changes might be associated with noisy data or mathematical errors stemming from solving the exponentials presented in Equation 3 and will not be presented further in this work.

4.4.4. NMR T_2 Peaks at Time and Temperature versus UCS

The T_2 peaks seem more stable than the distribution of T_2 relaxation times throughout time and may offer a better understanding of hydration dynamics. Like in the porosity measurements, reproducibility across samples is observed in T_2 peaks as well, and a lower resolution is observed for measurements performed with a $\tau = 150$ ms, so that the T_2 peaks are larger (green and red curves **in Figure 70**).

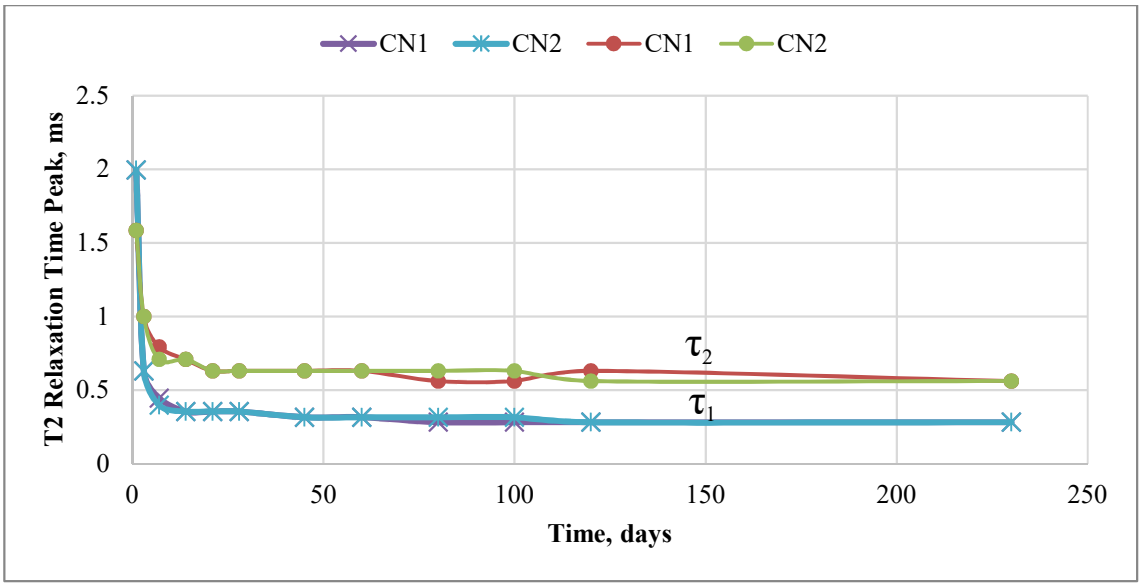

Figure 70 – Observed T_2 Peaks at τ_1=57 ms and τ_2=150 ms

At higher temperatures, the T_2 evolution with curing time, with T_2 peaks being larger at 50°C, and starting to increase after day 3 at 75°C.

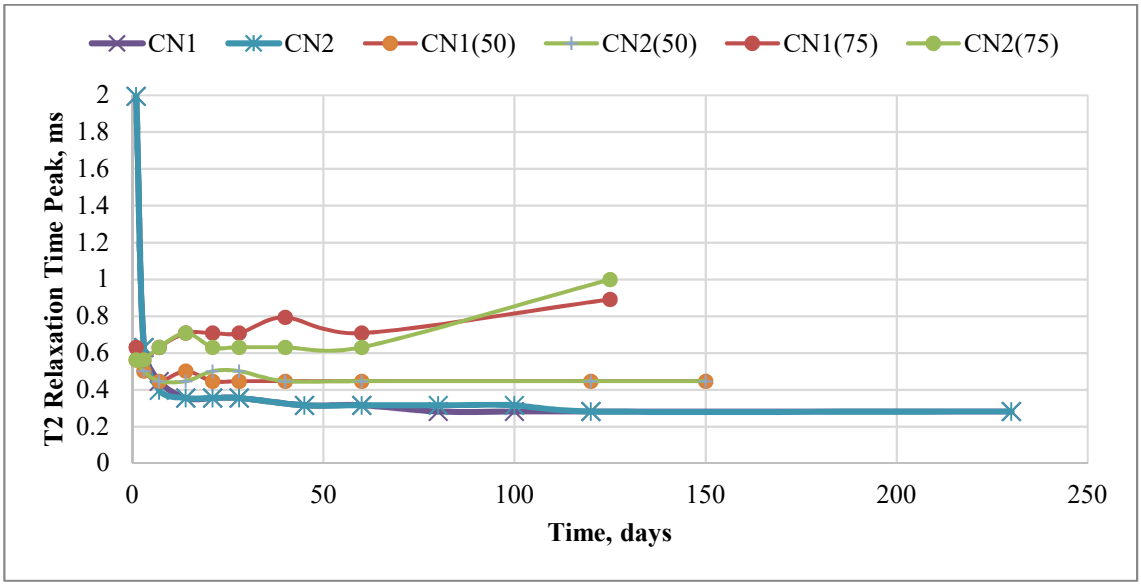

Figure 71 – T_2 Peaks Evolution with Time and Temperature – Neat Cement

A similar evolution is observed in samples containing bentonite (4% and 10%), which exhibit peaks at longer relaxation times, meaning that most of the pores in these samples are larger than in neat cement (see figure below).

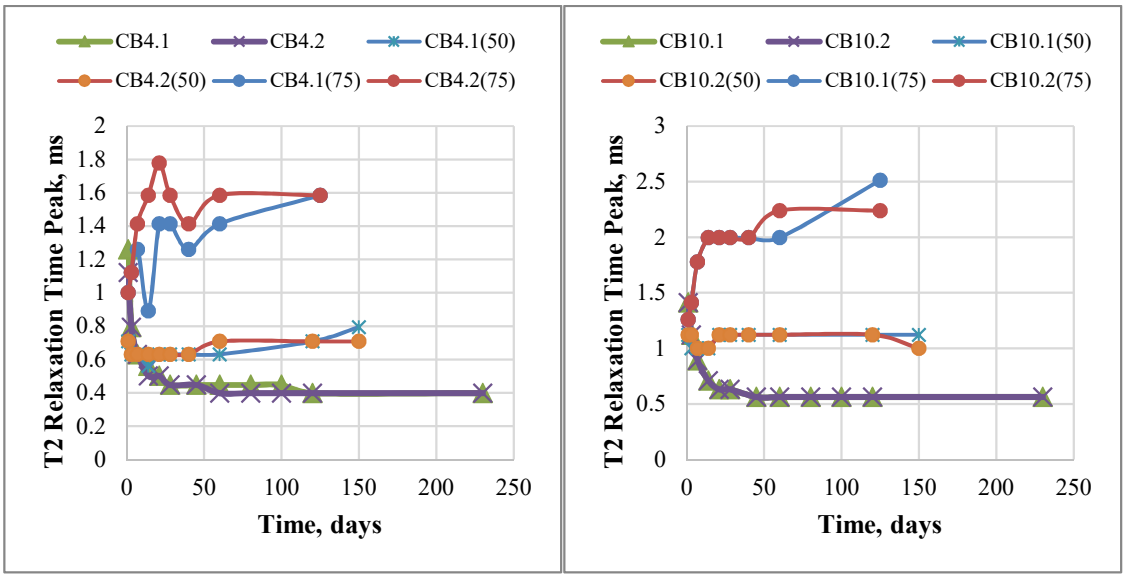

Figure 72 – T_2 Peaks Evolution with Time and Temperature – Bentonite Cement

Salt cements also exhibit an increase in T_2 peak relaxation times, and their values are comparable to the ones observed in neat cements at different temperatures.

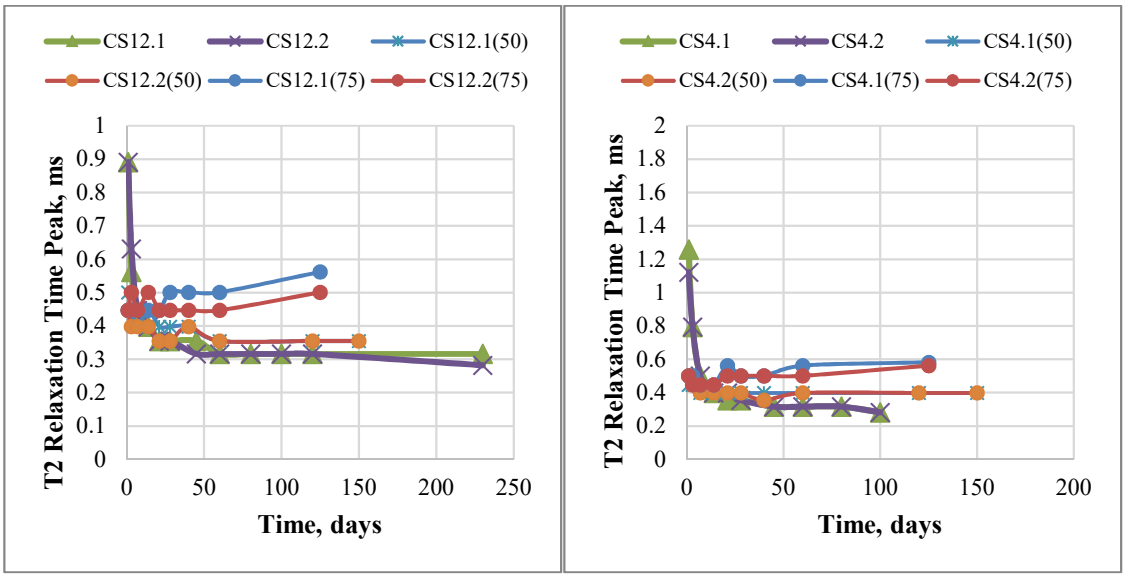

Figure 73 – T_2 Peaks Evolution with Time and Temperature – Salt Cement

Since the T_2 peak relaxation time is related to pore size, which in turn relates to how advanced the degree of hydration in a cement sample is, one can use the T_2 peak evolution with time to assess when a cement develops strength, and, through previous correlation, how much the strength developed. This is presented in **Figure 74**, which shows how smaller T_2 peak relaxation values lead to higher compressive strengths with time.

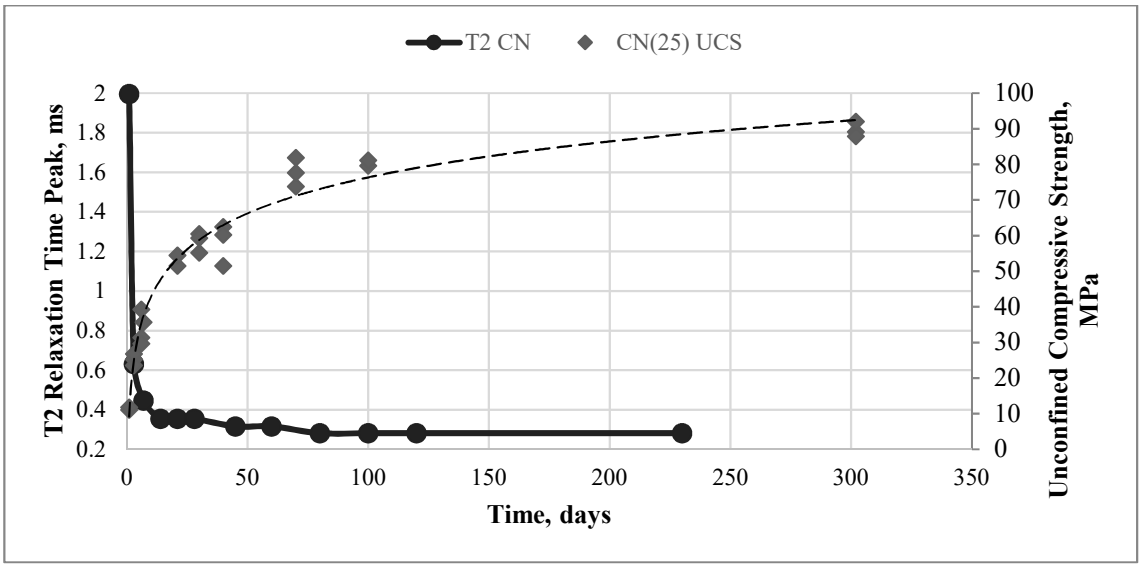

Figure 74 – Neat Cement T_2 Peaks and UCS Evolution with Time (25°C)

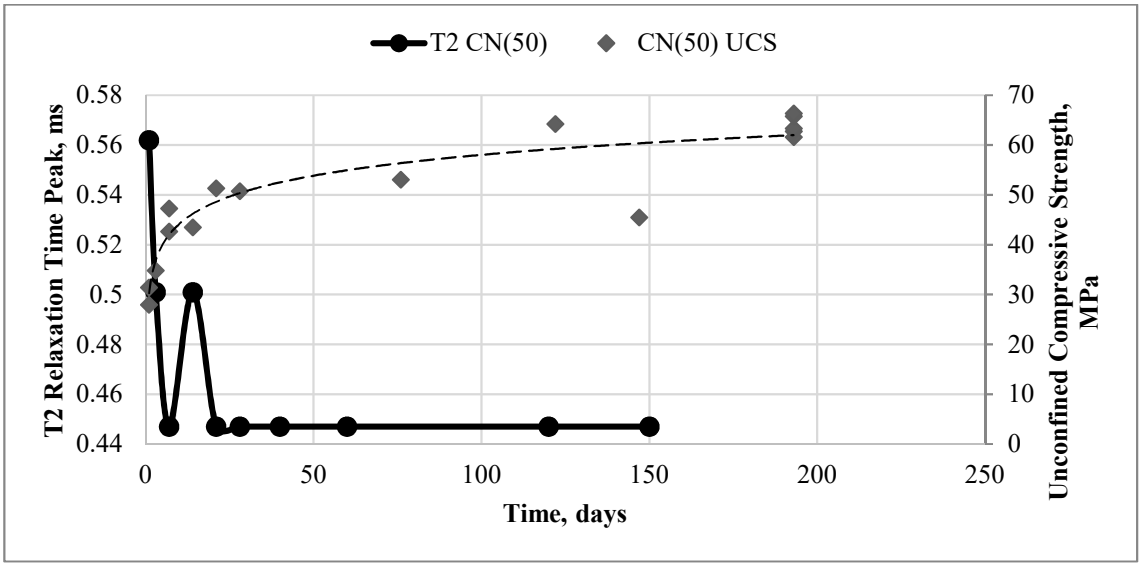

Figure 75 – Neat Cement T_2 Peaks and UCS Evolution with Time (50°C)

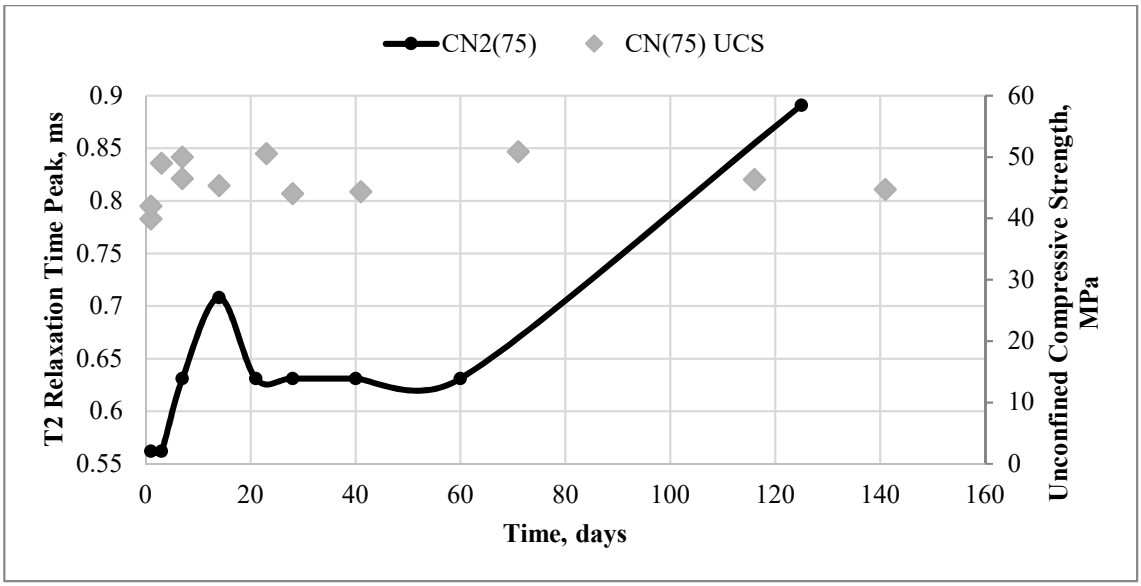

Figure 76 – Neat Cement T_2 Peaks and UCS Evolution with Time (75°C)

At higher temperatures, the T_2 peak relaxation does not decrease like in the 25°C scenario, as also shown in the previous section. In some cases, this may correlate with a loss in strength. However, no evidence shows that the observed pore population decreases strength. The change in these peak positions might arise from the experimental procedure, and may be a result of the sample removal from hot water baths and allowing it to cool to the temperature at which the NMR measurement is done (35°C). As observed in previous experiments done in the Integrated Core Characterization Center at University of Oklahoma, potential temperature gradients of the sample lead to erroneous measurements.

It is shown in **Figures 74, 77, 79, 81**, and **83**, how at 25°C, T_2 measurements can be correlated to UCS values. The other plots of T_2 peaks versus UCS of bentonite cements at higher temperatures are shown as comparison.

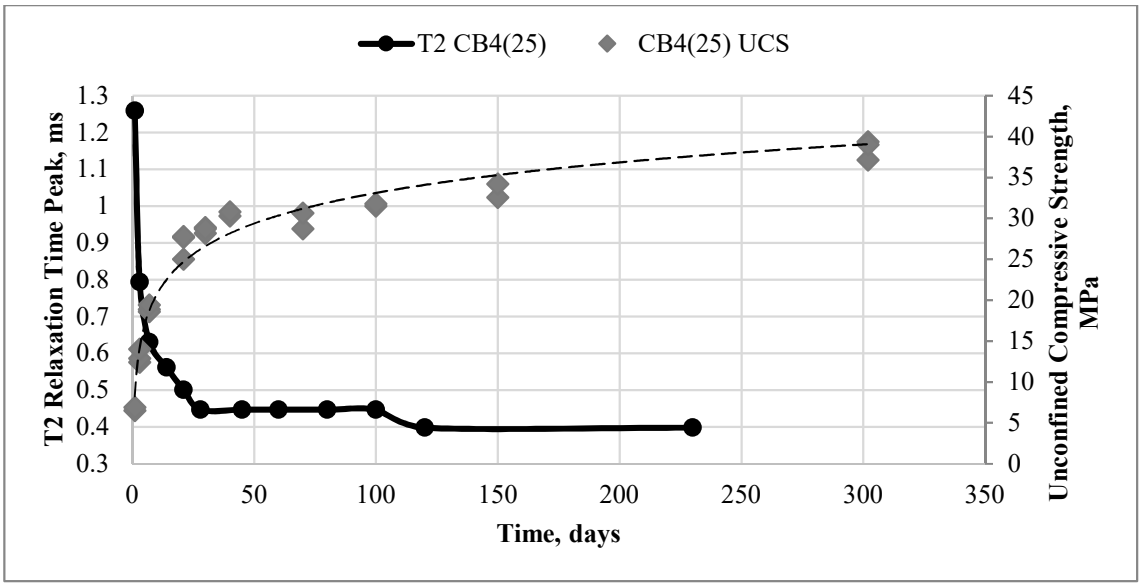

Figure 77 – 4% Bentonite Cement T_2 Peaks and UCS Evolution with Time (25°C)

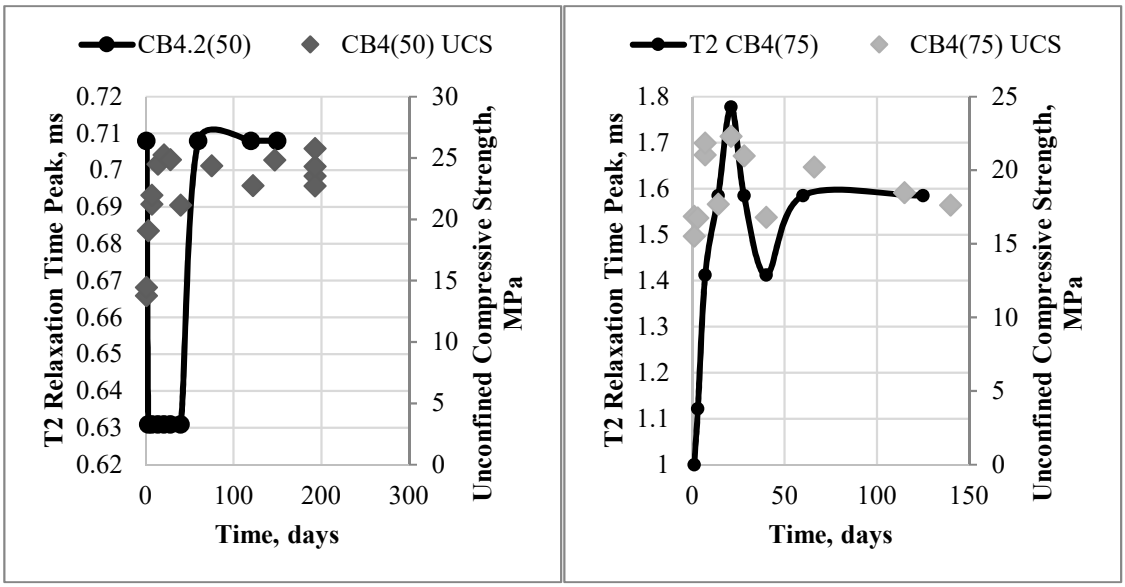

Figure 78 - 4% Bentonite Cement T_2 Peaks and UCS Evolution with Time (50°C – left and 75°C - right)

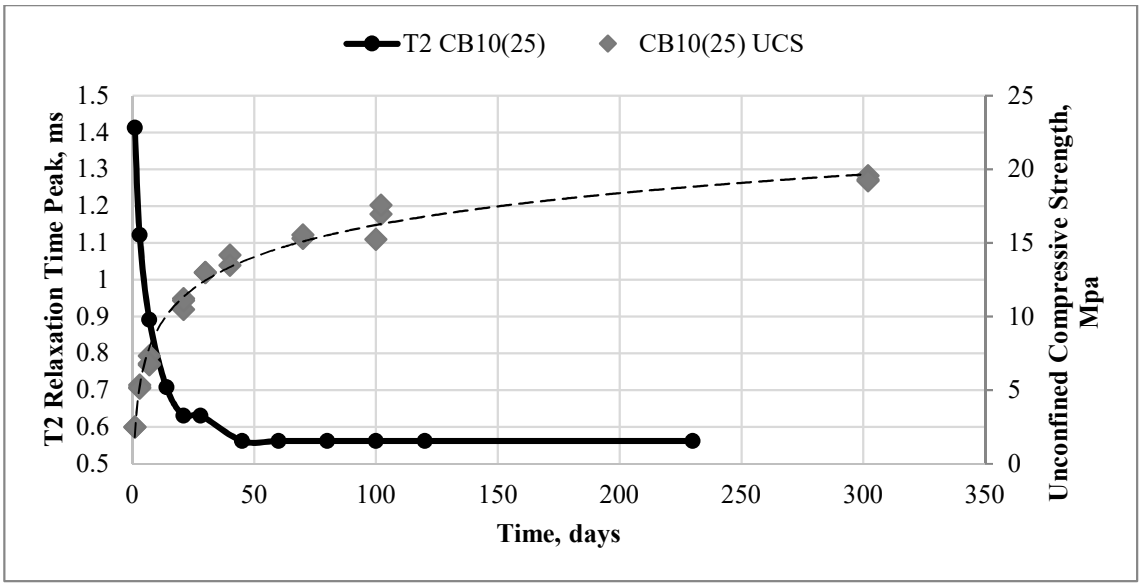

Figure 79 - 10% Bentonite Cement T_2 Peaks and UCS Evolution with Time (25°C)

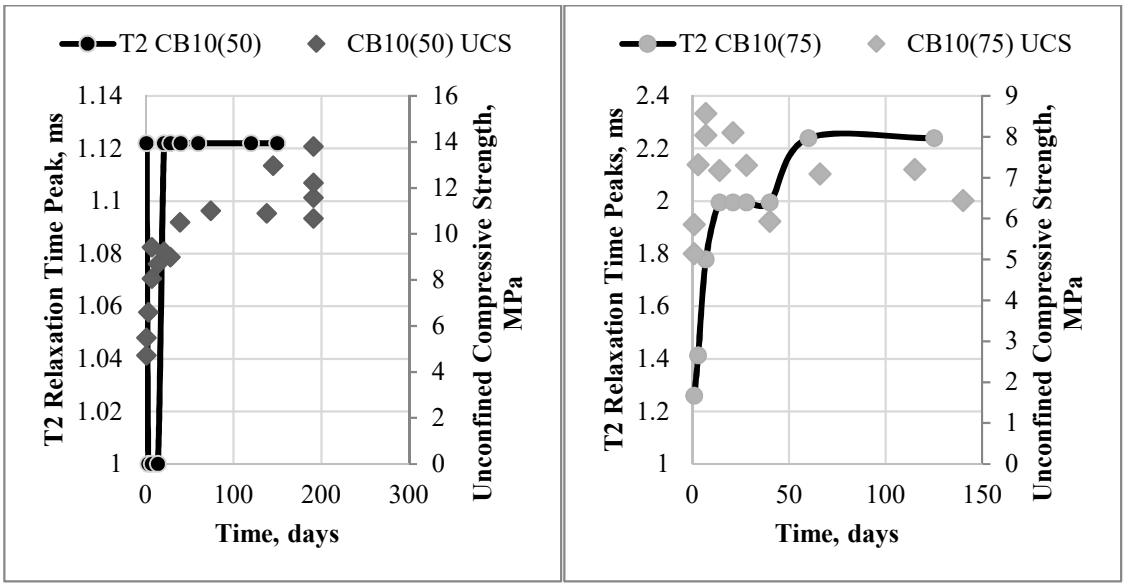

Figure 80 - 10% Bentonite Cement T_2 Peaks and UCS Evolution with Time (50°C – left and 75°C - right)

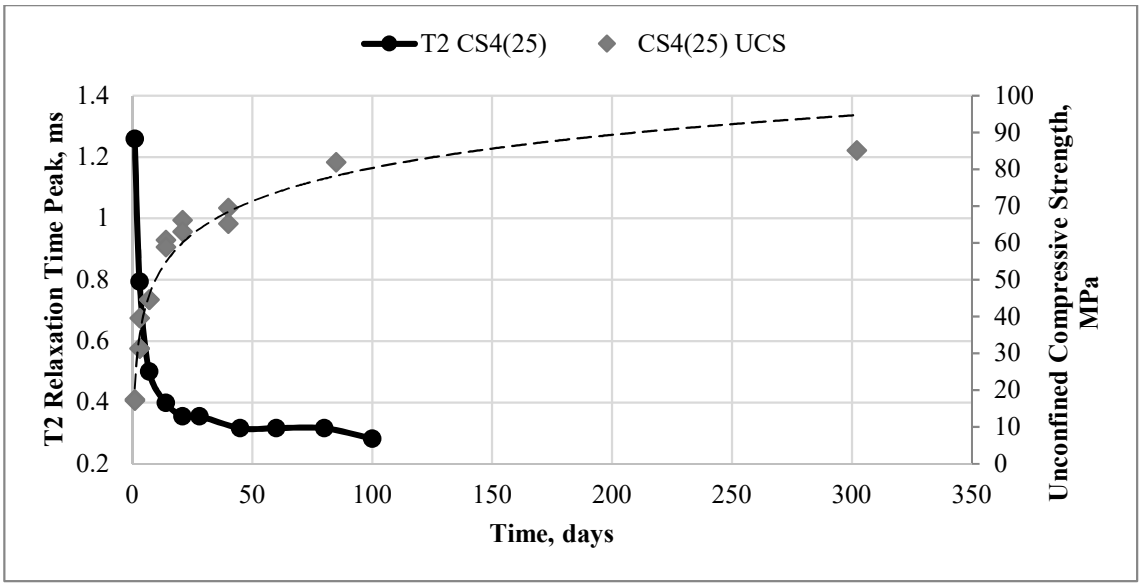

Figure 81 - 4% Salt Cement T_2 Peaks and UCS Evolution with Time (25°C)

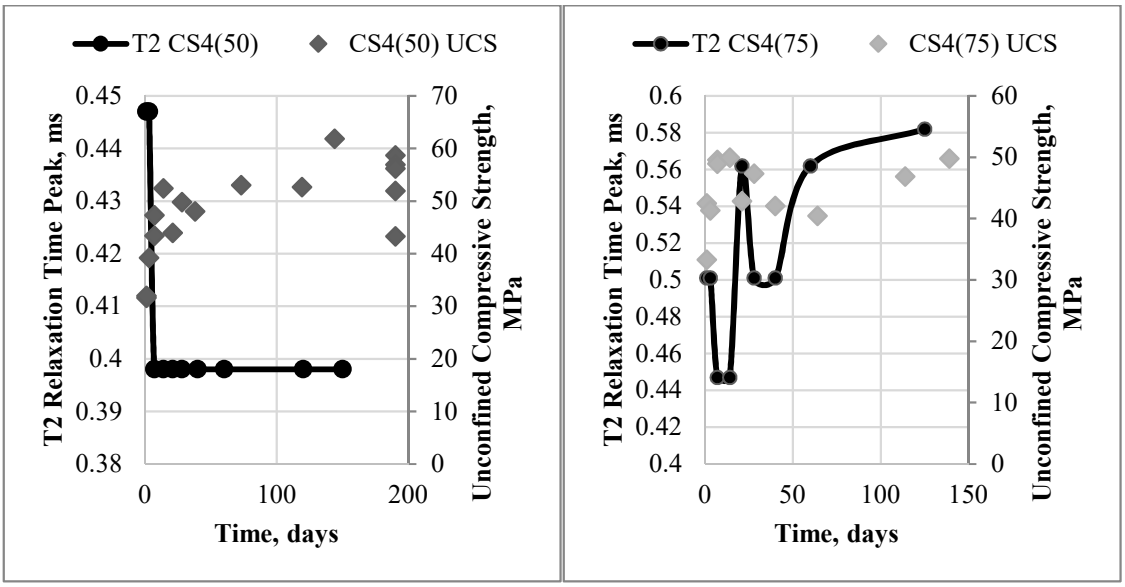

Figure 82 - 4% Salt Cement T_2 Peaks and UCS Evolution with Time (50°C – left and 75°C - right)

The 4% salt cement T_2 peaks correspond to the trends established at 25°C, as shown in **Figure 82** (left), where we see constant T_2 peaks with constant UCS at 50°C, and

increasing/decreasing T_2 peaks with decreasing/increasing UCS at 75°C (**Figure 82** – right).

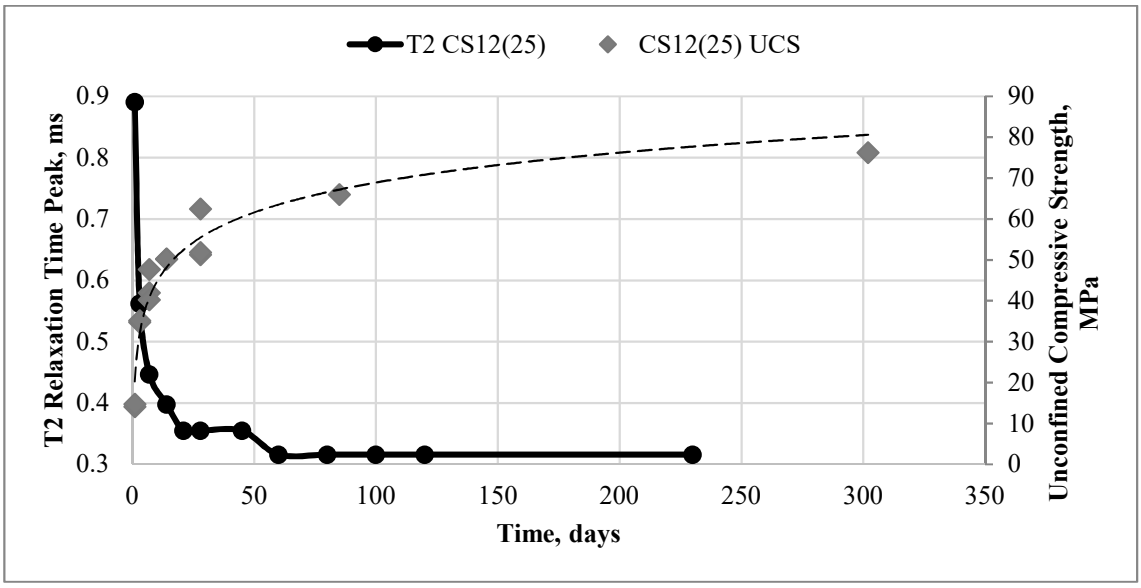

Figure 83 - 12% Salt Cement T_2 Peaks and UCS Evolution with Time (25°C)

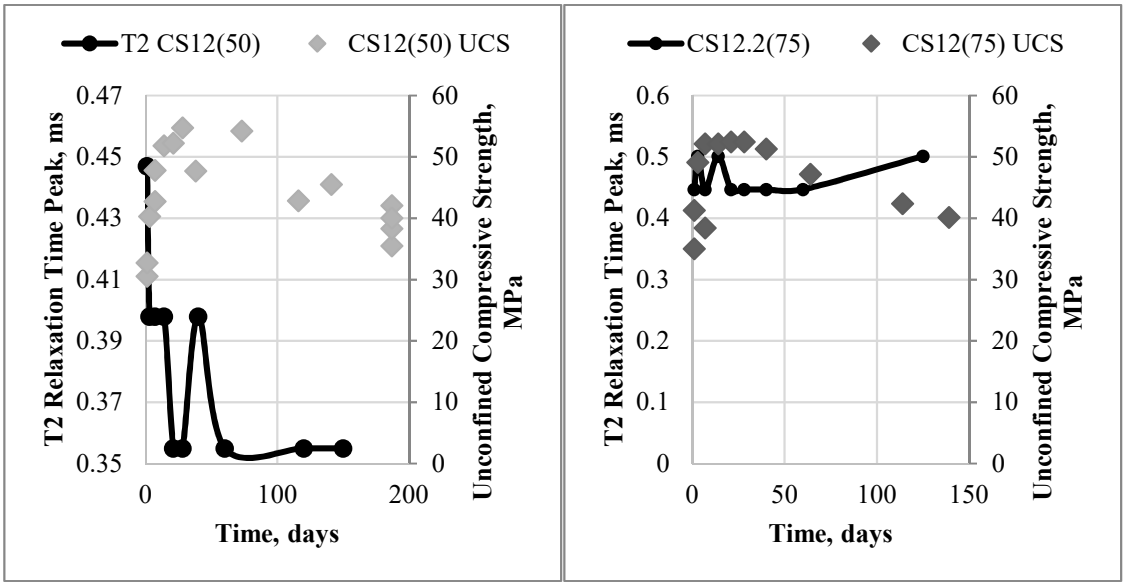

Figure 84 - 12% Salt Cement T_2 Peaks and UCS Evolution with Time (50°C – left and 75°C - right)

Finally, the 12% salt cement samples exhibit a behavior comparable to the 4% salt cements, with increasing T_2 peaks at lower strength, and constant peaks when UCS development stops (see **Figure 84**).

4.5. Saturation Profile Distribution Measurements

DHK SPRITE measurements were performed on samples cured at 50°C and 75°C at three times, and on old samples cured at 25°C. These measurements offer a one-dimensional distribution of the saturation profile in each sample across its length. Because of varying geometries, sample' lengths have been converted to percentage from the sample bottom. As an exercise, three different slices of neat cement and cement with 4% and 10% bentonite were stacked in three different combinations and placed in a glass vial. After determining the geometry, a gradient measurement has been run to see if different saturations can be captured by the NMR system.

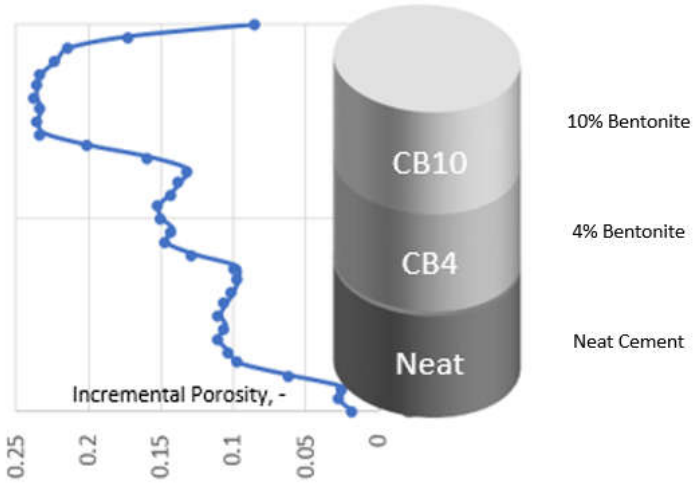

Figure 85 – Stacked Samples Saturation Profile – CB10/CB4/CN

As shown in **Figures 85** and **86**, the NMR signal clearly differentiates between the different samples, since these contain different water volumes.

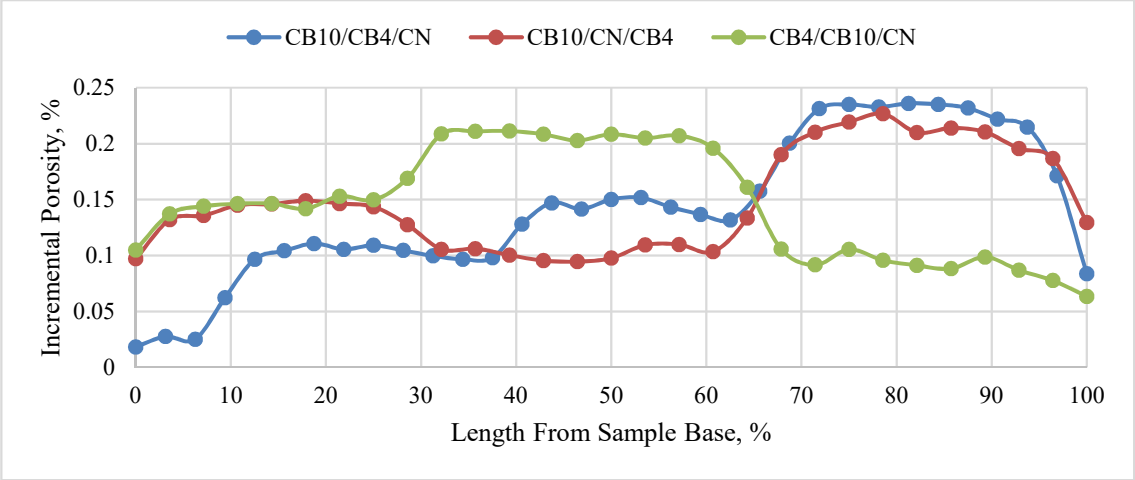

Figure 86 – Stacked Configurations Saturation Profiles

Figure 87 shows that the neat cement saturation profile and water content are similar to the two salt cements, whereas the bentonite cements contain more water. Note saturation distributions are very homogeneous attesting to the uniformity and mixing of the samples.

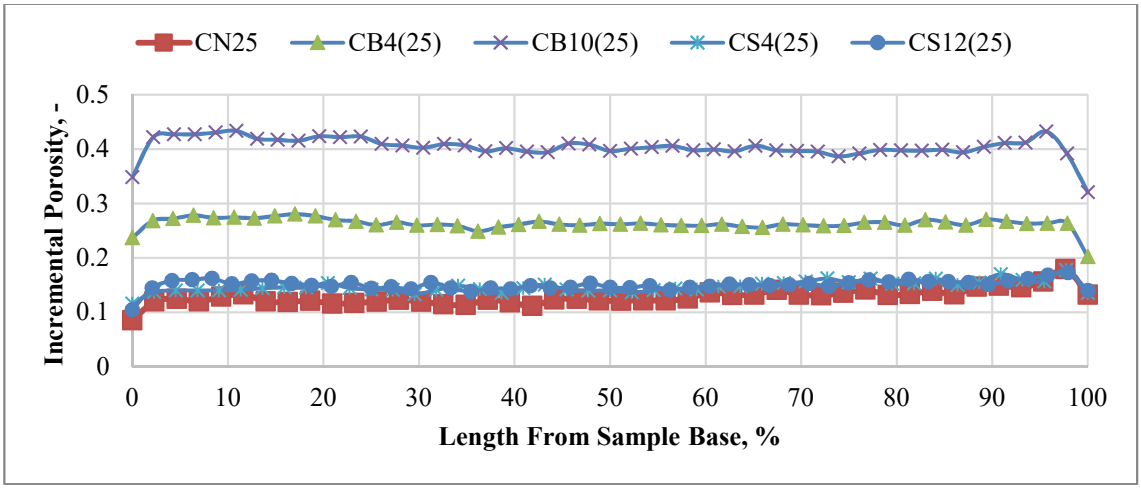

Figure 87 – Saturation Profiles of All Samples at Day 280

In samples cured at higher temperatures, the saturation increases from the bottom to the top of the sample, indicating water accesses the pore structure of the cement at different

times, i.e. 1 day, 50 days and 170 days. These observations are in line with those reported in Chapters 4.4.2 and 4.4.3.

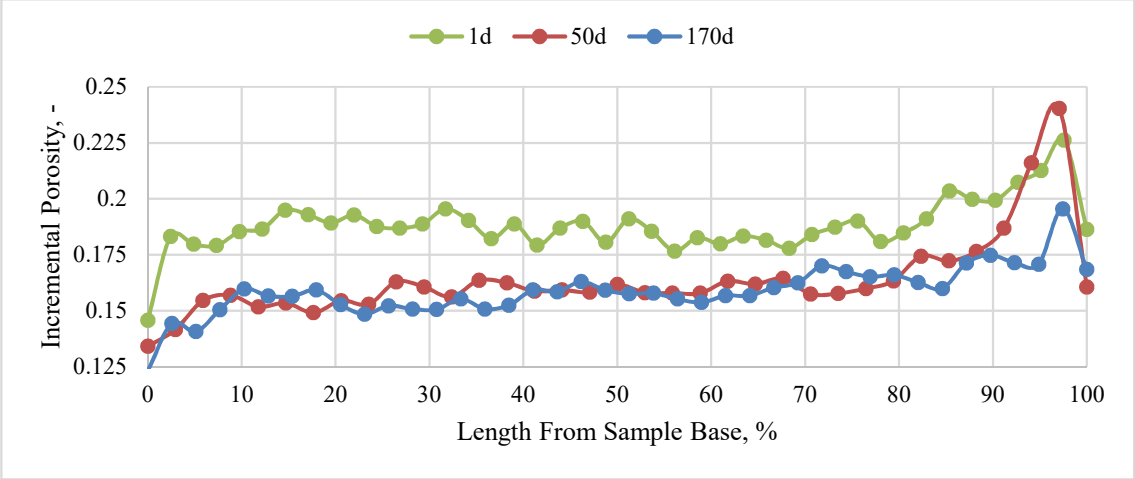

Figure 88 – Saturation Profile over Time - Neat Cement - 50°C

In samples with bentonite, a higher water saturation is observed. The saturation profile is linear in both the 4% and 10% bentonite cases and shows an increase closer to the sample base, instead of the sample top as observed in the other cases. This is more obvious at in the cement sample mixed with 10% bentonite (see **Figure 90**).

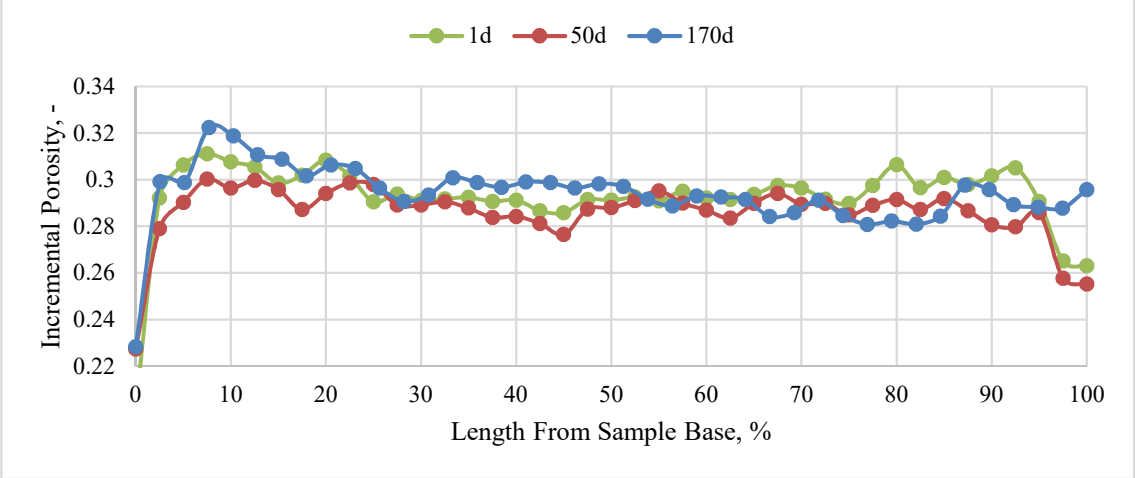

Figure 89 – Saturation Profile over Time - 4% Bentonite Cement - 50°C

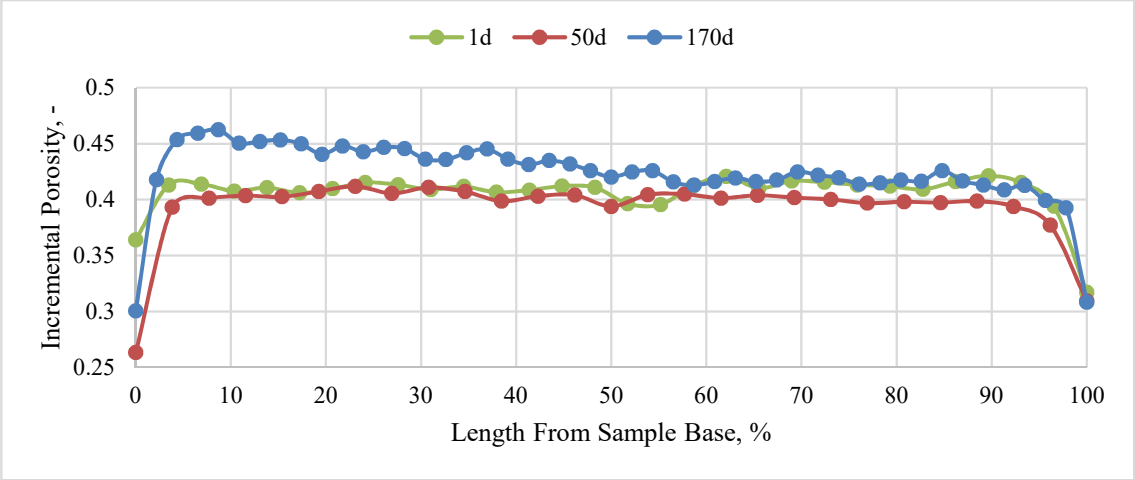

Figure 90 – Saturation Profile over Time - 10% Bentonite Cement - 50°C

The saturation profiles of salt cements at 50°C are similar to the water distribution in neat cement at different times. A decrease in the peak observed at 10% of the sample length is observed between days 1 and 50, and an increase of these shows at day 170, which may be explained by the water accessing the sample from the free water at the top of the sample.

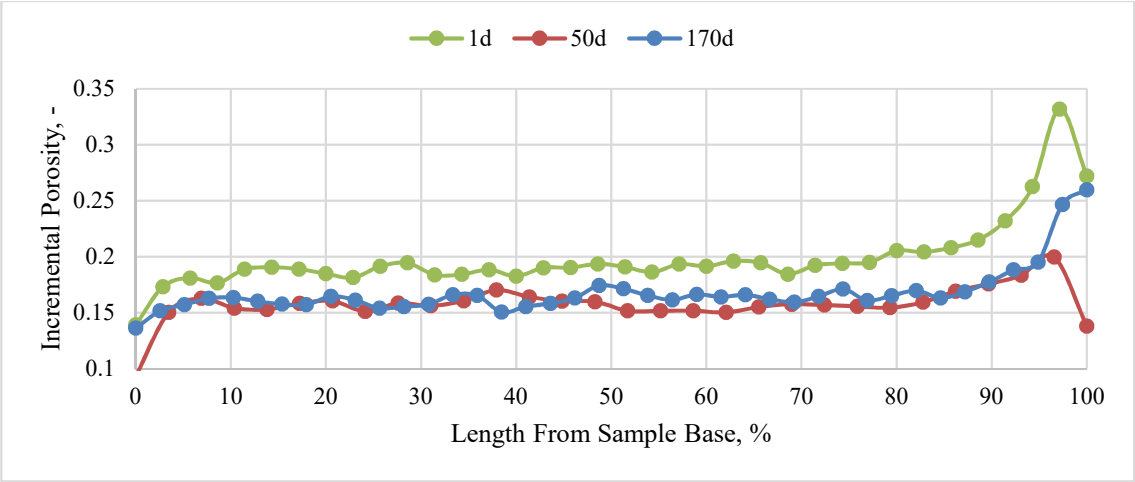

Figure 91 – Saturation Profile over Time - 4% Salt Cement - 50°C

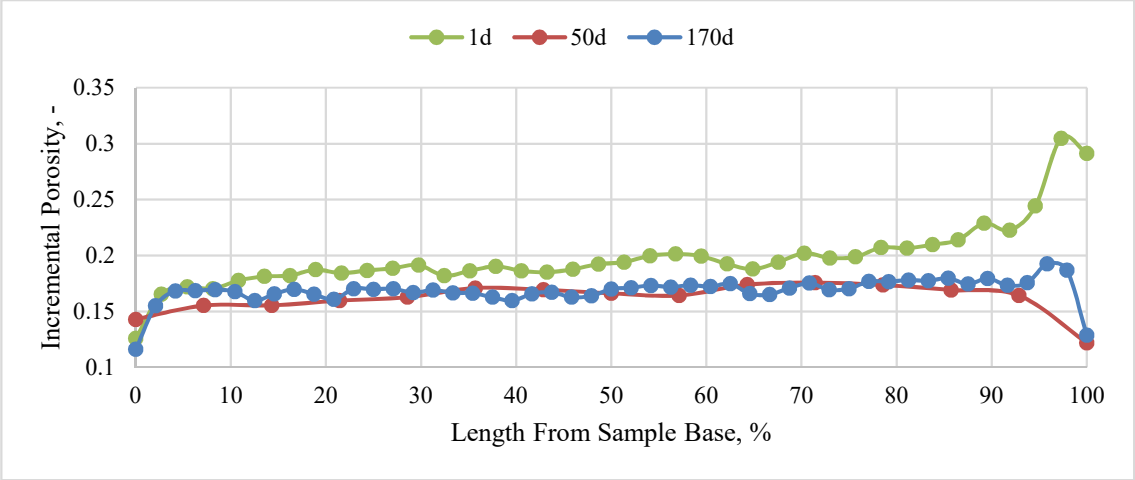

Figure 92 – Saturation Profile over Time - 12% Salt Cement - 50°C

The location of water seems to change with time due to various saturations at the different measurement times. This change of saturation is more obvious at 75°C, where the 170-days line clearly lays between the 1-day and 50-days lines, confirming the hypothesis of water accessing the sample at advanced curing times (see **Figures 93** to **97**).

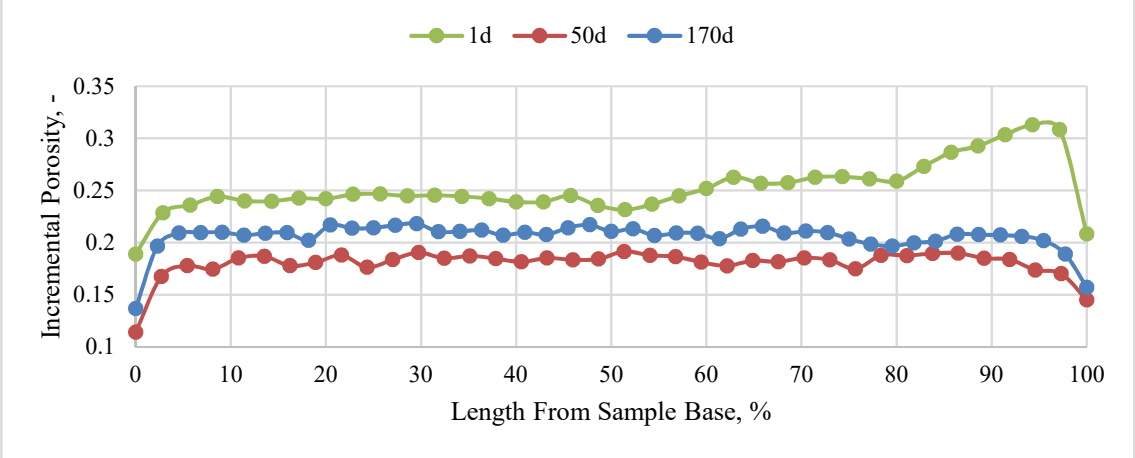

Figure 93 – Saturation Profile over Time - Neat Cement - 75°C

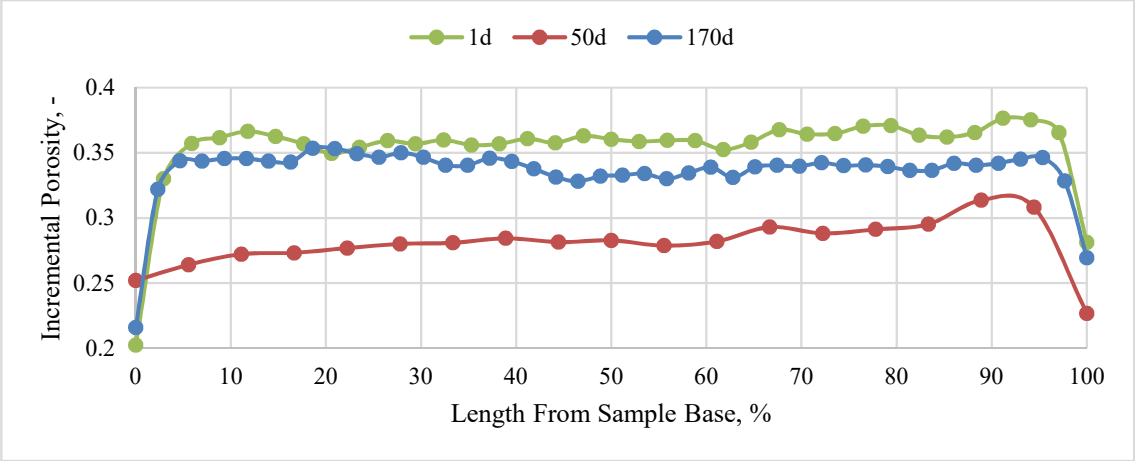

Figure 94 – Saturation Profile over Time - 4% Bentonite Cement - 75°C

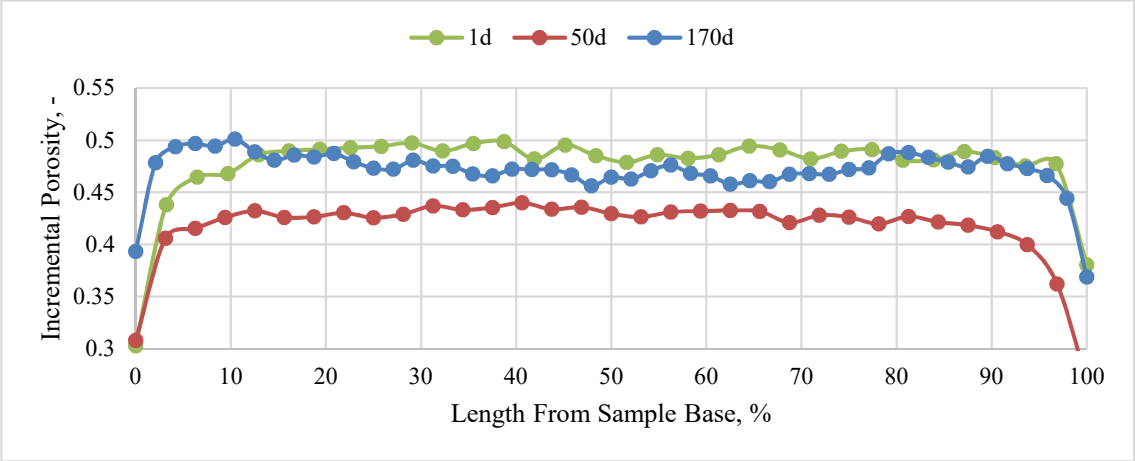

Figure 95 – Saturation Profile over Time -10% Bentonite Cement - 75°C

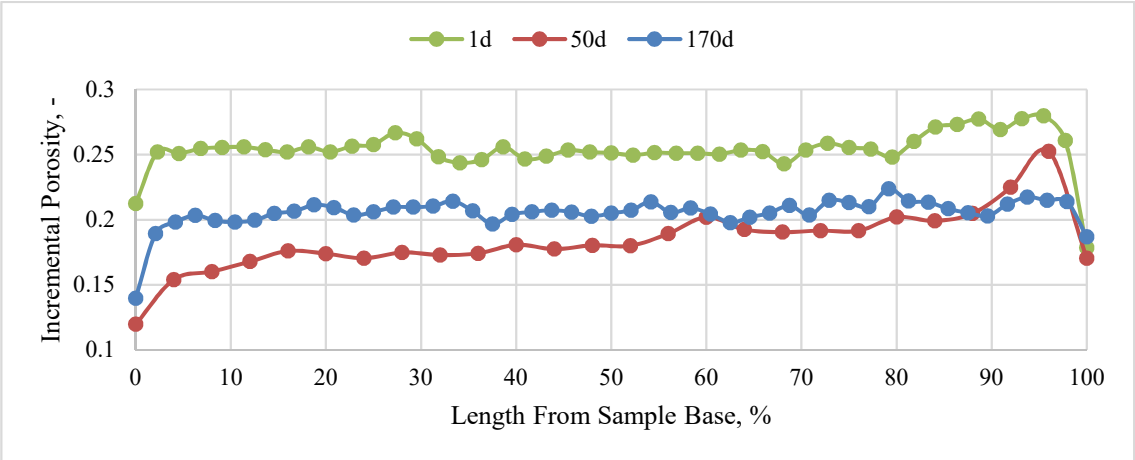

Figure 96 – Saturation Profile over Time - 4% Salt Cement - 75°C

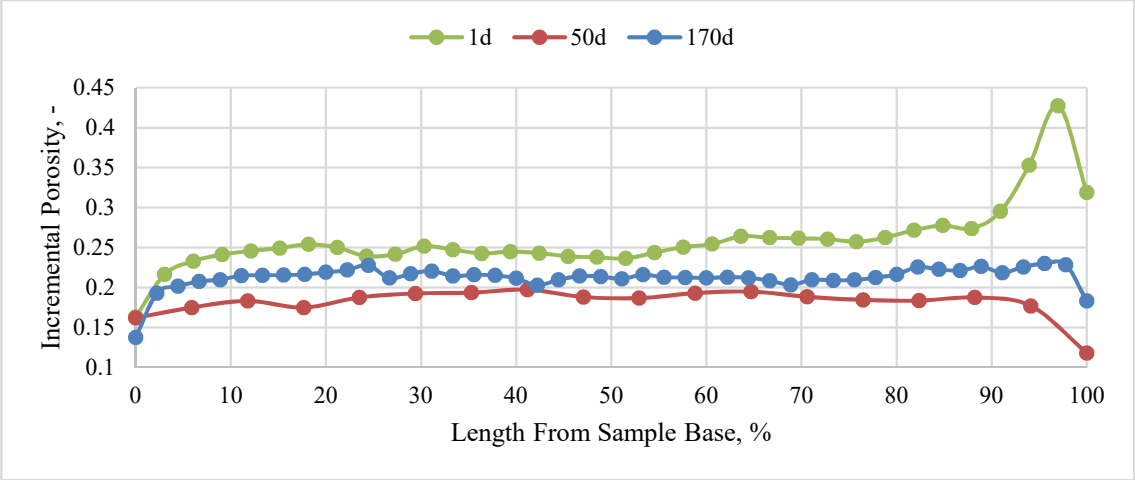

Figure 97 – Saturation Profile over Time - 12% Salt Cement - 75°C

4.6. T_1-T_2 NMR Measurements

T_1-T_2 measurements give us a two-dimensional map of the T_1 and T_2 relaxation times in the samples and their evolution with time and temperature. From these maps, it can be observed where the water is located at the time of measurement. At early hydration times, T_1 is larger than T_2, after which they both reach similar values, so that the processed data lies on the 1-to-1 line of the 2D map. The following only presents a few of the acquired maps, which show that, for example, in neat cement (**Figure 98**), relaxation times are around 10 ms for T_1 and 2 ms for 10 ms for T_2 at day 1, shifting to approximately 0.5 ms for T_1 and T_2 at day 60. Moreover, a shift from the 1:1 translates into a more viscous fluid at early hydration time, so transitioning to a solid can also be hypothesized. At higher temperatures, more signal is observed along the 1:1 lines. In the 10% bentonite samples, the trend is similar, but with larger relaxation times (see **Figure 99**).

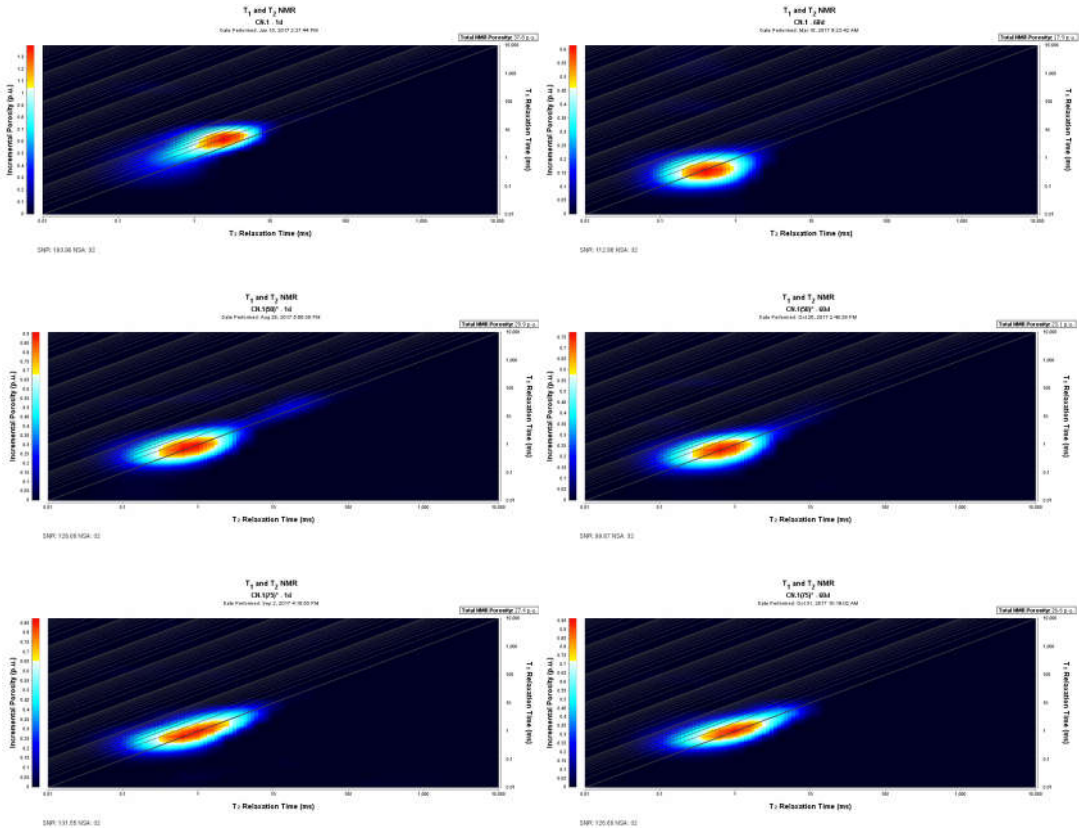

Figure 98 – Example of T_1-T_2 maps at 1 (left), and 60 (right) days for neat cement samples cured at 25°C (top), 50°C (center), and 75°C (bottom)

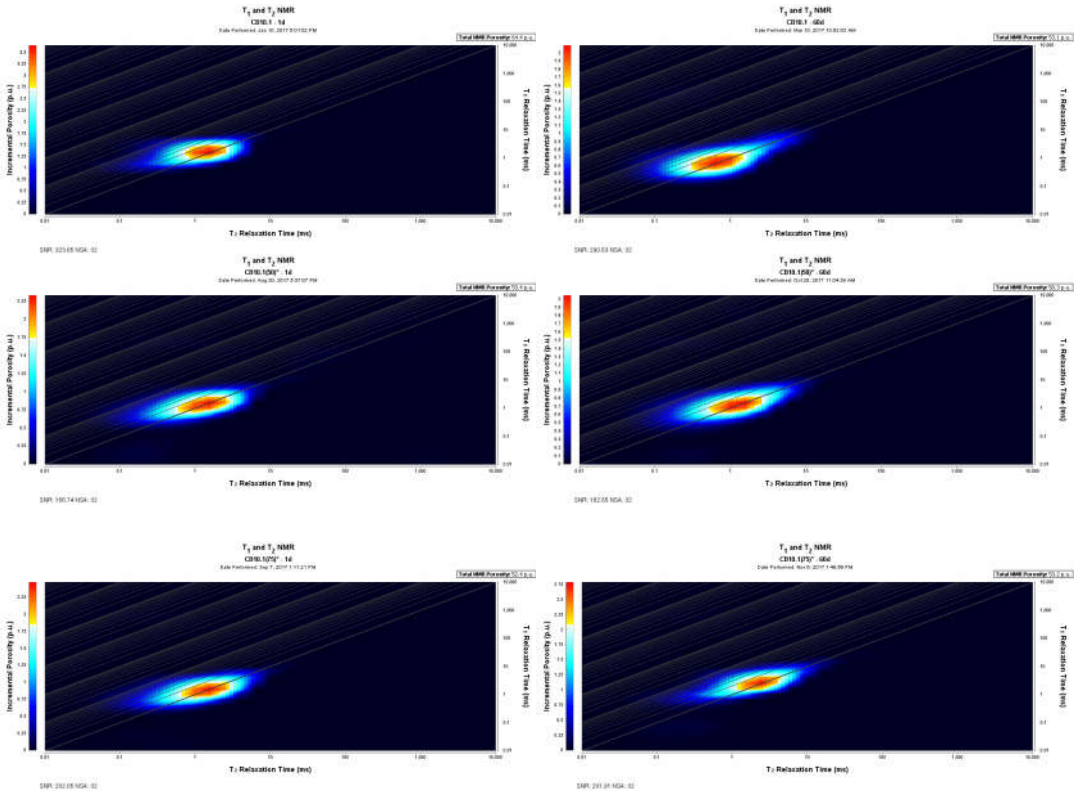

Figure 99 – Example of T_1-T_2 maps at 1 (left) and 60 (right) days for 10% bentonite cement samples cured at 25°C (top), 50°C (center), and 75°C (bottom)

5. Conclusions and Recommendations

This work presented experiments run on Class G cement mixed with and without additives and cured at 25°C, 50°C, and 75°C, and constant pressure for approximately two years. The influence of time, temperature, and additives on the performance of these cements was evaluated, and non-destructive testing methods were used to (1) develop correlations to assess cement mechanical properties and (2) understand the development of porosity and its influence on cement performance. The potential of NMR measurements as a NDT method for oilfield cements has been assessed and shows potential at surface temperatures. Through ultrasonic measurements, the dynamic elastic properties of the presented cement recipes under surface pressure and increasing temperature have been determined.

Throughout this work, the evolution of unconfined compressive strength of five cement recipes at three different temperatures was observed at times extending past what is defined as common times or standard testing times (up to 28 days). All strengths were evaluated at atmospheric pressure. Samples cured at room temperature exhibit a slow increase in UCS, leading to the highest final values of

- approximately 90 MPa for neat and salt cements,
- 37 MPa for the 4% bentonite cement and
- 20 MPa for the 10% bentonite cement,

whereas the increase in temperature shows higher initial strength in all samples at day 1, when compared to samples cured at 25°C:

- 150% at 50°C and 260% higher at 75°C in neat cements,
- 110% at 50°C and 160% higher at 75°C in 4% bentonite cements,

- 90% at 50°C and 106% higher at 75°C in 10% bentonite cements,
- 80% at 50°C and 88% higher at 75°C in 4% salt cements,
- and 111% at 50°C and 190% higher at 75°C in 12% salt cements,

but lower strength at longer times (around 100 days) when compared to values at 25°C:

- 20% at 50°C and 42% lower at 75°C in neat cements,
- 28% at 50°C and 41% lower at 75°C in 4% bentonite cements,
- 28% at 50°C and 53% lower at 75°C in 10% bentonite cements,
- 35% at 50°C and 42% lower at 75°C in 4% salt cements, and
- 35% lower at 50°C and 75°C in 12% salt cements.

Values for tensile strength were measured and presented at different times for samples cured at the 50°C and 75°C, showing that at a higher temperature, the tensile strength decreases by up to 50%. The tensile of neat cement at 50°c and 75°c is between 4.8 and 7.9 MPa, for salt cements between 4.8 and 6.7 MPa with no observable difference between 4% and 12% salt, and bentonite cements between 1.2 and 3.1 MPa, with the lower value corresponding to the 10% bentonite cement.

Ultrasonic testing allows the determination of cement transitioning from liquid to a solid, and of compressive strength through a non-destructive test. The measurements carried in this study allow the development of better correlations between UCS and UPV through the inclusion of the used additive in cement and the curing temperature. These are shown in the following table, and can be further programmed into commercial-type ultrasonic cement analyzers for comparison. Further research in this direction may include additional concentrations of different chemicals to see which have an impact of the relation between UCS and UPV, and how large this impact might be.

Table 12 – Correlations for All Cement Types at All Temperatures

Cement Type	25°C	50°C	75°C
Neat	$UCS = 0.0136e^{0.0022Vp}$	$UCS= 0.2901e^{0.0014Vp}$	$UCS = 1.8104e^{0.001Vp}$
	$R^2 = 0.95$	$R^2 = 0.86$	$R^2 = 0.63$
4% Bentonite	$UCS=0.084e^{0.0019Vp}$	$UCS = 0.154e^{0.0017Vp}$	$UCS = 0.1701e^{0.0018Vp}$
	$R^2 = 0.96$	$R^2 = 0.93$	$R^2 = 0.82$
10% Bentonite	$UCS = 0.0348e^{0.0023Vp}$	$UCS = 0.0386e^{0.0023Vp}$	$UCS = 0.4283e^{0.0013Vp}$
	$R^2 = 0.98$	$R^2 = 0.91$	$R^2 = 0.86$
4% Salt	$UCS = 0.1767e^{0.0015Vp}$	$UCS = 0.6843e^{0.0012Vp}$	$UCS = 1.1583e^{0.0011Vp}$
	$R^2 = 0.97$	$R^2 = 0.91$	$R^2 = 0.86$
12% Salt	$UCS = 0.3436e^{0.0014Vp}$	$UCS = 0.7738e^{0.0012Vp}$	$UCS = 0.0211e^{0.0023Vp}$
	$R^2 = 0.99$	$R^2 = 0.81$	$R^2 = 0.89$

*UCS in MPa and Vp in m/s

Moreover, dynamic elastic properties for all cement types have been estimated at 50°C and 75°C, and lower Young's moduli for the 75°C batches are observed in all cases, with up to 24% less (in the case of neat cement). Poisson's ratio varies between 0.29 and 0.35. The evolution of porosity through NMR measurements is followed for up to 300 days and insights that are more specific are offered for the various cement recipes cured at different temperatures. Additionally, $T_1 - T_2$ and DHK-Sprite measurements were used to further understand the hydration process, and later invasion of water from an external source.

By taking temperature into account, it is observed how NMR porosity values vary over time between

- 24% and 43.8% for neat cement,
- 40% and 57% for 4% bentonite cements,
- 51% to 69% for cement mixed with 10% bentonite,
- 30% to 44.5% for cement mixed with a 4% salt brine, and
- 30% to 44% for 12% salt cements.

With higher curing temperatures, initial porosities decrease by up to 25%. Oscillations in NMR porosity values with time are observed at higher curing temperatures of 50°C and 75°C; in contrast, the evolution at room temperature, is defined by an initial decay, followed by a constant behavior. This can be explained by water invasion from external sources, behavior which is very important downhole. DHK SPRITE measurements were used to view the water distribution profiles in the samples at different times, showing through late-time measurements (day 170) that at 75°C, more water is present in the sample than at 50 days, but less than in day 1, confirming water accessing the cylindrical sample over time from the top. Finally, T_1-T_2 measurements show the transitioning of the water in the sample from a viscous fluid to a solid state, and its location at different points in time.

From the standpoint of wellbore integrity, this research provides a large amount of data related to the compressive strength of five different cement slurries cured for long times at three different temperatures, which are useful in the evaluation of wellbore stresses under different loads. We show the necessity of advanced testing to understand the ultrasonic response of cements based on temperature and additives, and how non-destructive testing methods can be improved for a better assessment of cement mechanical and elastic properties. Finally, data related to the development of NMR porosity and saturation is published, all important in better describing and understanding cement-water reactions, water content evolution with time, water invasion, and pore size distribution, which influence well integrity and potential risks at a young age and on the long term.

References

Ahmed, Ramadan M., Nicholas Takach, U.M. Khan, and Rune Godøy. 2009. "Rheology of Foamed Cement." *Cement and Concrete Research* 39 (4): 353-361. doi:j.cemconres.2008.12.004.

Aïtcin, Pierre-Claude, and Robert J. Flatt. 2016. *Science and Technology of Concrete Admixtures.* Elsevier.

American Petroleum Institute. 2010. *ANSI/API Spec 10A - Specification for Cements and Materials for Well Cementing.* Washington, D.C.: American Petroleum Institute.

—. 2013. *API RP 10 B-2, Recommended Practice for Testing Well Cements.* Second. Washington, D.C.: American Petroleum Institute.

ASTM International. 2016. "ASTM D3967-16 Standard Test Method for Splitting Tensile Strength of Intact Rock Core Specimens." (ASTM International). doi:10.1520/D3967-16.

—. 2015. *ASTM E494 - Standard Practice for Measuring Ultrasonic Velocity in Materials.* West Conshohocken, PA: ASTM International. doi:https://doi.org/10.1520/E0494-15.

Barrie, Patrick J. 2000. "Characterization of porous media using NMR methods." *Annual Reports on NMR Spectroscopy* (Academic Press) 41: 265-316. doi:10.1016/S0066-4103(00)41011-2.

Blinc, R., M. Burgar, G. Lahajnar, and M. Rozmarin. 1978. "NMR Relaxation Study of Adsorbed Water in Cement and C3S Pastes." *Journal of the American Ceramic Society* 61: 35-37. doi:10.1111/j.1151-2916.1978.tb09224.x.

Bourgoyne Jr, A.T., K.K. Millheim, M.E. Chenevert, and F.S. Young Jr. 1991. *Applied Drilling Engineering.* Richardson, Texas: Society of Petroleum Engineers.

BP p.l.c. 2017. *BP Energy Outlook.* London: BP p.l.c.

Bryant, Ben. 2011. *Deepwater Horizon, Key Questions Answered.* April 20. https://www.theguardian.com/environment/2011/apr/20/deepwater-horizon-key-questions-answered.

Carino, N.J. 1994. "Nondestructive Testing of Concrete: History and Challenges." *Special Publication* (American Concrete Institute (ACI)) 623-678.

Coates, George R., Lizhi Xiao, and Manfred G. Prammer. 1999. *NMR Logging Principles and Applications.* Houston: Halliburton Energy Services.

Dalas, Florent, Jean-Pierre Korb, Sylvie Pourchet, Andre Nonat, David Rinaldi, and Martin Mosquet. 2014. "Surface Relaxivity of Cement Hydrates." *Journal of Physical Chemistry* 118: 8387-8396. doi:10.1021/jp500055p .

Davies, Richard J., Sam Almond, Robert S. Ward, Robert B. Jackson, Charlotte Adams, Fred Worall, Liam G. Herrigshaw, Jon G. Gluyas, and Mark A. Whitehead. 2014. "Oil and gas wells and their integrity: Implications for shale and unconventional resource exploitation." *Marine and Petroleum Geology* 56: 239-254.

De Bruijn, G., A. Loiseau, A. Chougnet-SIrapian, B. M. Piot, E. Pershikova, W. Khater, and G. Wilson. 2010. "Innovative Cementing Solution for Long-term Steam Injection Well Integrity." *SPE EUROPEC/EAGE Annual Conference and Exhibition.* Barcelona, Spain: Society of Petroleum Engineers. doi:10.2118/131324-MS.

Deane-Shinbrot, Steven, Kassandra Ruggles, Griffin Walker, and Sheila Werth. 2011. *Marcellus Shale: Cementing and Well Casing Violations.* Worcester, Massachusetts: Worcester Polytechnic Institute.

Doherty, D. R., and A. Brandl. 2010. "Pushing Portland Cement Beyond The Norm Of Extreme High Temperature." *IADC/SPE Asia Pacific Drilling Technology Conference and Exhibition.* Ho Min Chin, Vietnam: Society of Petroleum Engineers. doi:10.2118/134422-MS.

Dunn, K. -J., D.J. Bergman, and G.A. Latorracca. 2002. *Nuclear Magnetic Resonance Petrophysical and Logging Applications.* Oxford: Elsevier Science Ltd.

Eid, Ramy, and Patric Mays. 2007. "Liquid Cement: Changing the Paradigm." *Latin American & Caribbean Petroleum Engineering Conference.* Buenos Aires, Argentina: Society of Petroleum Engineers. doi:10.2118/105500-MS.

Eilers, L. H., and E. B. Nelson. 1979. "Effect Of Silica Particle Size On Degradation Of Silica Stabilized Portland Cement." *SPE Oilfield and Geothermal Chemistry Symposium.* Houston, Texas: Society of Petroleum Engineers. doi:10.2118/7875-MS.

Elkhadiri, I., M. Palacios, and F. Puertas. 2009. "Effect of curing temperature on hydration." *Ceramics - Silikaty* 53 (2): 65-75.

Exxon Mobil Corporation. 2017. *2017 Outlook for Energy: A View to 2040.* Irving, Texas: Exxon Mobil Corporation.

Fink, Johannes. 2015. *Petroleum Engineer's Guide to Oil Field Chemicals and Fluids.* 2nd. Elsevier.

Garnier, A., B. Fraboulet, J. Saint-Marc, and A. Bois. 2007. "Characterization of Cement Systems to Ensure Cement Sheath Integrity." *Offshore Technology Conference.* Houston, TX: Offshore Technology Conference. doi:10.4043/18754-MS.

Green Imaging Technologies, Inc. 2016. *Hardware Setup and Calibration Manual.* Fredericton, NB, March.

Greener, Jessie, Hartwig Peemoeller, Changho Choi, Rick Holly, Eric J. Reardon, Carolyn M. Hansson, and Mik M. Pintak. 2000. "Monitoring of Hydration of White Cement Paste with Proton NMR." *Journal of American Ceramic Society* 83 (3): 623-627.

Griffith, Bob. 2013. *Comprehensive Oil, Gas and UIC Inspections in Oklahoma.* Grapevine, Texas: Groundwater Protection Council Spotlight Series.

Gutteridge, Walter A., and John A. Dalziel. 1990. "Filler Cement: The Effect of Secondary Component on the Hydration of Portland Cement." *Cement and Concrete Research* (Pergamon Press plc.) 20: 778-772. doi:10.1016/0008-8846(90)90011-L.

Halliburton. 2017. *Cementing Bentonite.* October 12. http://www.halliburton.com/public/cem/contents/chem_ compliance/web/h02088-a4.pdf.

—. 1994. "Halliburton Cementing Tables."

Halperin, W.P., J.-Y Jehng, and Y.-Q Song. 1994. "Application of spin-spin relaxation to measurement of surface area and pore size distributions in a hydrating cement paste." *Magnetic Resonance Imaging* 12 (2): 169-173. doi:10.1016/0730-725X(94)91509-1.

Henry, Terrence. 2012. *Stateimpact.* January 6. https://stateimpact.npr.org/texas/2012/01/06/chesapeake-fracking-well-catches-fire-oklahoma/.

Hibbeler, J., P. Rae, T. Gilmore, and L Weber. 2000. "Using Alternative Sources of Oilwell Cement." *IADC/SPE Asia Pacific Drilling Technology.* Kuala Lumpur, Malaysia: Society of Petroleum Engineers. doi:10.2118/62746-MS.

Hole, H. M. 2008. *Geothermal Well Cementing.* Vol. Workshop 28. Dubrovnik: Petroleum Engineering Summer School.

Hornak, Joseph P. 2017. *The Basics of NMR.* 11 1. https://www.cis.rit.edu/htbooks/nmr/

Ichim, Adonis. 2015. *Effect of Cement Thermal Properties on Heat Transfer in HP/HT Wells.* Clausthal-Zellerfeld: Clausthal University of Technology.

Ichim, Adonis, Antonio Marquez, and Catalin Teodoriu. 2016. *How Accurate is Your Well Integrity? A Discussion About the Surface Casing Integrity Under Temperature Loading in Heavy Oil Fields.* Lima: Society of Petroleum Engineers. doi:doi:10.2118/181154-MS.

Keating, J., D. J. Hannant, and A. P. Hibbert. 1989. "Correlation Between Cube Strength, Ultrasonic Pulse Velocity, and Volume Change for Oil Well Cement Slurries." *Cement and Concrete Research* (Pergamon Press plc) 19 (5): 715-726.

Kiran, Raj, Catalin Teodoriu, Younas Dadmohammadi, Runar Nygaard, David Wood, Mehdi Mokhtari, and Saeed Salehi. 2017. "Identification and evaluation of well integrity and causes of failure of well integrity barriers (a review)." *Journal of Natural Gas Science and Engineering* (Elsevier) 45: 511-526.

Königsberger, Markus, Christian Hellmich, and Bernhard Pichler. 2016. "Densification of C-S-H is mainly driven by available precipitation space, as quantified through an analytical cement hydration model based on NMR data." *Cement and Concrete Research* 170-183. doi:10.1016/j.cemconres.2016.04.006.

Labibzadeh, Mojtaba, Behzad Zahabizadeh, and Amin Khajehdezfuly. 2010. "Early-age compressive strength assessment of oil well class G cement due to borehole pressure and temperature changes." *Journal of American Science* 38-47.

Luke, Karen, Chris Hall, Tim Jones, Paul Barnes, Xavier Turillas, and Andrew Lewis. 1995. "New Techniques for Monitoring Cement Hydration Under Simulated Well Conditions." *SPE International Symposium on Oilfield Chemistry.* San Antonio, TX, USA: Society of Petroleum Engineers. doi:10.2118/28958-MS.

Macalister, Terry. 2013. *Piper Alpha disaster: how 167 oil rig workers died.* July 4. https://www.theguardian.com/business/2013/jul/04/piper-alpha-disaster-167-oil-rig.

Maharidge, R., A. Bottiglieri, S.S. Dighe, A. Holley, A. Zhang, and A. Koch. 2016. "Development of Permeability and Mechanical Properties of Class G Cement from Slurry to Set." *SPE Annual Technical Conference and Exhibition.* Dubai, UAE: Society of Petroleum Engineers. doi:10.2118/181512-MS.

McDonald, P., J.P. Korb, J. Mitchell, and L. Monteilhet. 2005. "Surface relaxation and chemical exchange in hydrating cement pastes: a two-dimensional NMR relaxation study." *Physical Review E* (American Physical Society) 72 (1). doi:10.1103/PhysRevE.72.011409.

Minja, Frank, and Gillian Lieberman. 2017. *The Basics of MRI: T1 vs. T2.* September 12. http://eradiology.bidmc.harvard.edu/LearningLab/central/minja.pdf.

Morgan, B.E., and G. K. Dumbauld. 1953. "Recent Developments in The Use of Bentonite Cement." *Drilling and Production Practice.* New York, USA: American Petroleum Institute. 163-176.

Mountain Cement Company. 2017. "Safety Data Sheet." Laramie, WY, USA.

Muir, Colleen E., and Bruce J. Balcom. 2012. "Pure Phase Encode Magnetic Resonance Imaging of Fluids in Porous Media." *Annual Reports on NMR Spectroscopy*, 81-113.

Muller, Arnaud Charles Albert. 2014. *Characterization of Porosity & C-S-H in Cement Pastes by 1H NMR.* Lausanne: Ecole Polytechnique Federale de Laussane.

Muller, Arnaud, Karen L. Scrivener, Agata M. Gajewicz, and Peter J. McDonald. 2012. "Densification of C−S−H Measured by 1H NMR Relaxometry." *Journal of Physical Chemistry* (American Chemical Society) 117: 403-412. doi:10.1021/jp3102964.

National Institute of Standards and Technology. 2017. *Cement and Concrete Characterization.* 11 1. https://www.nist.gov/el/materials-and-structural-systems-division-73100/inorganic-materials-group-73103/concrete-1.

Nelson, E.B. 1990. *Well Cementing.* 1st. Vol. 28. Elsevier Science.

Nguyen, Tan. 2017. *Well Design.* October 10. infohost.nmt.edu/~petro/faculty/Nguyen/PE413/Presentation/C3/2_Classification_Additives_Calculations.ppt.

Noik, C., A. Rivereau, and C. Vernet. 1998. "Novel Cements Materials for High-Pressure / High-Temperature Wells." *European Petroleum Conference.* The Hague, Netherlands: Society of Petroleum Engineers. doi:10.2118/50589-MS.

NORSOK. 2004. *D-010 Well integrity in drilling and well operations.* Norsk Sokkels Konkurranseposisjon.

OFITE. 2017. "Ultrasonic Cement Analyzer, Dual Cell, 20 KSI." *OFITE.* October 23. http://www.ofite.com/doc/120-52_brochure.pdf.

Oil & Gas UK. 2016. *Decommissioning Insight Report 2016.* London: The UK Oil and Gas Industry Association Limited.

Omosebi, O., Ramadan Ahmed, and S. Shah. 2017. "Mechanisms of Cement Degradation in HPHT Carbonic Acid Environment." *SPE International Conference on Oilfield Chemistry.* Montgomery, Texas, USA: Society of Petroleum Engineers. doi:10.2118/184567-MS.

Patchen, F.D. 1960. "Reaction and Properties of Silica-Portland Cement Mixtures at Elevated Temperatures." *Journal of Petroleum Technology* 219.

Pike, William J. 1997. "New Technology Improves Cement Slurry Design." *Journal of Petroleum Technology* 49 (8): 844-845. doi:10.2118/0897-0844-JPT.

Powers, T.C. 1958. "Structure and Physical Properties of Hardened Portland Cement Paste." *Journal of the American Ceramic Society* 41 (1): 1-6.

Rao, Prabhakar, P., David L. Sutton, Jerry D. Childs, and Willis C. Cunningham. 1982. "An Ultrasonic Device for Nondestructive Testing of Oilwell Cements at Elevated Temperatures and pressures." *Journal of Petroleum Technology* (Society of Petroleum Engineers) 34 (11): 2611-2616. doi:10.2118/9283-PA.

Romanowski, Niklas, Adonis Ichim, and Catalin Teodoriu. 2017. "Investigations on Oilwell Cement Response to Ultrasonic Measurements in the Presence of Additives." *ASME 2017 36th International Conference on Ocean, Offshore and Arctic Engineering.* Trondheim: ASME.

Saleh, Fatameh, Adonis Ichim, Catalin Teodoriu, and Daniel Mbainayel. 2017. "A Quantification of Mixing Energy During the Whole Cementing Cycle." *Proceedings of the 36th International Conference on Ocean, Offshore & Arctic Engineering.* Trondheim: ASME.

Saunders, Calvin D., and Wayne A. Walker. 1954. "Strength of Oil Well Cements and Additives under High Temperature Well Conditions." *Fall Meeting of the Petroleum Branch, American Institute of Mining and Metallurgical Engineers.* San Antonio, TX: Society of Petroleum Engineers International.

Schreiner, L.J., J.C. Mactavish, L. Miljkovic, M.M. Pintar, R. Blinc, G. Lahajnar, D. Lasic, and L.W. Reeves. 1985. "NMR Line Shape-Spin-Lattice Relaxation Correlation Study of Portland Cement Hydration." *Journal of the American Ceramic Society* 68 (1): 10-16. doi:10.1111/j.1151-2916.1985.tb15243.x.

Shuker, Muhannad, Khalil R. Memon, Saleem Q. Tunio, and Muhammad K. Memon. 2014. "Laboratory Investigation on Performance of Cement Using Different Additives Schemes to Improve Early Age Compressive Strength." *Research Journal of Applied Sciences, Engineering and Technology* 7 (11): 2298-2305. doi:10.19026/rjaset.7.529.

Slagle, Knox A., and Dwight K. Smith. 1963. "Salt Cement for Shale and Bentonitic Sands." *Journal of Petroleum Technology* (Society of Petroleum Engineers) 15 (2): 187-194. doi:10.2118/411-PA.

SoCalGas. 2017. *Aliso Canyon Natural Gas Storage Facility.* November 3. https://www.socalgas.com/stay-safe/pipeline-and-storage-safety/aliso-canyon-storage-facility.

Sondergeld, Carl. 2017. *Introduction to Rock Properties.* Norman, Oklahoma: University of Oklahoma.

Teodoriu, Catalin, and Peter Asamba. 2015. "Experimental Study of Salt Content Effects on Class G Cement Properties with Application to Well Integrity." *Journal of Natural Gas Science and Engineering* (Elsevier) 324-329. doi:10.1016/j.jngse.2015.03.039.

US Energy Information Administration. 2017. *Annual Energy Outlook 2017.* Washington, D.C.: EIA.

Valori, A., P.J. McDonald, and K.L. Scrivener. 2013. "The Morphology of C-S-H: Lessons from 1H Nuclear Magnetic Resonance Relaxometry." *Cement and Concrete Research* 49: 65-81. doi:10.1016/j.cemconres.2013.03.011.

van Bruegel, K. 1991. *Simulation of Hydration and Formation of Structure in Hardening Cement-Based Materials.* Meinema, Delft: University of Delft.

Woods Hole Oceanographic Institution. 2014. *Oil in the Ocean.* July 28. http://www.whoi.edu/oil/ixtoc-I.

Appendix A: Methods to Assess Cement Properties

An overview of methods to investigate cement properties at a laboratory and field scale is presented throughout this appendix. From the laboratory methods, a more focused description of the approaches and devices used in this work is provided in Chapter 3.

According to the American Petroleum Institute, cement testing requires samples of cement, cement blend, solid and liquid additives, and mixing water. The sampling of separate or blended materials can be done at a field location, or at manufacturing facilities and transported in sealed containers to the testing facilities. If separate materials were sampled, laboratory mixing procedures must be similar to the field (American Petroleum Institute 2013).

After mixing, the slurry must be conditioned, or cured, to reflect expected conditions during slurry placement. API recommends using well temperature and pressures, or, conditioning at atmospheric pressure as an alternative (American Petroleum Institute 2013).

Standardized tests for oilfield cements can be divided into fluid tests and set cement tests. The ultrasonic response of cement evaluates the cement in both its liquid and solid form. Fluid tests are designed and used to understand the properties of the slurry after mixing, during pumping, and during the transition time before it sets. These include:

- *Slurry density measurements*
- *Thickening time tests*
- *Fluid loss tests*
- *Rheological properties and gel strength*
- *Slurry stability tests* (free fluid and sedimentation tests)

- *Compatibility of wellbore fluids*

Destructive and non-destructive tests are used to determine the compressive strength of set cement.

- *Compressive strength* determined through sample crushing.
- *Nondestructive sonic determination* of compressive strength of cement

Although not standardized through API, service companies, operators, research facilities and academia use more in-depth tests to better understand the development of multiple cement properties under various conditions. These properties may include, but are not limited to: tensile strength, flexural strength, Poisson's ratio, Young's modulus, cement permeability, cement porosity, and are usually standardized by other entities (e.g. American Society for Testing Materials, American Society of Mechanical Engineers, International Standards Organization). Other methods used to study the evolution of cement properties at a more detailed level include Fourier Transform Infrared Spectroscopy (FTIR), Synchrotron X-ray Powder Diffraction, Scanning Electron Microscopy (SEM), NMR, and electron energy loss spectroscopy (Luke, et al. 1995).

Cement porosity is usually measured by using dynamic vapor sorption, mercury intrusion porosimetry, scanning electron microscopy, and nuclear magnetic resonance, each with advantages, limitations, and precision. Also, methods which involve sample drying or pre-heating to eliminate water may damage the microstructure of cement change the outcomes of a study.

After wellbore placement, cements set and form a bond between casing and formation. When exposed to downhole conditions, their properties and behavior change, leading to the necessity of field evaluation of cement through downhole measurements. Kiran et al.

(2017) offer an extensive overview of such methods and their limitations, summarized in the following table.

Table A1 – Uses and Limitations of Downhole Tools for Determining Well Integrity (Kiran et al. 2017)

Method	Uses	Limitations
Cement Bond Log/Variable-Density Log	Predicts well-bonded cement, debonding at wet casing and formation	No prediction of mud channels, vertical cracks, gas chimney, and radial variation in cement
Ultra-Sonic Imaging Log(UBI)	Shows well-bonded cement, mud channel in good cement, gas chimney, and debonding at wet casing	Determining mud channels in weak cement, vertical cracks, debonding at dry casing and formation, and radial variation in cement
Isolation Scanner	Capable of showing good cement, mud channels, gas chimneys, thick vertical cracks, debonding at wet casing and formation, and cement radial variation	Predicting thin vertical cracks and debonding at dry casing
Radioactive Tracer Survey	Used for leak detection	Predicting the quality of cement or casing
Temperature Log/Noise Log	Detects anomalies due to leak	No insight on cement
Corrosion Log	Predicts the corrosion in the casing, tubular, and even casing behind cement (e.g. surface casing).	No insight on cement
SAPT/VIT*	Assessment of the hydraulic properties of the cemented annulus zone under study	No evaluation of cement and casing quality

*** Standard Annulus Pressure Test/Vertical Interference Test**

Appendix B: Experimental Procedures

B.1. Cement Mixing

Recommendations of the American Petroleum Institute have been followed during the mixing procedure. A bottom-driven, blade-type blender with an automated control unit was used (**Figure B1**). A slurry volume of 600 ml is mixed in the one-quart cup, to not overfill the mixing cup and ensure the mixing energy matches recommended values of 5.9 KJ/Kg, since mixing energy variations lead to different compressive strengths (Saleh et al. 2017). The temperature of water, cement, and additives is 22°C ± 2°C. Deionized water was used instead of water from the field source. The mix water is weighed in a clean, dry container. The recommended mixing schedule is 4,000 RPM ± 250 RPM for 15 s and 12,000 RPM ± 250 RPM for 35 s ± 1 s. The electronic control unit ensures a maximum deviation of ± 50 RPM from the API recommended numbers (American Petroleum Institute 2013)

Figure B1 – OFITE Automated Cement Mixing Unit (OFITE 2016)

Five different slurries were mixed by using an API certified mixing unit according to API 10 D:

1. Measure masses of water, cement, and additives.
2. Add water to mixing cup. If salt cements are mixed, create brine by mixing water with the necessary salt mass.
3. If bentonite cements are mixed, dry-mix the two powder components for approximately two minutes. Make sure to add an additional of 5.3% water per percent of bentonite powder added to ensure clay hydration and minimize water scavenging effects (Bourgoyne Jr, et al. 1991) (Nguyen 2017).
4. Start cement slurry mixer. The automatic mode will set the rotational speed to 4,000 RPM for 15 seconds, time in which the cement powder and additives must be added to the cup.
5. Place lid on top of the mixing cup. The rotational speed of the mixer will automatically increase to 12,000 RPM, creating a homogeneous slurry mixture.
6. The mixer will stop after a total of 50 seconds. Remove the lid and proceed with pouring the slurry into molds.

The masses of cements and additives were calculated by using the ideal mix density equations and data available from the cement and additive manufacturers together with API, also presented in Table 14.

$$\rho_{slurry} = \frac{M_{total}}{V_{total}} = \frac{(M_c + M_w + M_{add})}{(V_c + V_w + V_{add})} \tag{B1}$$

$$M_c = V_{total} \frac{\left(1 + \frac{W_w}{W_c} + \frac{W_{add}}{W_c}\right)}{\left(\frac{1}{\rho_c} + \frac{\frac{W_w}{W_c}}{\rho_w} + \frac{\frac{W_w}{W_c}}{\rho_{add}}\right)\left(1 + \frac{W_w}{W_c} + \frac{W_{add}}{W_c}\right)} \quad \text{(B2)}$$

Table B1 – Used Parameters and Densities

Parameter		**Value**
Total Mixing Volume	V_{total}	600 ml (API RP 10B-2)
Cement Density	ρ_c	3.15 kg/l (Mountain Cement Company 2017)
Water Density	ρ_w	1.00 kg/l (API RP 10B-2)
Bentonite Density	ρ_{add}	2.35 kg/l (Halliburton 2017)
Salt Density (NaCl)	ρ_{add}	2.17 kg/l (API RP 10B-2)

B.2. Cement Casting and Curing

Before casting the samples, density is measured by using an unpressurized oilfield mud balance. The balance is calibrated with purified water before each measurement. Reported values are within ±0.1 SG. from the ones calculated with Equation 1. This may be caused by slight variations in chemical densities, varying water density, air trapped in the cement slurry (especially in salt and bentonite slurries, where higher viscosity prevents air from exiting the sampling cup through the orifice in the top lid). Before pouring the slurry into the molds, their inside walls are coated with an easy-applicable, inert, noncorrosive at curing temperature, watertight release agent (industrial grease), to ease samples removal and slurry or water loss. The grease was also used to seal the mold base and lubricate mold screws.

The slurry is poured into molds or glass vials and air bubbles are removed by using a corrosion-resistant 6mm diameter puddling rod. The samples are puddled at approximately one-half of the mold depth with 27 circular motions, after which the

remaining slurry is stirred with a spatula and poured to the top. The samples are puddled again, and excess slurry is removed from the mold. No top plate is used in these experiments.

The molds are placed in water baths with deionized water at 25°C, 50°C, and 75°C (±3°C). Water temperatures were closely monitored and the highest deviation is experienced when fresh water is added to compensate water evaporation. To reduce this effect, smaller volumes of water were added to the water baths on a regular basis.

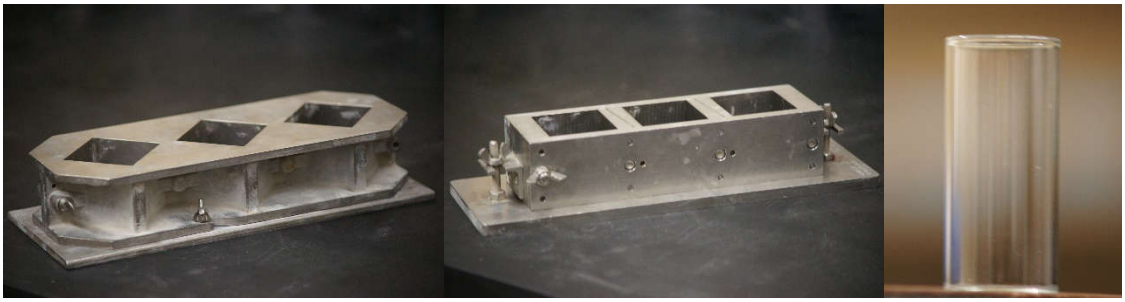

Figure B2 – Two-inch cube molds (left, center), glass vial (right) (not on scale)

The samples cast in API certified metal molds were removed after 1 day and kept under water at constant temperature and surface pressure. The cylindrical samples were kept in vials and the sample tops were constantly in contact with water. Cores from cubes were used for indirect tensile strength measurements.

Figure B3 – Water bath used for curing cement samples

B.3. Sample Geometry

API RP 10B-2 recommends the testing of cubes with a 2-inch edge (or 50.8 mm). For the cubes used in this work, their dimensions were measured by using a digital Vernier caliper. 90% of the cube samples were always within 10% of the API recommendations, with the rest of the samples being smaller than the suggested size because of cement losses when mixing and casting, or subsequent slurry loss. These samples were tested and documented separately. These cube geometrical measurements are necessary for the calculation of compressive strength and ultrasonic waves' travel speed.

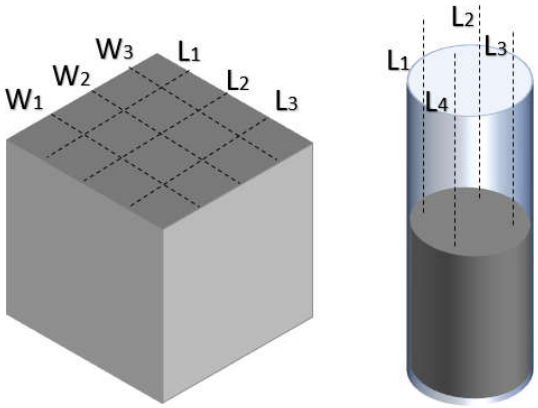

Figure B4 – Dimensions Measurement for Cube and Cylinder

For the samples poured in glass cylinders, the inner diameter and initial length of these have been measured. After curing, the length from the top of the glass vial to the top of cement is measured with a caliper and subtracted from the total inner length of the glass cylinder. This gives a good estimate of the bulk volume for the NMR measurements.

After coring and slicing, the diameter and length of the samples prepared for indirect tensile strength measurements were measured with a digital caliper as well.

Appendix C: Ultrasonic Principles

Assuming the material is homogeneous, two types of waves can be transmitted: a compressional (longitudinal, principal, acoustic, or sonic) wave, and a transversal, or shear wave. The longitudinal wave travels at higher velocities than the shear wave. If a material is isotropic and linearly elastic, the following relationships can be used to relate velocities and moduli:

$$V_p = \sqrt{\frac{K + \frac{4}{3}G}{\rho}} \tag{C1}$$

$$V_s = \sqrt{\frac{G}{\rho}} \tag{C2}$$

where V_p is the principal velocity, V_s the shear velocity, K is the bulk modulus, G is the shear modulus, and ρ is the bulk density. During an ultrasonic experiment, a transmitter sends a wave caused by the expansion of an electrically stimulated piezoelectric crystal. The receiving piezoelectric crystal captures the sent wave, which is recorded by an oscilloscope. The travel velocity is:

$$V_i = \frac{d}{tt}, i \in \{p, s\} \tag{C3}$$

d – travel distance (m), tt – transient time (s)

After acquiring the transient times and calculating the velocities, the bulk and shear moduli can be rewritten as:

$$G = \rho {V_s}^2 \tag{C4}$$

$$K = \rho\left({V_P}^2 - \frac{4}{3}{V_s}^2\right) \tag{C5}$$

The calculation of Young's modulus (E) and Poisson's ratio (ν) follows (see Birch 1957).

$$E = \frac{9GK}{G + 3K} = \frac{9\rho {V_s}^2 \left(\frac{K}{\rho {V_s}^2}\right)^2}{3\left(\frac{K}{\rho {V_s}^2}\right)^2 + 1} \quad \text{(C6)}$$

$$\nu = \frac{\left(\frac{V_p}{V_s}\right)^2 - 2}{2\left(\frac{V_p}{V_s}\right)^2 - 1} \quad \text{(C7)}$$

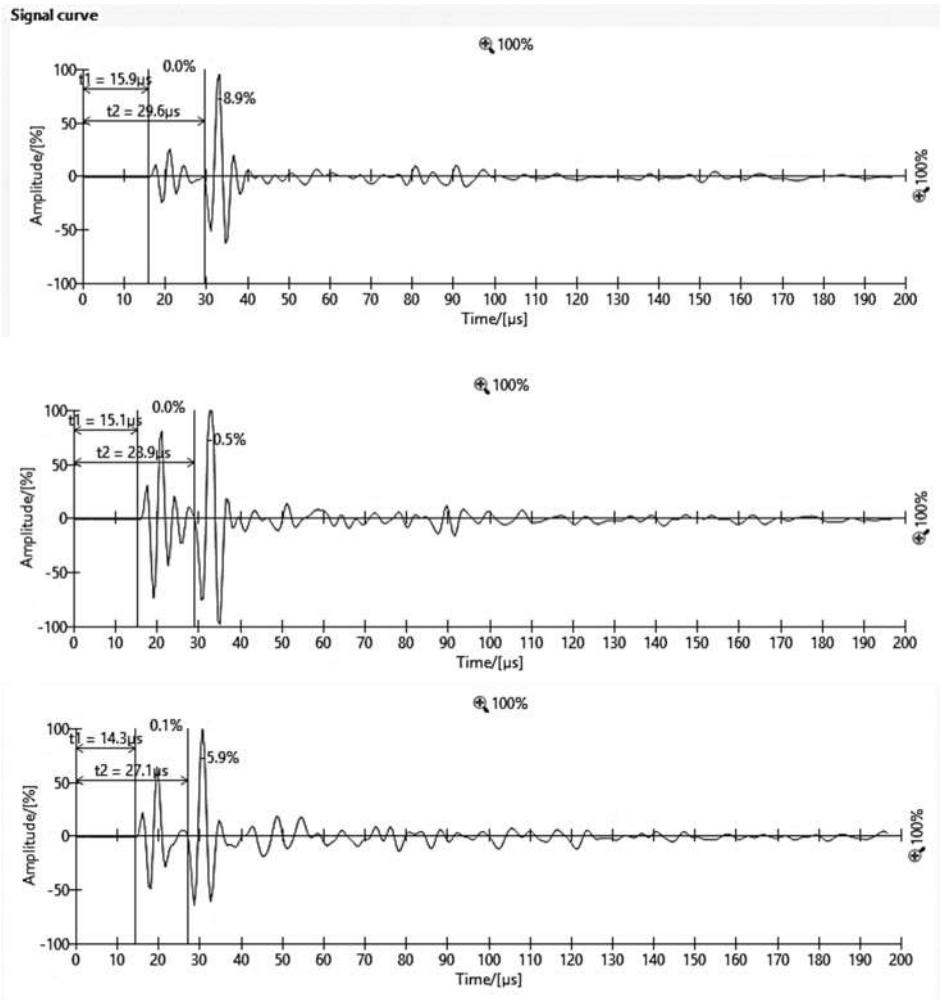

Figure C1 – Vp and Vs Arrival Times Pick in Neat Cement at Two Different Ages (Top and Center) and in Salt Cement (Bottom)

Appendix D: Error Sensitivity Analysis for UCS-UPV Correlations

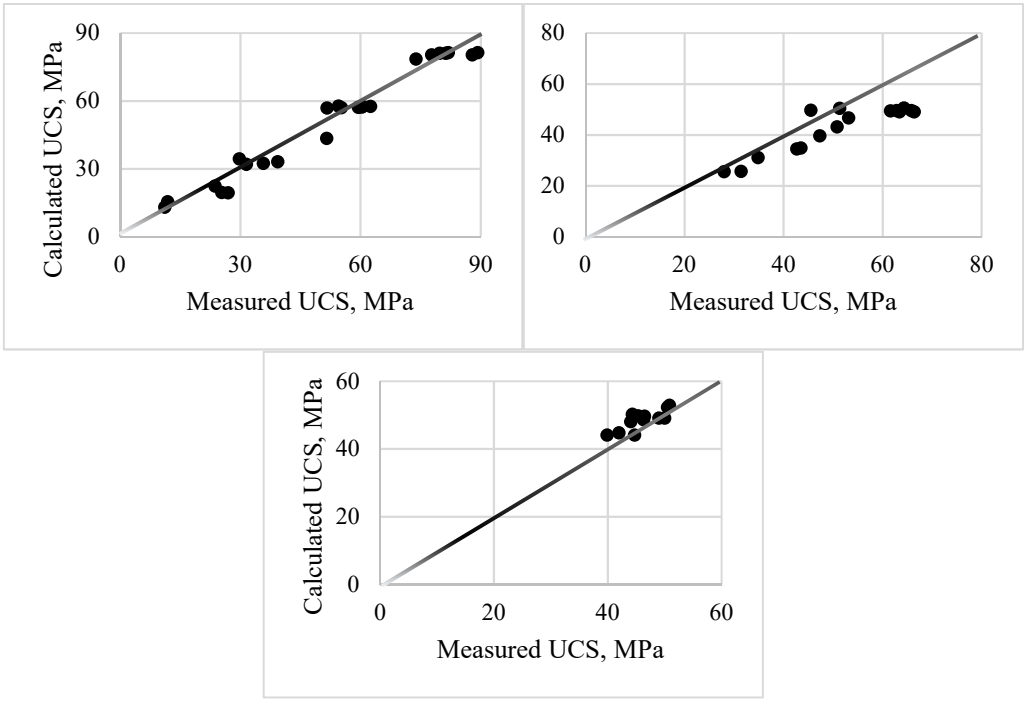

Figure D1 – Error Sensitivity Plots for Neat Cement Cured at 25°C (left), 50°C (right), 75°C (center)

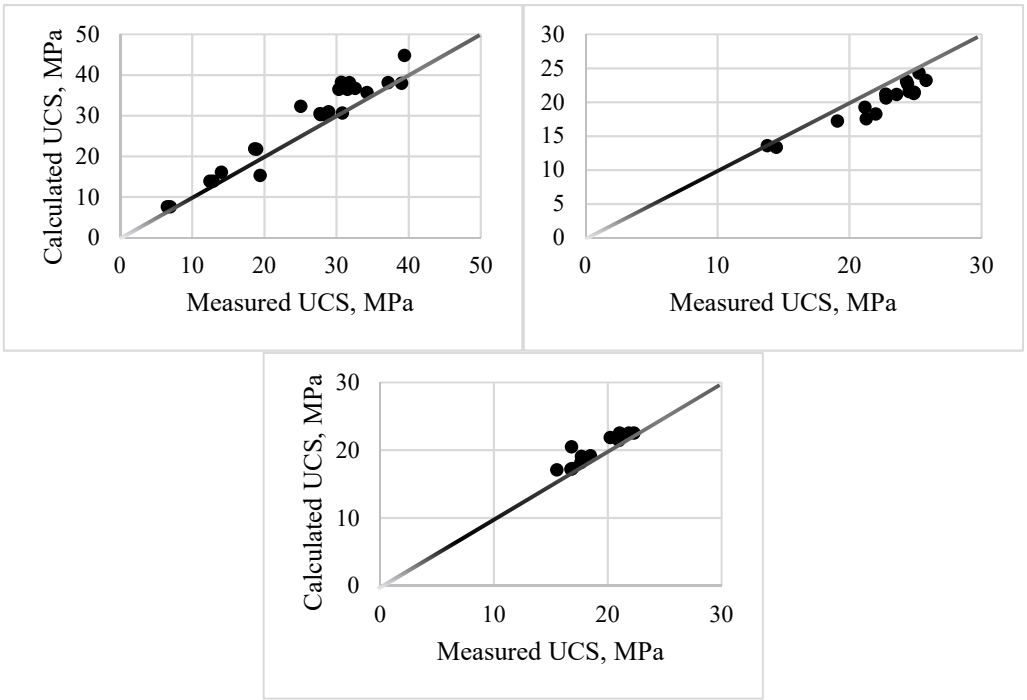

Figure D2 – Error Sensitivity Plots for 4% Bentonite Cement Cured at 25°C (left), 50°C (right), 75°C (center)

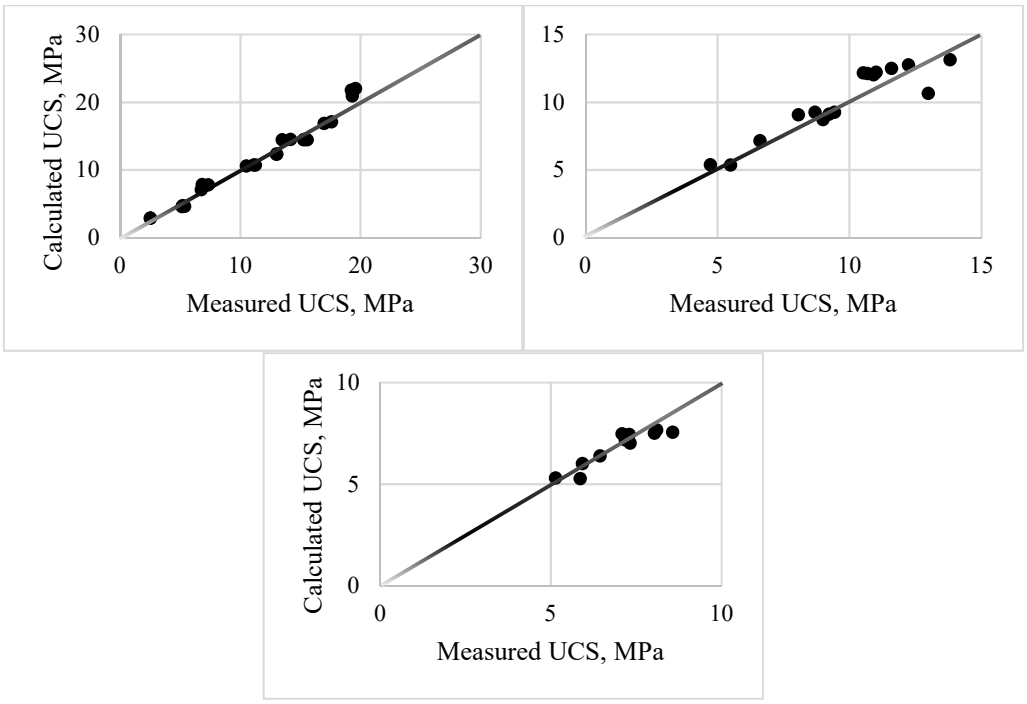

Figure D3 – Error Sensitivity Plots for 10% Bentonite Cement Cured at 25°C (left), 50°C (right), 75°C (center)

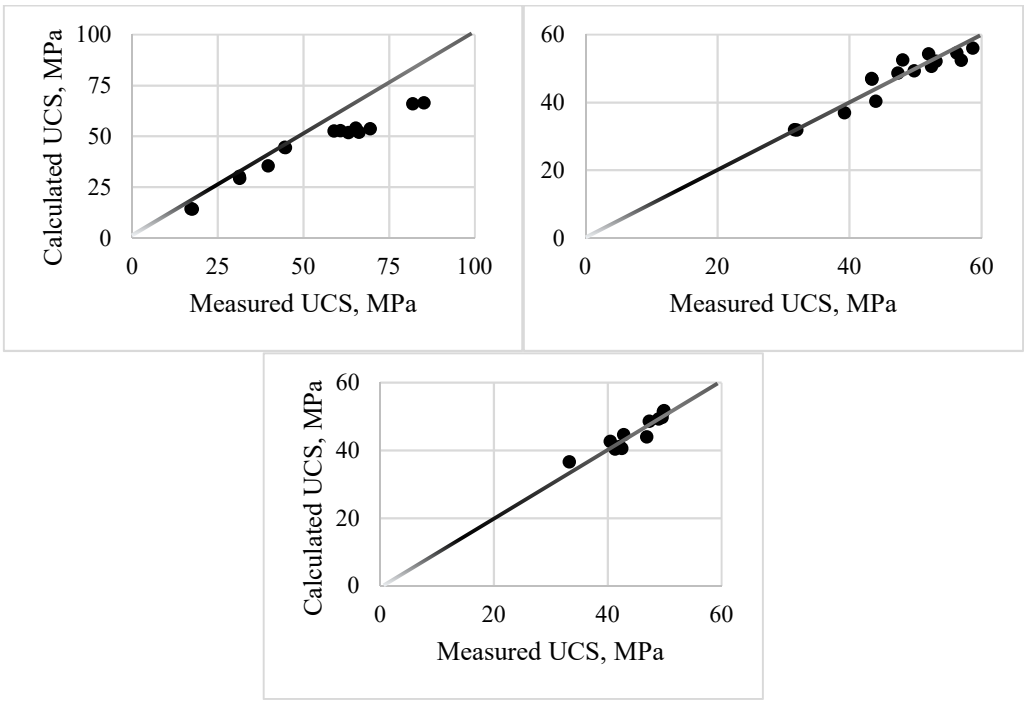

Figure D4 – Error Sensitivity Plots for 4% Salt Cement Cured at 25°C (left), 50°C (right), 75°C (center)

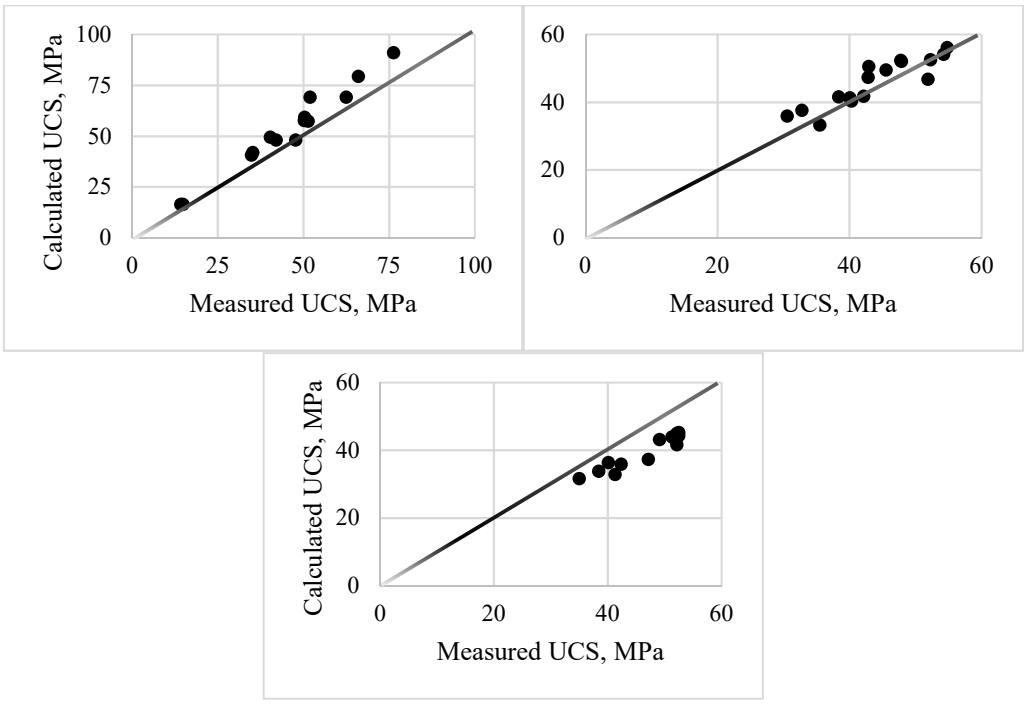

Figure D5 – Error Sensitivity Plots for 12% Salt Cement Cured at 25°C (left), 50°C (right), 75°C (center)

Appendix E: NMR Principles

In petroleum engineering, NMR principles like nuclear magnetism, polarization, T1 and/or T2 relaxation time, pulse tipping, free induction decay, spin echoes and CPMG sequences are utilized to analyze fluids trapped in the pore spaces of the rocks and to provide a mineralogy-independent porosity and its distribution (Coates et al. 1999), but also for irreducible water saturation determination, hydrocarbon typing, oil viscosity and rock permeability estimation after proper calibration (Dunn et al. 2002). .

Many atomic nuclei are constantly spinning around their axis and have a spin angular momentum and an intrinsic magnetic moment associated with it in their ground state, both being along the same direction, and producing *nuclear magnetism*. The hydrogen proton, of interest in ^{1}H proton NMR, has a spin of 1/2, leading to nuclear magnetic resonance (Dunn, Bergman and Latorracca 2002). The abundance of hydrogen in formations bearing water and/or hydrocarbons explains the popularity of ^{1}H NMR tools in laboratory and field tools.

Polarization represents the first step of an NMR measurement and consists of aligning magnetic nuclei with an external, static magnetic field, which, when applied, exerts a torque on the nucleus that acts to align the nuclear spin axis with the applied field. Parallel alignment of the proton to the static field is the low energy state, whereas anti-parallel alignment is a high energy state. More spinning protons prefer the low energy state, reason why the net magnetic moment of all protons is parallel to the external magnetic field (Minja and Lieberman 2017). Because of the torque exerted by the external magnetic field, the axis of the nucleus moves perpendicular to the torque in a motion called precession, at a frequency termed Larmor frequency, calculated by multiplying the

strength of the static magnetic field with the gyromagnetic ratio ($\gamma/2\pi$=42.58 MHz/T for hydrogen nuclei). Because the Larmor frequency depends on the magnitude of the static magnetic field and the given nuclear species, the location of the region investigated is determined by the operational frequency (Coates et al. 1999). Once the protons are in equilibrium with the external magnetic field, B_0, a radiofrequency (RF) pulse is applied, disrupting the equilibrium and causing the protons to fall out of alignment with the external magnetic field. After the RF pulse, the nuclei will return to their aligned state and continue precession around B_0. The polarization process depends on time and is described by:

$$M_z(t) = M_o(1 - e^{\frac{-t}{T_1}}) \quad \text{(E1)}$$

where t represents the time of protons' exposure to the magnetic field (B_0), $M_z(t)$ is the magnitude of magnetization at time t, M_0 is the final and maximum magnetization in a given magnetic field, and T_1 is the longitudinal relaxation time, also described as spin-lattice relaxation time. T_1 is a joint property of the spin system and its environment, its value reflecting how effectively the magnetic energy of the spin system is transferred to or from its surroundings (a large value translates into a weak coupling, whereas a small value shows a good coupling and a rapid approach to equilibrium) (Dunn et al. 2002).

The second step in the measurement cycle is *pulse tipping,* which changes the magnetization from the longitudinal direction to a transverse plane (from the z-direction to the xy-direction). The application of an oscillating magnetic field (B_1) perpendicular to the static magnetic field (B_0) leads to tipping, a jump of protons from low to high energy levels, causing them to precess in phase with one another, both leading to nuclear magnetic resonance (Coates et al. 1999).

When the transversal field is turned off, the protons dephase and net magnetization decreases. A receiver coil measures the decaying signal, called *Free Induction Decay, FID*. This is usually exponential, and has a very short time constant (T_2^*) because of the inhomogeneities in the B_0 field, which leads to protons at different locations precessing with different Larmor frequencies.

The dephasing of protons caused by B_1 is reversible through the application of a 180° pulse (B_1), leading to *Spin-Echo Detection.* The time constant of transverse magnetization decay is the transverse relaxation (T_2), and the magnitude of the spin-echo train is given by the following exponential:

$$M_x(t) = M_{0x}(e^{\frac{-t}{T_2}}) \tag{E2}$$

In these measurements, the strength of the measured field depends upon the number of protons remaining aligned in the transverse (B_1) plane, which becomes smaller with increasing measurement time (usually to the order of ms), because the 180° pulses cannot realign the protons which are out of plane or which have relaxed (due to Brownian motion and surface relaxation) (Sondergeld 2017). The chance of a proton encountering its containing surface increases as the enclosure becomes smaller, resulting in a shorter relaxation time for water in small pores, than for water in large pores. When surface relaxivity dominates, T_2 is directly proportional to the size of the pores, and is defined as

$$\frac{1}{T_2} = \rho_r \frac{S}{V} = \frac{\rho_r}{a} \tag{E3}$$

Where ρ_r is the surface relaxivity ($\mu m/s$), S is the surface area (m^2), V is the pore volume (m^3), and a is the pore dimension (usually radius - m). A similar relationship is observed for spin-lattice relaxation (T_1).

T_1 and T_2 measurements encode frequency at a fixed gradient value and variable time. Another type of NMR measurement is phase encoding, which changes gradient values with a fixed encoding time, and it is a robust approach for imaging samples with short relaxation times (Muir and Balcom 2012). Single Point Ramped Imaging with T_1 Enhancement (or SPRITE), developed by Balcom et al. (1996), employs a short RF pulse and a ramped gradient to produce images of short T_2* samples, and is an alternative to the SPI (single point imaging) method, which uses intense, rapidly switched gradients. The double half k-space (DHK) SPRITE experiment is employed for one-dimensional imaging (where k-space stands for the matrix of numbers representing spatial frequencies in the NMR image before Fourier Transformation). DHK SPRITE samples data in one half of k-space by incrementing the gradient, then, after a relaxation delay of $5 \times T_1$, the data in the second half of k-space are sampled by incrementing the gradient in the opposite direction. The acquired data sets are arranged in a single linear array, and the two k = 0 points are averaged prior to a Fourier transform (Muir and Balcom 2012).

Appendix F: NMR System Calibration

Before running a series of measurements, the system is calibrated with a pre-configured calibration sample (water with 2% NaCl in a sealed glass vial), with a diameter of 32 mm, length of 46 mm, 17.01 ml of NMR fluid volume, and the following properties: $T_{2max}^{*} =$ 10 ms, $T_{2max} = T_{1max} = 100$ ms and 46% NMR porosity. A special tool is used to center the sample inside the magnetic field of the NMR system (**Figure F1**).

Figure F1 – Centered Calibration Sample

Calibration is necessary to ensure that all tests are correctly displaying the results in units of volume or porosity. The calibration test determines the NMR resonance frequency, the resonance frequency pulse lengths for 90° and 180° tip angle pulses, and the calibration factor for all the acquisition tests (performed to convert NMR machine units to fluid volume by using the known calibration sample volume). Moreover, a system health measurement is performed during calibration, which measures the NMR resonant frequency, the magnetic field homogeneity, the signal to noise ratio (SNR), the system sensitivity, and the RF probe frequency response (reflected RF power versus frequency) (Green Imaging Technologies, Inc. 2016).

Moreover, the accuracy of the NMR system has been determined by performing 13 separate measurements on water volumes ranging from 1 to 20 ml. The results, plotted in the following figure, show a very high linearity.

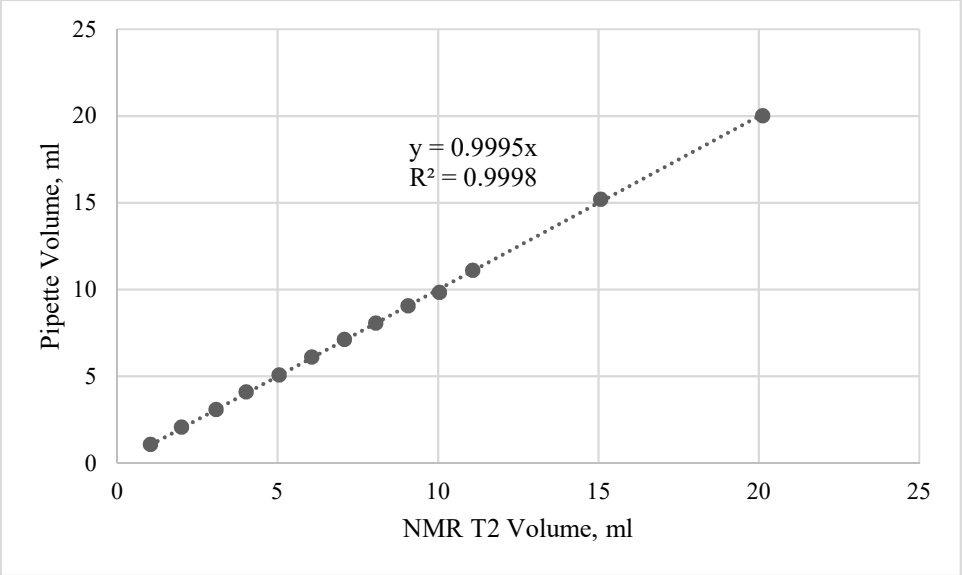

Figure F2 – Results Consistency between Pipette Volume and NMR Measured Volume